NEW RADIO FREQUENCY SENSOR NETWORK MEASUREMENT MODELS AND METHODS FOR TRACKING APPLICATIONS

by

Peter Thomas Hillyard

A dissertation submitted to the faculty of
The University of Utah
in partial fulfillment of the requirements for the degree of

Doctor of Philosophy

Department of Electrical and Computer Engineering

The University of Utah

August 2017

The University of Utah Graduate School

STATEMENT OF DISSERTATION APPROVAL

The dissertation of **Peter Thomas Hillyard**
has been approved by the following supervisory committee members:

Neal Patwari ,	Chair(s)	**April 17, 2017** Date Approved
Rong Rong Chen ,	Member	**April 17, 2017** Date Approved
Behrouz Farhang ,	Member	**April 17, 2017** Date Approved
Sneha Kasera ,	Member	**April 17, 2017** Date Approved
Suresh Venkatasubramanian ,	Member	**April 17, 2017** Date Approved

by **Gianluca Lazzi** , Chair/Dean of
the Department/College/School of **Electrical and Computer Engineering**
and by **David B. Kieda** , Dean of The Graduate School.

ABSTRACT

Device-free localization (DFL) and tracking services are important components in security, emergency response, home and building automation, and assisted living applications where an action is taken based on a person's location. In this dissertation, we develop new methods and models to enable and improve DFL in a variety of radio frequency sensor network configurations.

In the first contribution of this work, we develop a linear regression and line stabbing method which use a history of line crossing measurements to estimate the track of a person walking through a wireless network. Our methods provide an alternative approach to DFL in wireless networks where the number of nodes that can communicate with each other in a wireless network is limited and traditional DFL methods are ill-suited.

We then present new methods that enable through-wall DFL when nodes in the network are in motion. We demonstrate that we can detect when a person crosses between ultra-wideband radios in motion based on changes in the energy contained in the first few nanoseconds of a measured channel impulse response. Through experimental testing, we show how our methods can localize a person through walls with transceivers in motion.

Next, we develop new algorithms to localize boundary crossings when a person crosses between multiple nodes simultaneously. We experimentally evaluate our algorithms with received signal strength (RSS) measurements collected from a row of radio frequency (RF) nodes placed along a boundary and show that our algorithms achieve orders of magnitude better localization classification than baseline DFL methods.

We then present a way to improve the models used in through-wall radio tomographic imaging with E-shaped patch antennas we develop and fabricate which remain tuned even when placed against a dielectric. Through experimentation, we demonstrate the E-shaped patch antennas lower localization error by 44% compared with omnidirectional and microstrip patch antennas.

In our final contribution, we develop a new mixture model that relates a link's RSS as a

function of a person's location in a wireless network. We develop new localization methods that compute the probabilities of a person occupying a location based on our mixture model. Our methods continuously recalibrate the model to achieve a low localization error even in changing environments.

For the glory and honor of the Sensing and Processing Across Networks (SPAN) Lab

CONTENTS

LIST OF FIGURES

LIST OF TABLES

ACKNOWLEDGEMENTS

When you accomplish a great feat in life, it is necessary to acknowledge mentors, colleagues, friends, and family who provided guidance, encouragement, and tools which contributed to your achievement. I would like to thank my advisor, Neal Patwari, for offering me a position in the glorious Sensing and Processing Across Networks (SPAN) Lab, an opportunity that has inestimable worth to me. I have been a benefactor of Neal's wealth of knowledge, experience, and vision and his abundance of patience. I would also like to thank the exceptional teachers and my committee members at the University of Utah from whom I learned a great deal.

I owe a great deal of gratitude to colleagues with whom I consulted and collaborated. I would like to thank Maurizio Bocca at Bosch RTC; Joey Wilson and Dustin Maas at Xandem Technology who provided the wireless nodes used in the experiments presented in Chapter 6; Greg Durgin and Cheng Qi at Georgia Tech; and Anh Luong, Michael Empey, Phil Lundrigan, Samira Daruki, Alemayehu Solomon, Amal Al-Husseiny, and Charissa Che at the University of Utah. I would finally like to thank my wife, Anna, who, without needing bribery, helped me perform many experiments for this dissertation, and my parents who loaned a parcel of their backyard for a year so that I could localize boundary crossings.

CHAPTER 1

INTRODUCTION

Wireless transmission and communication have changed our world in so many ways. Embedded devices the size of a thumb can send and receive data wirelessly at astonishing speeds to another device many meters away. With multiple nodes forming a network, data can be passed from one node to another until it reaches its destination. These networks are appearing in greater numbers in our homes, businesses, and communities. When a node in a network transmits its data, an electromagnetic wave propagates throughout space. The electromagnetic waves are inevitably reflected, attenuated, and scattered by the objects and people in that space. As the objects and people in the space move, a receiving node will measure changes in the wireless channel. The same channel over which data are sent is also the medium through which two nodes sense a person nearby. With a network of these nodes, we are able to locate the source of the movement. Using the measurements on the links on a wireless network to perform localization has been called sensorless sensing [15], passive localization [12], and device-free localization (DFL) [17], since we do not localize tags.

In this dissertation, we develop new methods and models to enable and improve DFL in a variety of sensor network configurations. The configuration of the sensor network can vary in many ways. The nodes of a sensor network can be statically deployed or the nodes can be moving. Alternatively, the number of nodes that can communicate with each other may be few because of the choice of communication protocol or because of a low signal-to-noise ratio. Sensor networks can also differ in the node's configuration geometry. Even the choice of hardware can influence the models and methods used in DFL. Understanding the nature of the problems we address in this dissertation requires that we first define the important terms *link*, *sensor*, *localization*, and *link line*.

The wireless networks we refer to in this dissertation are made up one or many nodes

that can make measurements of the wireless channel. A pair of nodes creates a *link* between many or all other nodes in the network. In that the measurements of the channel are changed by the presence and movement of a person, a wireless link forms a *sensor* by which we sense the presence and location of a person. A wireless sensor network is thus made of many links that provide the measurements to sense the environment.

The goal in DFL is to use the measurements of all the links to perform *localization* where we estimate the coordinates of a person in space. In this dissertation, we limit localization to one person in either one-dimensional (1D) or two-dimensional (2D) space. Many of the localization methods we develop are based on the idea of crossing lines. We call the imaginary line segment between two nodes a *link line* which is crossed when a person passes between the nodes. A link line crossing detector then indicates when the person is occupying the space between the nodes. A person's location can be inferred when they cross many link lines simultaneously, or over time.

In the remainder of this chapter, we discuss the applications that require or benefit from DFL in Section 1.1 and then we explain several methods of performing DFL in Section 1.2 and the channel measurements that can be used for sensing in Section 1.3. In Section 1.4, we explain the contributions of this dissertation to work in DFL and outline the remainder of the dissertation in 1.5.

1.1 DFL Applications

DFL systems have a long history in military applications to detect aircraft and missiles in the air and sea vessels that are unseen in darkness or in fog. Weather prediction has also benefited from tracking the path of clouds with radar. DFL technology, which has filled the skies and seas, is gradually making a greater presence in homes, buildings, and cities. Home and business owners benefit from DFL because it serves as a security system. Detecting intruders and having a record of their path provides valuable information on how much time was spent in the vicinity, when the intrusion occurred, and the rooms or offices the intruder visited. A DFL system could also supply information to a smart home or building that sends actuation commands to appliances, lights, locks, and window covers based on the location of a person inside. As the life expectancy increases, more of the aging population is opting for aging in place and in-home care during their sunset years.

Family members and caretakers of the aging population can use DFL to remotely monitor daily activity. A system could notify caretakers if the aging person has not moved from one location for a period of time which may indicate that they have fallen, for example. With technological advances happening at an increasing rate, the number of location-based services will continue to rise. Creating DFL systems that can provide reliable and efficient solutions will need to keep up with this demand.

1.2 DFL Methodologies

Many forms of DFL have been developed to localize and track a person based solely on observed or modified channel measurements the person's presence and movement induces. We describe the more traditional DFL methods in the following sections.

1.2.1 Fingerprint Methods

In multipath environments, it is difficult to predict what the observed channel measurements will be as a function of a person's location. The size, clothing and spatial orientation of a person as well as the RF properties and locations of objects in the environment are additional variables that make this prediction even more challenging. An alternative to predicting is measuring and is accomplished by performing fingerprint training in many locations in the area of interest. Channel measurements are stored to a database and labelled with the location of the person. After the training period is over, DFL is performed by computing a similarity metric between new channel measurements and those stored in the database. The label with the greatest similarity is then selected as the location estimate [11], [16]. Fingerprint DFL is highly accurate when the only change in the environment is a person moving inside. But by moving, adding, or removing objects from the area, fingerprints need to be retrained to account for the changed environment [10].

1.2.2 Model-Based

Training and retraining fingerprints can be laborious and infeasible which is why many DFL methods are model-based. Model-based DFL instead uses spatial models to define the relationship between changes in channel measurements and a person's location *a priori*. Typically these models are based on the idea that changes in a link's channel measurements are caused by a person being on or near the link line. It is necessary, therefore, to have

reference channel measurements when the person is not affecting the link's measurements. Reference measurements are typically obtained when it is known the area of interest is vacant or by keeping a long-term average of the channel measurements. Yet, there are discrepancies between the spatial model and with reality which can result in poorer localization performance than fingerprinting. In spite of this trade-off, many types of DFL have been developed for their ease of use. Some of the more popular methods are described in the next sections.

1.2.2.1 Bistatic Radar

Radars have been widely used in the military and in the aviation industry to track the location of objects flying in the sky. In monostatic pulse radar systems, a transmitter sends a pulse in the direction of possible targets. When a target is nearby, it reflects some of the electromagnetic energy toward the source which is in receive mode. The receiver then estimates the time between the reflection and reception and uses this estimate to calculate the distance to the target. An actual location estimate can be achieved with bistatic pulse radar [1]. A transmitter sends a pulse and a receiver measures many copies of this pulse as it was reflected off of objects in the environment. One of the copies of the pulse can be caused by the presence of a person. The time difference between the first arriving copy, or path, and the path caused by the person translates to the excess length of the reflected path. For a transmitter-receiver pair, the excess path length puts the person on an ellipse whose foci are the locations of the transmitter and receiver. When multiple receivers estimate the excess path length, multiple ellipses are formed, the intersection of which estimates the location of the person.

1.2.2.2 Radio Tomographic Imaging

In radio tomographic imaging (RTI), an image of showing the locations which are most likely responsible for the change in channel measurements is estimated [9], [13]. RTI uses a linear model that relates the change in channel measurements $\mathbf{y}$ and an image $\mathbf{x}$ through

$$\mathbf{y} = \mathbf{W}\mathbf{x} + \mathbf{n} \tag{1.1}$$

where $\mathbf{n}$ is noise and $\mathbf{W}$ is a weight matrix that defines how much a person's presence in a pixel contributes to changes in a link's channel measurements. A common weight matrix

follows an elliptical model where a change in channel measurements on a link only occur when a person occupies a pixel inside of an ellipse whose foci are the link's nodes. A regularized least-squares solution to this linear equation is typically used to estimate the image **x**. Each pixel in **x** maps to a coordinate in space, and the coordinate whose pixel is greatest is the location of the person.

1.2.2.3 Particle Filters

A different approach to localization is to say that the channel measurements are a random variable and that they follow a probability distribution conditioned on the location of the person [14], [18]. Likelihoods of observing new channel measurements given particle locations are computed using the distributions. The particle with the greatest likelihood is selected as the location estimate. It is common to define a link as being in either an affected or unaffected state. The link follows either an unaffected or affected distribution. The parameters for these distributions are either learned on-the-fly or through training. Like in RTI, particle filters use an elliptical model to spatially define where a person must be for the link to be in either the affected or unaffected state.

1.3 RF Devices Used in DFL

RF devices offer a variety of different ways to make measurements of the channel between two nodes. These measurements are then processed to perform DFL, as discussed previously. RF devices differ in many ways, but we focus on ultra-wideband and narrowband transceivers and discuss what channel measurements they offer for use in DFL.

1.3.1 Ultra-Wideband

In an ideal wireless transmission, we would be able to send pulses with infinitely narrow periods. When the pulse is sent, copies of it travel along many paths, being reflected and attenuated by objects nearby in the process. A receiver then measures the pulse that traveled along the LOS path as well as the paths of longer lengths. The channel at time t is modeled as the linear function

$$h(t,\tau) = \sum_{j=1}^{N} \alpha_j(t)\delta(\tau - \tau_j(t)) \tag{1.2}$$

where τ is a time delay, N is the number of paths, α_j is the complex gain of the jth path, and $\delta(t)$ is the Dirac impulse function [2]. Radios cannot send infinitely narrow pulses, but with (UWB) radios, the period of the pulse is very small. An UWB receiver can measure the channel impulse response (CIR) which exposes the constructive and destructive interference of the pulses at many time delay bins. Changes in the complex amplitude in individual time delay bins can indicate the presence or absence of a person, as was explained in bistatic radar DFL. When the changes in amplitude occur for paths with very short time delays, that provides evidence that a person is on or near the link line where the paths have very small excess path lengths. We leverage this portion of UWB CIR measurements along with RTI to perform DFL in Chapter 3.

UWB radios come with a cost. A typical UWB radio will cost on the order of hundreds or thousands of dollars. Additionally, it occupies a 500 MHz or greater portion of the radio spectrum. With bandwidth already at a premium, the widespread use of UWB for DFL applications may not be a viable solution.

1.3.2 Narrowband

Measuring the channel impulse response is only possible with radios that are allowed to occupy a large part of the radio spectrum. In contrast, narrowband receivers are limited to measuring either amplitude and phase or received signal strength (RSS). While amplitude and phase are accessible on some wireless devices, RSS measurements are more ubiquitous and are easily accessible. The RSS is an estimate of the power at the receiver's antenna and is a measure of the sum of the magnitudes of all multipath components in the CIR. Unlike the measured CIR, RSS contains contributions from all time delays. This means that RSS measurements can change significantly even when a person stands far from the link line. Additionally, a person could stand directly on the link line without causing a significant change in RSS. So although RSS is easily accessible and ubiquitous, the measurement itself makes it difficult to predict the affect a person's location will have on RSS measurements. In this dissertation, we develop new RSS-based methods and spatial models to enable and improve DFL.

1.4 Contributions

In this dissertation, we make several contributions to the field of DFL using the channel measurements of wireless sensor networks. These contributions include new models to capture the relationship between RSS measurements and a person's location and developing new methods to perform DFL with line crossing measurements. The publications, both accepted and in process, along with the specific contributions of the author are summarized below.

- **P. Hillyard**, S. Daruki, N. Patwari, and S. Venkatasubramanian, "Track estimation using link line crossing information in wireless networks," Global Conf. on Signal and Inform. Process. (GlobalSIP), 2013 IEEE, 2013 [3].

    1. In wireless networks with many, well-distributed, fully-connected nodes, DFL methods can achieve low localization error because a person is likely to affect the RSS measurements on multiple links simultaneously. However, DFL methods can be ill-suited to perform localization when the wireless network has a low-density of link lines passing in the area. In this work, we advance the field of DFL by developing two new methods to perform tracking in networks where traditional DFL methods are ill-suited. Our methods estimate the track a person took while in the network from a history of link line crossing measurements.

    2. My contribution in this work includes the development of the linear regression and line stabbing algorithms to perform track estimation. Additionally, I developed a simulation testbed where the tracking performance of the linear regression and line stabbing solutions could be evaluated and compared. We include this work in Chapter 2.

- **P. Hillyard**, D. Maas, S. Premnath, N. Patwari, and S. Kasera, "Through-wall person localization using transceivers in motion," Arxiv.org, Tech. Rep. arXiv:1511.06703 [cs.ET], Nov. 2015 [5].

    1. Many DFL methods are developed under the assumption that the nodes of the sensor network are statically deployed. Changes in the RF measurements are consequently the cause of people moving inside the network. We contribute the

to the field of DFL by putting the nodes in motion where they quickly sweep the area for changes in channel measurements which would indicate the presence and location of a person. However, changes in the channel measurements are a combination of a person's presence and small scale fading due to moving nodes. An additional contribution to DFL we make is showing that we can discriminate between small scale fading and a person's presence using the energy contained in the first few nanoseconds of a link's channel impulse response measurement. In addition, our choice of channel measurement fits naturally with RTI's spatial model because multipath with short time delays are changed or created when a person is inside the ellipse of a link.

2. My contribution in this work includes making measurements with ultra-wideband impulse radios to demonstrate that we can detect link line presence from the energy contribution of short excess delays in the impulse response. Additionally, I led the experiments to collect impulse response measurements used for localization evaluation. Lastly, I developed the link line presence detection algorithms and the algorithm used to estimate a person's location. We include this work in Chapter 3.

- **P. Hillyard**, N. Patwari, S. Daruki, and S. Venkatasubramanian, "You're crossing the line: Localizing border crossings using wireless RF links," 2015 IEEE Signal Process. and Signal Process. Educ. Workshop (SP/SPE), Aug. 2015. [6].

- **P. Hillyard** and N. Patwari, "Demonstration: Detecting and localizing border crossings using RF links," Proc. of the 14th Int. Conf. on Inform. Process. in Sensor Networks (IPSN '15), Apr. 2015 [8].

- **P. Hillyard**, A. Luong, and N. Patwari, "Highly reliable signal strength-based boundary crossing localization in outdoor time-varying environments," Proc. of the 14th Int. Conf. on Inform. Process. in Sensor Networks (IPSN '16), Apr. 2016 [4].

1. Algorithms that detect link line crossings suffer from false alarms and missed detections. Our contribution to DFL in these works includes a new deployment geometry to correct individual link line crossing measurement errors. We de-

ploy nodes linearly along a boundary which naturally partitions a boundary into short segments and places link lines in an overlapping geometry. An additional contribution is this work is that we develop localization methods that exploit the network geometry to provide robust boundary crossing localization by correcting errors in single link line crossing measurements.

2. In these works, I carried out over 75 h worth of experimentation, gathering RSS measurements during boundary crossings during in sunny, windy, and rainy periods. I developed four new boundary crossing localization systems that leveraged the linearly deployed node configuration. I also developed code to compare my methods against baseline DFL methods in terms of localization accuracy. Additionally, I built the physical system and created the algorithms for a real-time boundary crossing localization system that ran for 3 months. We include this work in Chapters 4 and 5.

- **P. Hillyard**, C. Qi, A. Al-Husseiny, G. D. Durgin, and N. Patwari, "Focusing through walls: An E-shaped patch antenna improves whole-home radio tomography," 2017 IEEE Int. Conf. on RFID, May 2017 [7].

  1. In RSS-based RTI, an elliptical model is used to define the pixels in which a person must stand to affect the RSS on a link. There is often a mismatch between reality and these models. The differences between the model and reality are even greater when antennas are placed against the surface of exterior walls. This work advances the field of RTI-based DFL by lessening the gap between reality and the model with an appropriate antenna design. The E-patch antennas stay tuned when placed against an exterior wall. The result is that more power is concentrated in the ellipse around a link line, which more closely matches RTI's spatial model. This contribution improves RTI's localization performance when compared to when microstrip patch and omnidirectional antennas are used in RTI.

  2. In this work, I lead experiments at three sites to collect RSS measurements with E-shaped patch antennas, microstrip patch antennas, and omnidirectional

antennas. I wrote the scripts used to perform two different RTI methods on the experimental data we collected. We include this work in Chapter 6.

- **P. Hillyard** and N. Patwari, "Never use labels: Signal strength-based bayesian localization in changing environments," IEEE Trans. on Mobile Computing, (to be submitted).

    1. DFL methods commonly use an elliptical model to spatially define where a person must be such that they affect the RSS measurements on a link. In reality, a person inside the ellipse can have no effect on the RSS measurements, and a person outside the ellipse can affect RSS measurements. Our contribution to DFL in this work is to develop a mixture model such that there is some probability of a link being affected and unaffected as a function of the person's excess path length to the link. Another significant contribution we make is to make a localization system that tracks a moving and stationary person without an empty room calibration and without fingerprint training.

    2. In this work, I develop two new Bayesian localization methods that compute the probabilities of a person's location using the mixture model I develop. These two methods are evaluated from measurements I recorded at two different sites. Lastly, I implemented other DFL methods to serve as baseline comparisons. We include this work in Chapter 7.

1.5 Outline of Dissertation

In the remainder of this dissertation, we develop new methods of using link line crossings to perform DFL. Additional models are also developed for DFL applications. In Chapter 2, we estimate a person's track from a history of link line crossing measurements using two new track estimation methods we develop. In Chapter 3, we measure line crossings using transceivers in motion to localize a person through walls. Link line crossings are measured using the channel impulse response measurements from a pair of ultra-wideband radios. A boundary crossing localization system is developed in Chapters 4 and 5 using RSS measurements on overlapping links. We compare our methods with other DFL methods adapted to the boundary crossing problem. In Chapter 6, we fabricate

new E-shaped antennas that remain tuned when placed against a dielectric material, thus improving RTI's localization performance compared to other antennas. In Chapter 7, we create a new probabilistic mixture model that relates RSS measurements as a function of a person's location. The system is calibrated as a person moves inside the network. Lastly, in Chapter 8, we conclude with key findings from this work and future directions.

1.6 References

[1] C. Chang and A. Sahai, "Object tracking in a 2D UWB sensor network," in *Conf. Rec. of the 38th Asilomar Conf. on Signals, Syst and Comput., 2004.*, vol. 1, Nov 2004, pp. 1252–1256.

[2] H. Hashemi, "The indoor radio propagation channel," *Proc. of the IEEE*, vol. 81, no. 7, pp. 943–968, Jul 1993.

[3] P. Hillyard, S. Daruki, N. Patwari, and S. Venkatasubramanian, "Track estimation using link line crossing information in wireless networks," in *2013 IEEE Global Conf. on Signal and Inform. Process.*, Dec 2013, pp. 1037–1040.

[4] P. Hillyard, A. Luong, and N. Patwari, "Highly reliable signal strength-based boundary crossing localization in outdoor time-varying environments," in *2016 15th ACM/IEEE Int. Conf. on Inform. Process. in Sensor Networks (IPSN)*, April 2016, pp. 1–12.

[5] P. Hillyard, D. Maas, S. N. Premnath, N. Patwari, and S. K. Kasera, "Through-wall person localization using transceivers in motion," Arxiv.org, Tech. Rep. arXiv:1511.06703 [cs.ET], Nov. 2015.

[6] P. Hillyard, N. Patwari, S. Daruki, and S. Venkatasubramanian, "You're crossing the line: Localizing border crossings using wireless RF links," in *2015 IEEE Signal Process. and Signal Process. Educ. Workshop (SP/SPE)*, Aug 2015, pp. 249–254.

[7] P. Hillyard, C. Qi, A. Al-Husseiny, G. D. Durgin, and N. Patwari, "Focusing through walls: An E-shaped patch antenna improves whole-home radio tomography," in *2017 IEEE Int. Conf. on RFID*, May 2017.

[8] P. Hillyard and N. Patwari, "Detecting and localizing border crossings using RF links," in *Proc. of the 14th Int. Conf. on Inform. Process. in Sensor Networks*, ser. IPSN '15. ACM, 2015, pp. 388–389.

[9] O. Kaltiokallio, M. Bocca, and N. Patwari, "Enhancing the accuracy of radio tomographic imaging using channel diversity," in *2012 IEEE 9th Int. Conf. on Mobile Ad-Hoc and Sensor Sys. (MASS 2012)*, Oct 2012, pp. 254–262.

[10] B. Mager, P. Lundrigan, and N. Patwari, "Fingerprint-based device-free localization performance in changing environments," *IEEE J. on Selected Areas in Commun.*, vol. 33, no. 11, pp. 2429–2438, Nov 2015.

[11] M. Seifeldin, A. Saeed, A. E. Kosba, A. El-Keyi, and M. Youssef, "Nuzzer: A large-scale device-free passive localization system for wireless environments," *IEEE Trans. on Mobile Computing*, vol. 12, no. 7, pp. 1321–1334, July 2013.

[12] F. Viani, P. Rocca, M. Benedetti, G. Oliveri, and A. Massa, "Electromagnetic passive localization and tracking of moving targets in a wsn-infrastructured environment," *Inverse Problems*, vol. 26, no. 7, pp. 1–15, 2010.

[13] J. Wilson and N. Patwari, "Radio tomographic imaging with wireless networks," *IEEE Trans. on Mobile Computing*, vol. 9, no. 5, pp. 621–632, May 2010.

[14] ——, "A fade-level skew-Laplace signal strength model for device-free localization with wireless networks," *IEEE Trans. on Mobile Computing*, vol. 11, no. 6, pp. 947–958, June 2012.

[15] K. Woyach, D. Puccinelli, and M. Haenggi, "Sensorless sensing in wireless networks: Implementation and measurements," in *2006 4th Int. Symp. on Modeling and Optimization in Mobile, Ad Hoc and Wireless Networks*, April 2006, pp. 1–8.

[16] C. Xu, B. Firner, Y. Zhang, R. Howard, J. Li, and X. Lin, "Improving RF-based device-free passive localization in cluttered indoor environments through probabilistic classification methods," in *2012 ACM/IEEE 11th Int. Conf. on Inform. Process. in Sensor Networks (IPSN)*, April 2012, pp. 209–220.

[17] M. Youssef, M. Mah, and A. Agrawala, "Challenges: Device-free passive localization for wireless environments," in *Proc. of the 13th Annu. ACM Int. Conf. on Mobile Computing and Networking*, ser. MobiCom '07. ACM, 2007, pp. 222–229.

[18] Y. Zheng and A. Men, "Through-wall tracking with radio tomography networks using foreground detection," in *2012 IEEE Wireless Commun. and Networking Conf. (WCNC)*, April 2012, pp. 3278–3283.

CHAPTER 2

TRACK ESTIMATION USING LINK LINE CROSSING INFORMATION IN WIRELESS NETWORKS

2.1 Abstract

Device-free or non-cooperative localization uses the changes in signal strength measured on links in a wireless network to estimate a person's position in the network area. Existing methods provide an instantaneous coordinate estimate via radio tomographic imaging or location fingerprinting. In this paper, we explore the problem of, after a person has exited the area of the network, how can we estimate their path through the area? We present two methods which use recent line crossings detected by the network's links to estimate the person's path through the area. We assume that the person took a linear path and estimate the path's parameters. One method formulates path estimation as a line stabbing problem, and another method is a linear regression formulation. Through simulation we show that the line stabbing approach is more robust to false detections, but in the absence of false detections, the linear regression method provides superior performance.

2.2 Introduction

Current research in device-free localization can provide instantaneous or real-time coordinate estimates of a person inside the deployment area of a wireless network. The person carries no wireless device to assist in the localization. Technologies such as radio tomographic imaging (RTI) can achieve remarkable localization accuracy [3], [6]. However,

the accuracy comes at the requirement of a high density of radio sensing nodes.

In this paper, we explore the estimation of the person's path or trajectory through the deployment area after the person has travelled through. We may want to know the direction and velocity of their path, and be willing to wait until the person has crossed through in order to make the estimate. In cases when the node (and thus link) density is low, a person may cross links only occasionally, and thus instantaneous point estimates may have significantly higher error than the after-the-fact path estimate.

We propose two path estimators which receive which link lines were detected as crossed and at what times, and output the estimates of the parameters of a linear path. We approximate the person's path as straight based on the observation that people tend to walk in piecewise straight paths. The first method formulates path estimation as a line stabbing problem, and the second method is a linear regression formulation.

Inaccuracies that arise as a result of detecting link line crossings are the major hurdles affecting the performance of our proposed methods. Link line crossing detection methods will ultimately miss crossing events and will report false crossings. The solutions we propose track a person's path in spite of these errors. We analyze the performance of the two methods through simulation.

The paper is organized as follows. We introduce our link line detection model, and the line stabbing and linear regression algorithms in Section 2.3. We then present a simulation framework and provide and discuss results in Section 2.4. We conclude in Section 2.5.

2.3 Methodology

In this paper, we consider a wireless network with N wireless devices, or *nodes*. The coordinate of the ith node is given as $\mathbf{z_i} = (x_i, y_i)$ in a Cartesian plane. In this work we consider only 2D localization. The link $k = (i, j)$ is a communication link between transmitter i and receiver j. We refer to the *link line segment* as s_k, whose endpoints are $\mathbf{z_i}$ and $\mathbf{z_j}$; and to the *link line* which contains both $\mathbf{z_i}$ and $\mathbf{z_j}$. Link line k is also given as the equation $a_k y = b_k x + c_k$. In this paper, we assume a single person is walking, with position $\mathbf{p}[n]$ at time index n. Time index n corresponds to time nT_s, where T_s is a sampling period.

We assume that link line crossing detection is performed using measurements of the radio channel. For example, the channel measurement might be the RSS. When a person

passes near a link line segment, he tends to affect the received signal strength (RSS) measured on the link, in a manner that is detectable [2], [5], [6]. We assume a detector as in [2], [5], [6] is applied to the channel measurements at each time index.

2.3.1 Link Line Crossing Detection Model

Link crossing detection methods are prone to both false alarms and missed detections [6], but our experimental experience tells us that the further a person is from a link line segment, the less likely that link will detect a crossing [4]. Currently, no statistical model for link line crossing detection performance has been reported in the literature. In this work, we use a simple model to describe the probability of a link's channel measurement being "perturbed" by a person's presence at a particular location, and that perturbation then causing the link to be detected as "crossed". We denote $P_k[n]$ as the probability that link $k = (i, j)$ is detected as *perturbed* at time index n,

$$P_k[n] = P_0 e^{-\frac{1}{\delta}\left(\|\mathbf{z}_i - \mathbf{p}[n]\| + \|\mathbf{z}_j - \mathbf{p}[n]\| - \|\mathbf{z}_i - \mathbf{z}_j\|\right)} \tag{2.1}$$

where P_0 is the probability a perturbation event is detected when a person is blocking the link line segment, and δ is the decay constant. A smaller δ value models links that experience changes in RSS solely when $\mathbf{p}[n]$ is very near the link, while larger δ values model links that experience significant changes in RSS even when $\mathbf{p}[n]$ is relatively far away.

Link line crossing algorithms consider a link line *crossed* only when detected as perturbed consecutively for longer than T_c seconds, or $n_c = \lfloor \frac{T_c}{T_s} \rfloor$ samples [5]. If the case arises that a link detects more than one perturbation, the system detects a crossing and records the median of the perturbation events as the crossing time. After the person crosses through the wireless network, the system generates a vector $Q_{state} = [q_1, q_2, \ldots, q_L]^T$ where L is the number of links and q_k is 0 when link k is not detected as crossed and 1 when it is detected as crossed. The system also generates $T_{time} = [t_1, t_2, \ldots, t_L]^T$ where t_k is the time in seconds when link k is detected as crossed. We use Q_{state} and T_{time} in the linear regression and line stabbing algorithms to estimate the person's path as described in the following subsections.

2.3.2 Line Stabbing Estimation

In computational geometry, given a set of line segments, the line stabbing problem is to define the set of lines $y = mx + b$ that intersect (or *stab*) all the line segments [1]. In our case, the line segments are the link line segments $\{s_k\}_k$, and we wish to estimate a line which corresponds to the straight path of a person passing through a wireless network. The key challenge in our problem is that the system may record false link crossings or miss link crossings.

To solve this problem, we use the principle of point-line duality. A point with coordinates (a, b) is transformed to a line $l^* = ax + (-b)$ and a line $l' = ax + b$ is transformed to a point with coordinates $(a, -b)$. A line segment, which is defined by two endpoints p_1 and p_2 is transformed into a dual-wedge, where the boundaries of the dual-wedge are the lines l_1^* and l_2^* and the region between the boundaries are the infinite number of lines that pass through the intersection of l_1^* and l_2^*. Overlapping dual-wedges form a *stabbing region* such that any point p_{stab} within the region transforms into a line l_{stab} that stabs the set of line segments that correspond to the overlapping dual-wedges.

In this work, the L links in the network are represented as line segments s_k, where k corresponds to the kth link. The line segment s_k is transformed into its dual-wedge w_k. For speed of processing, we use a discretized grid of points, denoted by the matrix M_k, to define w_k: the grid point $M_k(a, b)$ is assigned the value 1 if (a, b) is inside w_k and 0 if (a, b) is outside w_k. The grid points for all M_k are bounded horizontally by $[a_{min}, a_{max}]$ and vertically by $[b_{min}, b_{max}]$. An example of a discrete dual-wedge is shown in Figure 2.1. We combine all L matrices in a database C, where the 1^{st} and 2^{nd} dimensions are the grid points and the 3rd dimension is the kth matrix, M_k. If we were to examine $C(0.3, 0.6)$, we would see a $1 \times L$ binary vector, $C(0.3, 0.6) = [c_1, c_2, \ldots, c_L]$. If $c_k = 1$, then the point $(0.3, 0.6)$ is inside w_k, and is outside w_k if $c_k = 0$. Applying duality to point $(0.3, 0.6)$, the line $l^* = 0.3x + (-0.6)$ stabs all line segments s_k whose corresponding c_k value is 1. Suppose that the link crossing detection system could perfectly detect link crossings. Then we could define a set of lines that stab the crossed links by finding all points in $C(a, b)$ where $Q_{state} = C(a, b)$. But since the link crossing detection system misses and falsely detects link line crossings, we are left to find all points in $C(a, b)$ such that the difference in values in $C(a, b)$ and Q_{state} are minimized. We define the stabbing region to be the set of

points (a, b) such that the Hamming distance between $C(a, b)$ and Q_{state} is minimized.

$$\arg\min_{(a,b)}\{d(Q_{state}, C(a, b))\} \tag{2.2}$$

where $d(Q_{state}, C(a, b)) = |\{i : q_i - c_i \neq 0\}|$, *i.e.*, the number of disagreements between the two vectors. In many cases, performing (2.2) yields multiple points (a, b) that define the stabbing region. We require one point, p_{stab}, whose dual is an estimate of the path traveled by the person. In this paper, we choose the centroid of points produced by (2.2) to be p_{stab}, whose dual is l_{est}. Estimating p_{stab} with a maximum liklihood or Bayesian estimator, is left to future work.

2.3.3 Linear Regression Estimation

In addition to the line stabbing adaptation, we also use ordinary least squares to estimate the initial position and trajectory of a person walking through the network using link crossing information in Q_{state} and the detected time of crossing in T_{time}. The path the person travels is parameterized such that when he crosses link k at time t_k, his coordinate (x, y) is defined by

$$\begin{aligned} x &= t_k v_x + p_x \\ y &= t_k v_y + p_y \end{aligned} \tag{2.3}$$

where the unknown parameters $\mathbf{p}[0] = [p_x, p_y]^T$ are the coordinates of the person at $t = 0$ and $[v_x, v_y]^T$ are the rate of change of the x and y coordinates, respectively. For all links k for which $q_k = 1$, we combine the line equation of all links detected as crossed, their recorded crossing time, and (2.3) to form a matrix equation

$$\underbrace{\begin{bmatrix} a_1 t_1 & -b_1 t_1 & a_1 & -b_1 \\ a_2 t_2 & -b_2 t_2 & a_2 & -b_2 \\ \vdots & \vdots & \vdots & \vdots \\ a_R t_R & -b_R t_R & a_R & -b_R \end{bmatrix}}_{\alpha} \underbrace{\begin{bmatrix} v_y \\ v_x \\ p_y \\ p_x \end{bmatrix}}_{\theta} = \underbrace{\begin{bmatrix} c_1 \\ c_2 \\ \vdots \\ c_R \end{bmatrix}}_{\beta}. \tag{2.4}$$

The value R must be ≥ 4 and is the number of links detected as crossed. Given that the link crossing detection and timing system are imperfect, we minimize the error in θ by using an ordinary least squares estimation:

$$\hat{\theta} = (\alpha^T \alpha)^{-1} (\alpha^T \beta). \tag{2.5}$$

The line that estimates the path the person took in the network is defined as $l_{est} = (\hat{v}_y/\hat{v}_x)x - (\hat{v}_y/\hat{v}_x)\hat{p}_x + \hat{p}_y$.

2.3.4 Quantifying Estimation Accuracy

In this section, we describe how we quantify the accuracy of the line estimate l_{est} obtained from the algorithm in Section 2.3.2 or 2.3.3. While many quantification methods exist, we calculate accuracy as the root-mean-square error (RMSE) of a discretized line segment that passes through the area. We calculate the bottom-left-most and top-right-most intersection points between that of the true path and the network as well as the estimated path and the network. These coordinates are denoted as $\mathbf{z}_{ll}^{path}$, $\mathbf{z}_{ur}^{path}$, and $\mathbf{z}_{ll}^{est}$, $\mathbf{z}_{ur}^{est}$. We choose P evenly distributed points along the lines connecting the coordinates of $\mathbf{z}^{path}$ and $\mathbf{z}^{est}$ and save both set of points in the $P \times 2$ matrices D_{path} and D_{est}. We calculate the RMSE as,

$$\text{RMSE} = \sqrt{\frac{1}{P}\|D_{path} - D_{est}\|_F}, \tag{2.6}$$

where $\|\cdot\|_F$ indicates the Frobenius norm.

2.4 Results

In this section, we describe our simulation framework, and then use it to show the accuracy of the line stabbing and linear regression methods.

2.4.1 Simulation Framework

In simulation, 30 nodes are placed inside of an 276 m^2 area as shown in Figure 2.2. A link $k = (i, j)$ is formed between the nodes only when $\|\mathbf{z_i} - \mathbf{z_j}\| < d_{max}$, where d_{max} is the connectivity distance. We use $d_{max} = 10$m in this simulation. The endpoints of the true path for each simulation are normally distributed $N(0, 1)$ around the points $(0, -5)$ and $(30, 10)$. We also adjust P_0 and δ in (2.1) for each trial to simulate scenarios where the detection rate (*i.e.*, the ratio of accurately detected link line crossings to the total number of true link line crossings) and false alarm rate (*i.e.*, the ratio of the number of false alarms to the product of the number of samples taken by the wireless network and the number of links) are high and low (see Figures 2.3 and 2.4). For each trial, we record the false alarm rate, the detection rate, and the RMSE with the associated value of P_0 and δ. In this work, anywhere from sixty to seventy link lines are crossed for each trial.

2.4.2 Line Stabbing Performance

Figure 2.5 shows the relationship between P_0 and δ and $RMSE_{avg}$. For $P_0 \geq 0.75$, $RMSE_{avg}$ is $\approx$0.8 m for small δ and increases to $>$2.0 m for large δ. We note the unexpected influence of the parameter P_0 — for almost all values of δ, the lower the value of P_0, the lower the $RMSE_{avg}$. This unexpected behavior is due to the false alarm rate vs. P_0 and δ, as seen in Figure 2.3. Lower values of P_0 result in lower false alarm rates over all δ. Although the detection rate is higher for larger P_0 (see Figure 2.4), $RMSE_{avg}$ increases for larger P_0 because of the higher false alarm rate.

2.4.3 Regression Performance

In Figure 2.6, we show the $RMSE_{avg}$ of all simulations with the given P_0 and δ value. We observe that the $RMSE_{avg}$ has a minimum of $\approx$0.5 meters when δ is small for all values of P_0. As δ increases, $RMSE_{avg}$ also increases until it peaks at $\approx$2.5 meters when $\delta = 2$ meters for $P_0 \geq 0.75$. This trend can be attributed to the average false alarm rate at each value of δ, as observed in Figure 2.3. For all values of P_0, the false alarm rate increases as δ increases. A higher false alarm rate tends to increase $RMSE_{avg}$ until it reaches a maximum. It should also be noted that although the system achieves a high detection rate for large δ (see Figure 2.4), the $RMSE_{avg}$ does not reduce significantly.

2.4.4 Performance Comparison

We draw a few conclusions about the different performance of the line stabbing and linear regression algorithms. Using the linear regression algorithm, $RMSE_{avg}$ maxes out at $\approx$2.5 meters whereas the $RMSE_{avg}$ in the adapted line stabbing algorithm would eventually exceed 2.5 meters for $\delta > 4$ meters (as observed in Figures 2.5 and 2.6). However, if $0.1 < \delta < 4$, the adapted line stabbing algorithm will provide a more accurate best line estimate (regardless of the the detection rate). In other words, the line stabbing approach is more robust to false alarms; but in the absence of false alarms, the linear regression algorithm provides the better accuracy. Note that low δ implies that links are only perturbed when a person is very close to the line between the transmitter and receiver.

2.5 Conclusion

In this paper, we present algorithms for device-free tracking using a wireless network. We study the algorithms via simulation using a simple probability of link line crossing detection model. Simulations show it is possible to track the straight path of a person passing through a wireless network despite the presence of false and missed line crossing detections. When there are few false alarms, we can accurately estimate the track of the person to within a RMSE of 0.8 meters using the adapted line stabbing algorithm and 0.5 meters using the linear regression algorithm. However, the line stabbing algorithm is more robust to a high false alarm rate compared to the linear regression approach.

2.6 Acknowledgements

This material is based upon work supported by the National Science Foundation under Grant Nos. 0748206 and 1035565.

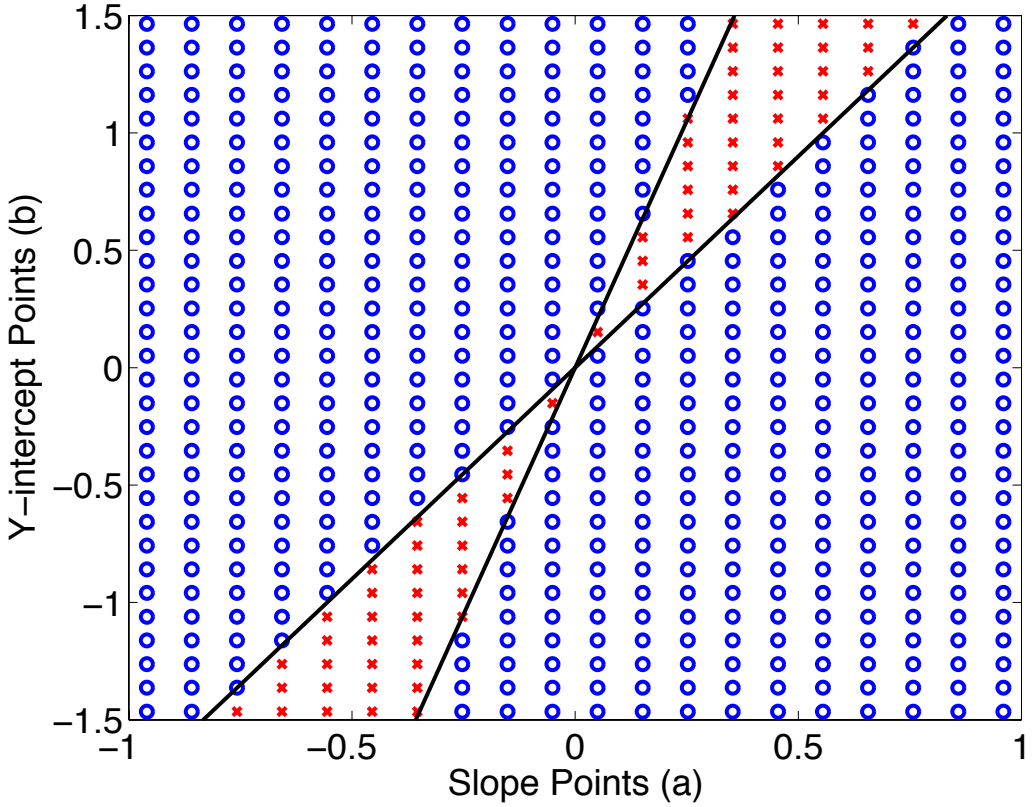

Figure 2.1. An example matrix M_k containing the dual-wedge w_k. Blue o's are where $M_k(a,b) = 0$ and red x's are where $M_k(a,b) = 1$. The black lines are the dual of the endpoints of line segment s_k.

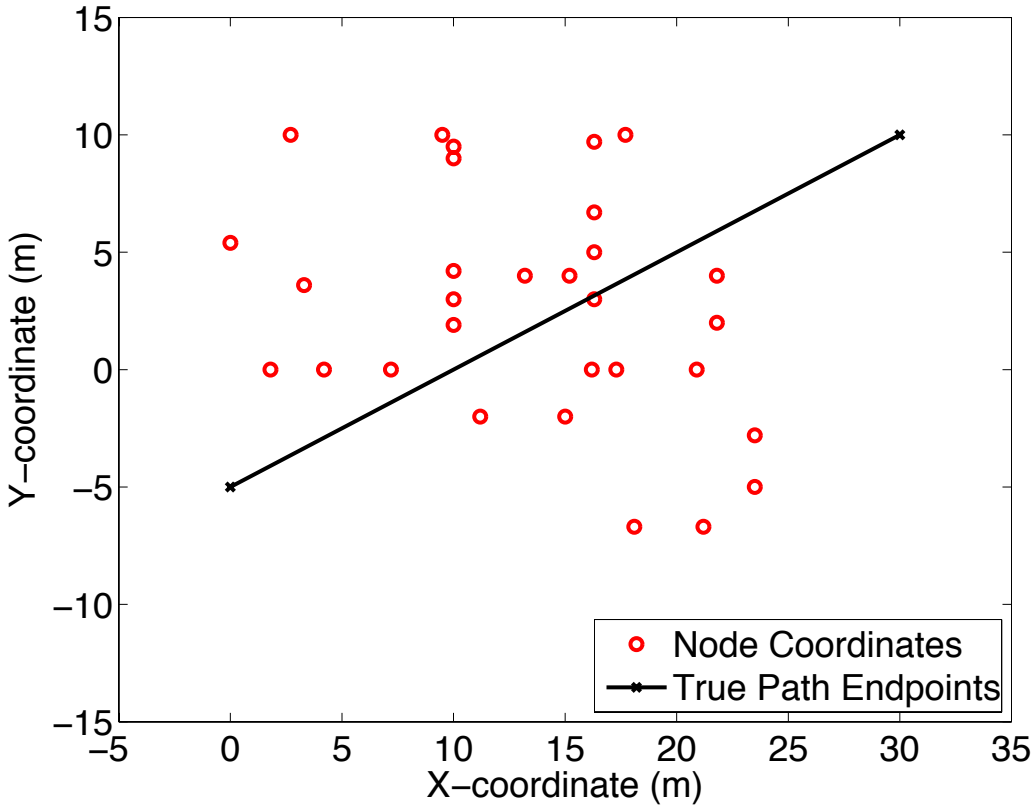

Figure 2.2. Node coordinates in the simulation network. Endpoints of the true path are normally distributed around the lower and upper (x).

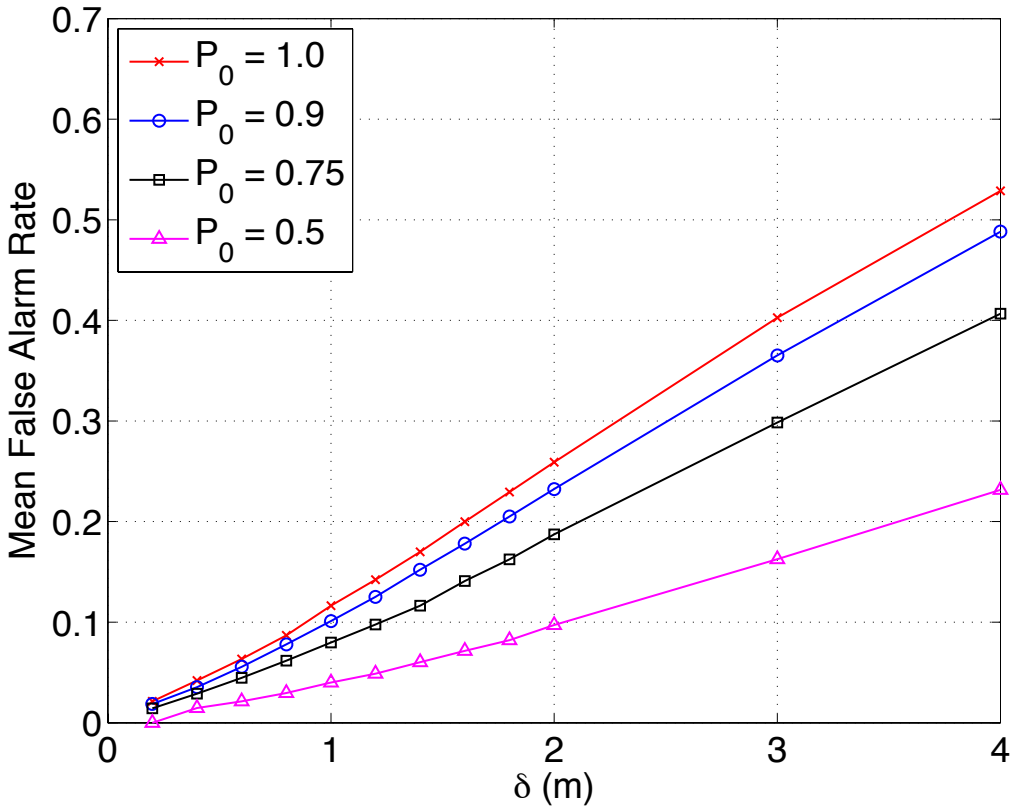

Figure 2.3. Mean false alarm rate as a function of P_0 and δ.

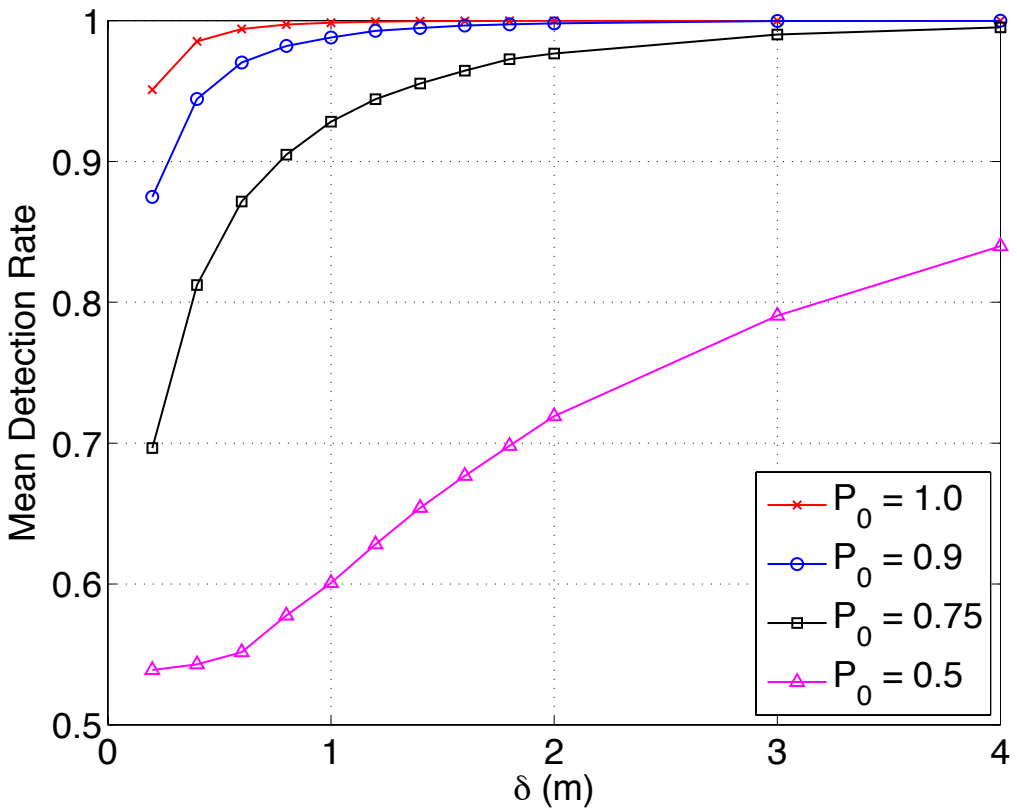

Figure 2.4. Mean detection rate as a function of P_0 and δ.

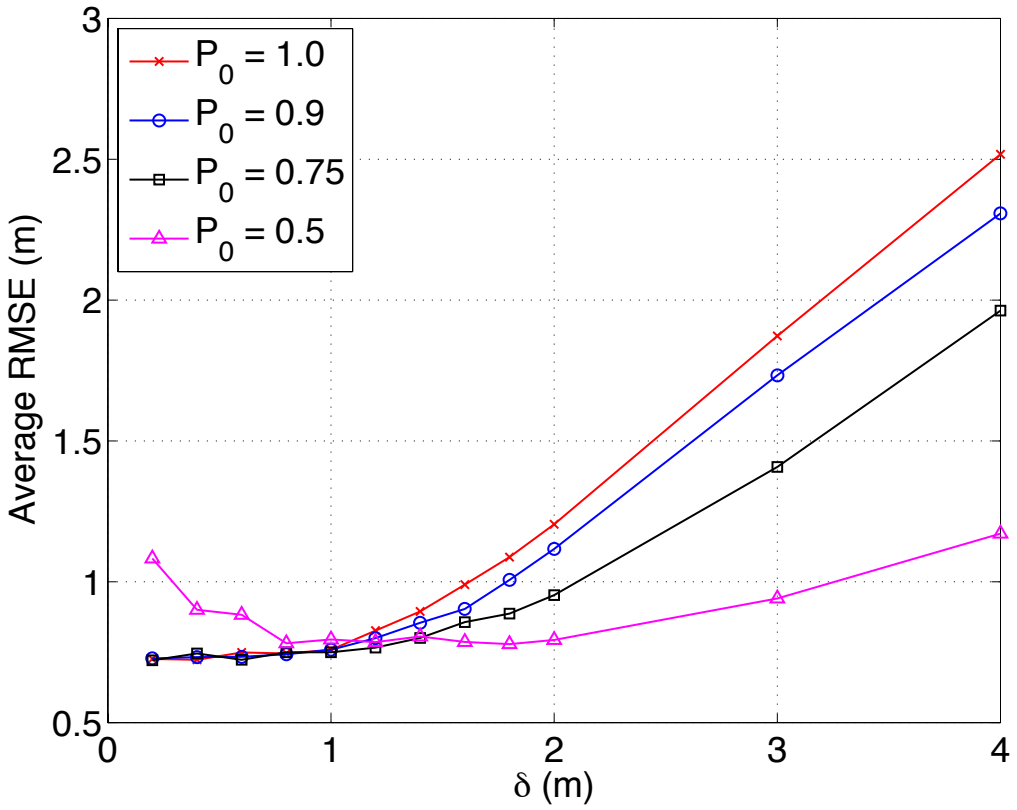

Figure 2.5. Average RMSE for the line stabbing algorithm as a function of P_0 and δ.

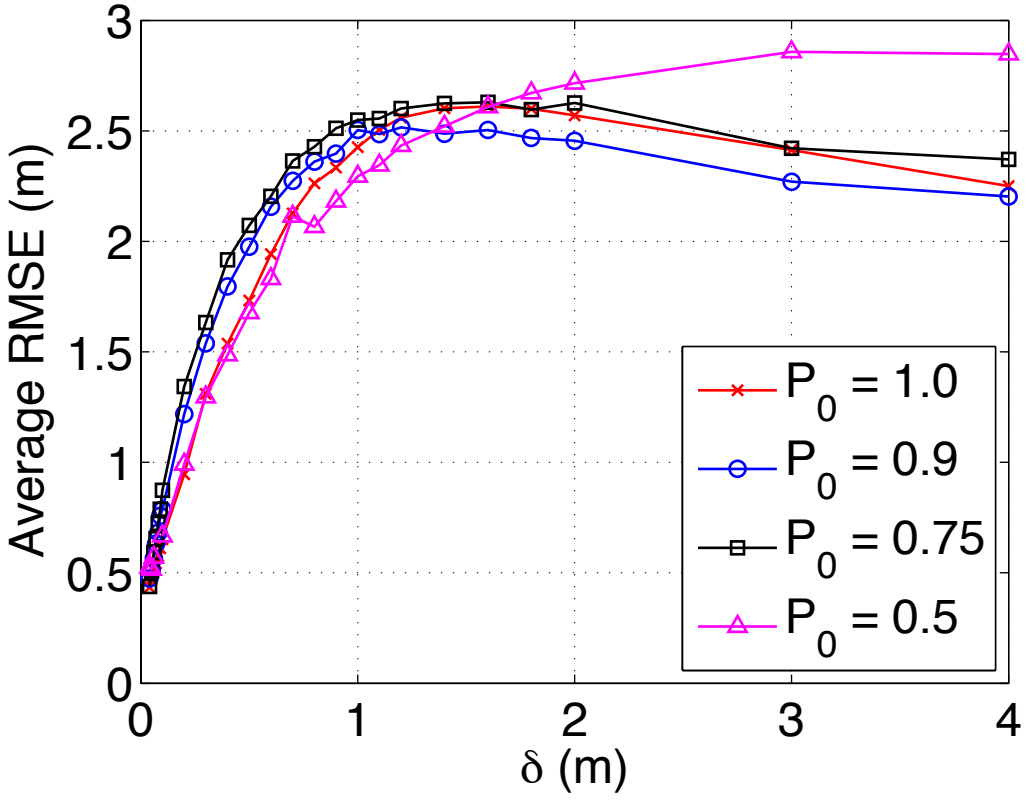

Figure 2.6. Average RMSE for the regression algorithm as a function of P_0 and δ.

2.7 References

[1] H. Edelsbrunner, H. Maurer, F. Preparata, A. Rosenberg, E. Welzl, and D. Wood. Stabbing line segments. *BIT Numerical Mathematics*, 22(3):274–281, 1982.

[2] O. Kaltiokallio and M. Bocca. Real-time intrusion detection and tracking in indoor environment through distributed rssi processing. In *2011 IEEE 17th Intl. Conf. Embedded and Real-Time Computing Sys. and Applications (RTCSA)*, volume 1, pages 61 –70, Aug. 2011.

[3] O. Kaltiokallio, M. Bocca, and N. Patwari. Follow @grandma: Long-term device-free localization for residential monitoring. In *Local Computer Networks Workshops (LCN Workshops), 2012 IEEE 37th Conference on*, pages 991–998, 2012.

[4] N. Patwari and J. Wilson. Spatial models for human motion-induced signal strength variance on static links. *Information Forensics and Security, IEEE Transactions on*, 6(3):791–802, 2011.

[5] M. Youssef, M. Mah, and A. Agrawala. Challenges: device-free passive localization for wireless environments. In *MobiCom '07: ACM Int. Conf. Mobile Computing and Networking*, pages 222–229, 2007.

[6] Y. Zhao, N. Patwari, J. M. Phillips, and S. Venkatasubramanian. Radio tomographic imaging and tracking of stationary and moving people via kernel distance. In *Proc. of the 12th Int. Conf. on Inform. Process. in Sensor Networks*, IPSN '13, pages 229–240, New York, NY, USA, 2013. ACM.

CHAPTER 3

THROUGH-WALL PERSON LOCALIZATION USING TRANSCEIVERS IN MOTION

Reprinted, with permission, from P. Hillyard, D. Maas, S. Premnath, N. Patwari, and S. Kasera, "Through-wall person localization using transceivers in motion," Arxiv.org, Tech. Rep. arXiv:1511.06703 [cs.ET], Nov. 2015.

3.1 Abstract

We develop novel methods for device-free localization (DFL) using transceivers *in motion*. Such localization technologies are useful in various cross-layer applications/protocols including those that are related to security situations where it is important to know the presence and position of an unauthorized person; in monitoring the daily activities of elderly or special needs individuals; or in emergency situations when police or firefighters can use the locations of people inside of a building in order to save lives. We propose that transceivers mounted on autonomous vehicles could be both quickly deployed and kept moving to "sweep" an area for changes in the channel that would indicate the location of moving people and objects. The challenge is that changes to channel measurements are introduced both by changes in the environment and from motion of the transceivers. In this paper, we demonstrate a method to detect human movement despite transceiver motion using ultra-wideband impulse radar (UWB-IR) transceivers. The measurements reliably detect a person's presence on a link line despite small-scale fading. We explore via multiple experiments the ability of mobile UWB-IR transceivers, moving outside of the walls of a room, to measure many lines crossing through the room and accurately locate a person inside within 0.25 m average error.

3.2 Introduction

Multistatic RF localization technologies, such as radio tomographic imaging [1], device-free passive localization [2], multiple-input multiple-output (MIMO) radar [3], and multistatic ultra-wideband impulse radar (UWB-IR) [4], offer the potential to locate moving people and objects over wide areas using RF channel measurements. In highly cluttered multipath environments, these systems rely on the change in the RF channel to identify and locate moving people and objects. Such localization technologies are useful in various cross-layer applications/protocols including those that are related to security situations where it is important to know the presence and position of an unauthorized person; in monitoring the daily activities of elderly or special needs individuals; or in emergency situations when police or firefighters can use the locations of people inside of a building in order to save lives.

Device-free localization (DFL) (where people being localized do not carry any wireless transmitters) research has, typically, built algorithms and systems around the assumption that the position of transceivers performing DFL remain static, and that measured changes are solely due to movements in the environment [5]–[7]. Under these conditions, changes in channel measurements are due to the movement of people or objects in the environment [8], [9]. The location of moving people or objects can be accurately estimated based on which wireless links show significant changes in channel measurements. The use of static transceivers poses certain practical challenges. First, a large number of transceivers may be required to cover the entire monitored area. Second, and very importantly, there may not be sufficient time to deploy a large number of transceivers when people must be localized very quickly (e.g., in emergency situations).

In this paper, we develop methods for DFL using only a few transceivers *in motion*. In our methods, the RF channel is measured by mobile transceivers (e.g., aerial or terrestrial vehicle-mounted) that can autonomously change position to enable rapid deployment, adapt to a moving target, or refine location estimates. For example, pairs of mobile transceivers, like $\mathbf{z}_1$ and $\mathbf{z}_2$ in Figure 3.1, can make rapid channel measurements while in motion then detect the obstruction of the *link line*, (i.e., the line from the transmitter to receiver), an operation we call *link line presence* detection. By measuring link line presence on many moving link lines, the system can effectively sweep a building for activity. We

assume that a transceiver can determine its coordinates relative to a fixed local coordinate system, and can eventually return to a previous position, to re-measure from that position. The mobile node's self-positioning and self-navigation will not be perfect, and part of this work explores how accurate the self-positioning and self-navigation need to be in order to accurately localize people. In a sophisticated deployment, a swarm of robotic vehicle-mounted transceivers may be used, some in motion and some static during any given period of time.

When mobile transceivers are used for measurements of a radio channel, multiple factors can cause variations in the channel measurements. First, with mobile transceivers, the radio channel between two transceivers changes due to small-scale multipath fading, a result of the change in position of the transceivers. Second, the radio channel also changes, by similar magnitudes, due to motion of a person nearby because of temporal fading. Furthermore, a mobile transceiver does not necessarily measure the channel at fixed locations. Distinguishing the changes in the channel that result from alterations in the environment and those that result from location variations is a challenging task. We tackle this challenge by examining the differences in the wireless channel multipath characteristics due to movement of people in a monitored region and due to small-scale fading caused by motion of transceivers monitoring the region.

Existing research shows that fading rate variance is proportional to angular spread of a wireless signal [10]. Angular spread can be shown to be very small in the first few nanoseconds of a channel impulse response (CIR) [11], [12] presumably because for multipath to arrive close in time to the line of sight path, the paths must be contained within a narrow ellipse around the transmitter and receiver [13]. Thus, while small-scale fading will have dramatic effects on CIRs at medium and large time delays, we can expect it to have a minor effect at small time delays.

In contrast, when a person or object moves across the link line, the person will scatter, absorb, and reflect the direct path and other paths with low excess delay.[1] Specifically, the person will attenuate multipath with small time delays as a result of shadowing. We distinguish the effects of small-scale fading from movement of transceivers from that of

[1]We use the term direct path to mean the multipath that travels along the link link either in an unobstructed or obstructed manner.

shadowing due to a person being near or on the line of sight between the transmitter and the receiver, by examining the first few nanoseconds of the impulse response measurement.

We use the change in the first few nanoseconds of the measured impulse response, thus, to test for link line presence, even with transceivers in motion. The use of UWB-IR radios allow us to measure the multipath power in the first few nanoseconds of the measured impulse response. Quantifying motion on a link line with moving endpoints serves as a fundamental building block for *environmental imaging* using networks of mobile transceivers for the applications described above.

In this paper, we make the following contributions. We first develop the components of our methodology for accurately localizing people, who are not carrying any transmitters, through walls using mobile transceivers. This methodology applies radio tomographic imaging to measurements of energy in the first few nanoseconds of the measured channel impulse responses gathered by mobile transceivers in order to localize people within the monitored area. We implement our methodology using two UWB transceivers and perform extensive experiments in different settings. Through our measurement campaigns, we show that link line presence can be detected with great accuracy despite movement of the transceivers. Furthermore, we show that mobile transceivers can be used to localize a person to within 0.25 m, on average, of their actual position.

The use of mobile transceivers both complements *and* sets our work apart from existing methods for multistatic UWB radar, which perform through-wall imaging using stationary transceivers [4], [14]. In contrast to traditional multistatic UWB radar, our paper provides methods that use measurements collected by *mobile* UWB transceivers. In addition, previous multistatic UWB research ignored the information contained in the direct path, and in fact, assumed that an intruder whose excess delay was very small (e.g., on the link line) could not be located [14]. We show that the energy change at these low excess delays can be used to reliably detect link line presence, even with a mobile device.

This paper proceeds as follows. Section 3.3 describes our method of measuring the CIR; how we distinguish small-scale multipath fading from temporal fading; and we describe the framework by which we perform DFL. In Section 3.4, we perform experiments to first evaluate our methods for distinguishing small-scale multipath fading from temporal

fading and second, to show that we can perform DFL with manually moved transceivers and accurately estimate a person's location. We discuss existing research on localization, mobile devices, and link line presence detection methods in Section 3.5, and we conclude this work and discuss future work in Section 3.6.

3.3 Methodology

In this section, we describe our use of UWB-IR transceivers to measure the CIR. In a through-wall experiment, we test and evaluate the feasibility of distinguishing small-scale multipath fading and link line presence. We analyze the test to set conditions under which we can distinguish the two causes of variateion in channel measurements. We end by presenting the framework by which we use mobile transceivers to perform through-wall DFL.

3.3.1 Measured Impulse Response

The multipath channel causes multiple copies of the transmitted signal to be received, each copy with its own amplitude and propagation delay. Specifically, the received signal $h(t)$ is written as [15], [16],

$$h(t) = \sum_{j=1}^{N} \alpha_j s(t - \tau_j) \tag{3.1}$$

where N is the number of multipath, α_j and τ_j are the amplitude and propagation delay of the jth multipath, and $s(t)$ is the transmitted signal.

Ideally, to measure the channel impulse response, we would make our transmitted signal $s(t)$ be equal to the Dirac impulse function $\delta(t)$. This would allow the receiver to uniquely determine the amplitude of each component. However, such a transmitted signal would consume infinite bandwidth. The closest we can get in practice is to use UWB-IR.

Our UWB-IR transmitter sends the Gaussian monocycle pulse $s(t)$ which is designed to be band limited to between 3 to 6 GHz; $s(t)$ closely resembles the pulse that we have shown in Figure 3.2. The majority of the energy of the wide-band pulse occurs in a window whose duration is approximately 1 ns. Paths that arrive within 1 ns of each other overlap and add together, either constructively or destructively. One can see from the shape of $s(t)$ in Figure 3.2 that two paths arriving 100 ps apart would tend to nearly cancel each other, while two paths 200 ps apart would add constructively. Note that 100 ps translates into

0.03 m of path length, so even a small position change can result in the difference between constructive and destructive interference.

However, multipath near the direct path contribute less small-scale multipath fading. Small-scale multipath fading occurs because spatial translation of an antenna changes the relative time delays of multipath *at different rates*, thus bringing their sum in and out of destructive and constructive interference. The rate of change of τ_j is a function of the angle of arrival of the jth path. If two multipath arrive from the same angle, their time delays change at the same rate, and thus their sum does not change. For paths arriving within a few nanoseconds of the direct path, the multipath must be contained in a very narrow ellipsoid with the transmitter and receiver locations as foci, and thus the angular spread of the arriving multipath is very low [13]. Thus we should see very slow small-scale multipath fading in the first few nanoseconds of the measured UWB received signal $h(t)$.

In this paper, we use two UWB-IR transceivers (Time Domain, P220) [17] with sampling period $T_s = 15.89$ ps. Figure 3.3 shows an example of the post-processed measured impulse response.

The two transceivers are not time-synchronous (to the ps level), and thus processing is needed to time-align different measurements, using the first arriving multipath as time zero. In this paper, we do this by cross-correlating the received signal $h(t)$ with the Gaussian monocycle pulse $s(t)$ and finding the first time at which the correlation coefficient exceeds a threshold ρ. When ρ is too small, we time-align with a later arriving multipath; when ρ is too large, we time-align earlier than the first arriving multipath. We use $\rho = 0.75$ in this paper based on observations of time-aligning accuracy. The occasional CIR measurements that were heavy corrupted with interfering signals were discarded.

A convenient way to represent the measured impulse response is using a power-delay profile (PDP). The PDP shows the energy of the received signal as a function of excess delay τ. By doing so, we remove unnecessary details about the pulse shape $s(t)$. The energy in time delay bin m, e_m, is calculated as,

$$e_m = \int_{mT_w}^{(m+1)T_w} |h(t)|^2 \mathrm{d}\tau. \tag{3.2}$$

The value of e_m is the integral of the received power that falls in the mth T_w-wide window.

3.3.2 Proof-of-Concept Experiment

Our intuition is that the first few nanoseconds of the PDP provides a means to be able to distinguish between small-scale multipath fading and link line presence. To test this, we set up a simple through-wall experiment.

We place our two UWB-IR transceivers in adjoining offices of an empty room as shown in Figures 3.4 and 3.5 with antennas at 1.1 m height. We measure $\log_{10}$ of the PDPs with time bin width $T_w = 100$ ps. We measure PDPs (see Figure 3.6(a)) at ten receiver positions spaced by 0.02 m while the room is empty. Over the course of 0.20 m displacement, the energy in any given bin changes slowly due to small-scale multipath fading. In particular, the changes in the first few nanoseconds have relatively slow changes.

Next, we run the same test, but with the person standing still on the link line in the middle of the empty room. In this case, with the same settings and same displacement of the receiver, we see the PDPs shown in Figure 3.6(b). The vertical scale in Figure 3.6(b) is identical to that of Figure 3.6(a). One can see that the energy in the first few ns is dramatically smaller.

We use a portion of the PDPs shown in Figure 3.6 by plotting the energy in the first three nanoseconds. For simplicity, we define $E = 10\log_{10}(e_0)$ for the case when $T_w = 3$ ns, that is, E is $10\log_{10}$ of the energy in the first three nanoseconds of the impulse response measurement. We plot E as a function of receiver displacement for the two cases: empty-room vs. link line presence, in Figure 3.7.

Comparing the empty-room and link line presence energy profiles, we observe that E is much greater when the room is empty at any receiver displacement. The difference in magnitude between the energies shows that we can use the energy in the first three nanoseconds of the CIR measurement as an indicator of link line presence even in the presence of small-scale fading. It will later be shown through experimentation that we can use the measurements E to detect link-line presence. We note that for the remainder of this work, we use $E = 10\log_{10}(e_0)$ and $T_w = 3$ ns.

3.3.3 Radio Tomographic Imaging

Radio tomographic imaging (RTI) has been shown to be an effective means for estimating the location of a person in the vicinity of an RF network that uses several stationary

transceivers [18]–[20]. It is also possible to apply RTI to measurements made with mobile transceivers, e.g., when the transceivers are attached to autonomous vehicles.

While several RTI methods have been developed, we apply shadowing-based RTI, which leverages the attenuation of RF transmissions moving people in order to infer their location. This form of RTI lends itself well to the UWB measurements at our disposal since we expect to be able to distinguish link line presence and no link line presence despite the effects of small-scale multipath fading.

We denote $E_l[n]$ to be the energy measurement E for link l at time n. Then, the energy decrease between two measurements $n-1$ and n is given as

$$\Delta E_l = E_l[n-1] - E_l[n]. \tag{3.3}$$

We note that a "link" is defined by the locations of the transmitter and receiver and refers to the two communicating transceivers. Thus a link $l = (\mathbf{z}^{tx}, \mathbf{z}^{rx})$, where $\mathbf{z}^{tx}$ and $\mathbf{z}^{rx}$ are the coordinates of the transmitter and receiver. *Other measurements made between any two devices at approximately the same coordinates are considered to be made on the same link*. In the context of localization, when $\Delta E_l > 0$, we use this as evidence of link line presence and as input to radio tomographic imaging.

Let the change in energy on each link be formed into a measurement vector $\mathbf{y} = [\Delta E_1, \ldots, \Delta E_L]^T$. In order to generate an image, we assume that the total attenuation for each link is the sum of the attenuations caused by the voxels the link line passes through, i.e.,

$$y_l = \sum_{i=1}^{M} w_{l,i} x_i \tag{3.4}$$

where x_i represents the ith voxel in an image vector $\mathbf{x}$ containing M voxels and $w_{l,i}$ is a weighting factor for quantifying the contribution of x_i to the overall attenuation y_l for link l. We use the weighting method

$$w_{l,i} = \begin{cases} \frac{1}{A_l} & \text{if } d_{l,i}^{tx} + d_{l,i}^{rx} < d_l + \lambda \\ 0 & \text{otherwise} \end{cases} \tag{3.5}$$

where $d_{l,i}^{tx}$ and $d_{l,i}^{rx}$ are the distances between the centroid of voxel i and the transmitter and receiver of link l, d_l is the distance between the transmitter and receiver of link l, A_l is the area of the ellipse, and λ is the excess path length of the ellipse (used to control the width of the ellipse).

We can write the attenuations for all of the links in the network in matrix form as follows

$$\mathbf{y} = \mathbf{W}\mathbf{x} + \mathbf{n} \tag{3.6}$$

where $\mathbf{n}$ is the noise contribution and $\mathbf{W}$ is the $L \times M$ weighting matrix. We solve for $\mathbf{x}$ using a regularized least-squares approach [1], [18]–[20].

3.4 Experimental Verification

In this section, we perform two measurement campaigns to: first, test that the changes in the channel due to small-scale multipath fading can be distinguished from differences in the channel measurement due to temporal fading; and second, test if we can perform DFL with mobile transceivers by localizing people based on the links whose channels show changes because of temporal fading.

3.4.1 Link Line Presence Detection Experiment

In the first measurement campaign, our goal is to detect when a person is on a link line formed by two wireless UWB transceivers while one of the transceivers is moving. Being able to detect link line presence while one transceiver is moving demonstrates the feasibility to distinguish temporal fading from small-scale multipath fading. We choose a cluttered room with a couch, several desks, bookcases, and chairs inside our engineering building as the experimental site. The layout of the room is shown in Figure 3.8.

We place two transceivers outside of the office space such that the link line is separated by two walls. The receiver sits on a platform that is suspended from the ceiling (see Figure 3.9) while the transmitter is placed on a stool. Both the transmitter and receiver are placed 1.1 m off the floor. We attach strings to the hanging platform so that the receiver can be displaced by a short distance when the strings are pulled.

We choose to examine the effects of displacing the transmitter by 0.10 m and 0.20 m so that we could compare how a system would perform with different degrees of small-scale fading. We perform two link line presence detection experiments using these two displacement distances. In the first test, we move the platform repeatedly back and forth 0.10 m parallel to the wall. In the second test, we move the platform repeatedly back and forth 0.20 m parallel to the wall. In both cases, we move the platform back and forth every 2 seconds.

During the first test, a person walks at approximately 0.46 m/sec inside the office, crossing the link line 8 times (and a ninth time standing on the link line momentarily) at different points on the link line. During the second test, a person again walks at approximately 0.46 m/sec inside the office crossing the link line 6 times. The link line crossings are separated by at at least 10 seconds. With a video recorder, we capture the time the person crosses the link line which we use to compare the measured and actual time of crossing. Throughout the tests, the wireless channel is measured approximately 3 times per second.

3.4.2 Link Line Presence Detection Results

We found in Section 3.3.2 that E could be used to detect link line presence. Although any link line presence detector could be used, we choose to implement the moving average based detector from Section from Section 4.3.1 in [2] because of its straightforward implementation and its accuracy in detecting link line crossings (see Figure 3.10). The moving average based detector adds an E measurement to a short and long term buffer. The long term buffer stores the static behavior of the link while the short term buffer stores the current behavior. Upon adding a new E measurement to the buffers, the detector computes the relative difference between the means of the two buffers. When the relative difference exceeds a threshold τ, an event is detected. These events are stored in a buffer that is summed with every new added event. If the sum of the buffer exceeds another threshold, a link line presence is detected. We let $\tau = 0.016$ and use the best parameters described in [2].

We use this detector with the measurements recorded during this experiment. Figure 3.11 and Figure 3.12 show the results of the experiment. A link line presence is correctly detected when at least one link line crossing event occurs during the time the person is actually crossing the link line. This is reasonable considering that a person is within 3 ns of excess delay for potentially several seconds as they cross the link line (see the measurements E for the 140 second mark of Figure 3.11). Our algorithm accurately detects the nine occurrences of link line presence when the receiver is repeatedly moved through 0.10 m. In contrast to the previous experiment, errors result when we move the receiver repeatedly through 0.20 m. Of the six occurrences of link line presence, four link line presence events are accurately detected.

We observe two important facts from our two tests. First, we show that detecting link line presence is more accurate when the transceiver is displaced by 0.10 m than when the transceiver is displaced 0.20 m. The amount of small-scale multipath fading in the test with 0.20 m transceiver displacement is much greater than in the test with 0.10 m transceiver displacement. Thus, in the test with 0.20 m transceiver displacement, there are instances when temporal fading could not be distinguished from small-scale multipath fading. In addition, small-scale multipath fading can be severe enough to appear like the effects of temporal fading. Second, we show that we can reliably distinguish small-scale multipath fading from temporal fading when the transceivers are displaced by no more than 0.10 m. Clearly, there are alternative ways other than our algorithm to distinguish temporal fading from small-scale multipath fading, however, our results show the feasibility of accomplishing this task.

3.4.3 Person Localization

Knowing that we are able distinguish the effects of temporal fading and small-scale multipath fading, our goal in the second measurement campaign is to show that a system can perform DFL with mobile transceivers by collecting mobile UWB-IR measurements and computing a transceiver's relative coordinate locations to locate moving people based on the links whose channels show changes because of temporal fading. We describe how we adapt RTI for channel measurements made with mobile transceivers to create an image that shows the presence of a person inside a network.

3.4.3.1 Experiment

We use a classroom whose walls are made of brick for our experiment test site. The classroom has a few tables and chairs making it a semi-cluttered environment. Figure 3.13 shows the layout of the experimental site.

In our experiment, we manually move one of the UWB transceivers to collect mobile channel measurements. We select four transmitter positions and for each transmitter position, we manually move the receiver on a track at approximately 0.08 m/s along the walls of the adjacent room and hall as shown in Figure 3.13. The receiver measures the channel approximately every 100 ms while two laser-range finders approximately every 300 ms log the relative position of the receiver with respect to a fixed coordinate system.

Because the channel measurements and the laser-range finder coordinates are sampled at different times, we linearly interpolate to match each channel measurement to a receiver coordinate. We call the coordinate at which the receiver measures the channel a *mobile receiver coordinate*. We perform this process for when the room is empty and while a person stands at each of the 4 positions in Figure 3.13.

To create images using RTI, the transceivers must have static coordinates. Since our receiver coordinates are mobile (i.e., two receiver coordinates, and therefore link line endpoints, are most likely not the same), we choose R *reference receiver* coordinates and we associate each mobile receiver coordinate to one reference receiver coordinate.

We now describe how we form the measurement vector $\mathbf{y}$ in (3.6). We first define each transmitter location to be at one of four locations s where $s \in \{1, 2, 3, 4\}$. When the receiver is at the jth mobile receiver coordinate and the transmitter is at location s, we compute the energy measurement E of the channel and denote it $E_{s,j}$. We denote the jth mobile receiver coordinate when the transmitter is at location s as $\mathbf{z}_{s,j}^{mc}$; and we denote the rth reference receiver coordinate $\mathbf{z}_r^{rc}$.

We associate each $E_{s,j}$ to the nearest reference receiver by finding r such that

$$\arg\min_r \|\mathbf{z}_{s,j}^{mc} - \mathbf{z}_r^{rc}\| \tag{3.7}$$

where $\|\cdot\|$ is the Euclidean distance. The energy measurement $E_{s,j}$ then belongs to the set $\mathcal{E}_{r,s}$ where r is the rth reference receiver and s is the transmitter location. For simplicity, we shorten the notation of the set to $\mathcal{E}_l$ where l is the link formed by reference receiver r and the transmitter at position s. Finally, we denote the median of the values in set $\mathcal{E}_l$ as M_l.

We redefine the components of the measurement vector $\mathbf{y}$ presented in (3.6) to take into account multiple measurements per link. We first define the change in median energy ΔM_l to be

$$\Delta M_l = M_l^{cal} - M_l^{occ} \tag{3.8}$$

where M_l^{cal} is computed from measurements when the room is empty and M_l^{occ} is computed from measurements when a person is in the room. In the event no median can be computed because $\mathcal{E}_l = \varnothing$, we set $\Delta M_l = 0$. We are interested in finding the change in median energy between empty-room case and occupied-room case. Thus we define

the measurement vector $\mathbf{y} = [y_1, \ldots, y_L]^T$ where L is the number of links created by transmitter-reference receiver pairs and y_l for link l is

$$y_l = \begin{cases} \Delta M_l & \text{if } \Delta M_l > 0 \\ 0 & \text{otherwise} \end{cases} \tag{3.9}$$

3.4.3.2 Mobile RF Network Results

In this section, we show the images we produce using RTI and the effectiveness in estimating the location of the person. We choose the number of reference receivers $R = 67$; 30 in the room and 37 in the hall. We evenly space the reference receivers in each set along each wall, the hall wall and the room wall as shown in Figure 3.13, such that the distance between any two reference receivers is less than 0.12 m. This ensures that we collect sufficient measurements for each reference receiver but that the reference receivers are close enough to adjacent reference receivers to avoid the effects of small-scale fading for medium to large delays.

Figure 3.14 shows the images we produce using RTI. In all of these figures, excluding Figure 3.14(a), the image shows high intensity near the location of the person, which follows the intuition that the link lines that pass through the voxels covered by the person will experience the greatest change in energy. Using the voxel with the greatest intensity as the estimate of the person's location, we accurately estimate the location of the person to within the errors, shown in Table 3.1:

The average of the four error values is approximately 0.25 m. These results show strong evidence that we can reliably localize a person in a through-wall environment using few mobile transceivers.

3.5 Related Work

To the best of our knowledge, this paper presents a novel approach for using UWB-IR measurements for device-free or non-cooperative localization. Traditional multistatic radar methods require that the UWB radios remain static [4], [14], [21]–[23]. These methods measure the excess delays of any new multipath components assumed to be due to a new person in the environment, from multiple pairs of UWB transceivers. Each excess delay restricts the person to be within an ellipsoid of specified width, and assuming sufficient measurements, people's locations can be determined [4], [22]. However, the problem of

finding one changed excess delay among dozens or hundreds of multipath components and noise is not at all a trivial problem [23]. Our methods are complementary by allowing the UWB radios to be mobile, and by monitoring for changes in the first few nanoseconds of excess delay to detect line presence. These small excess delays are typically ignored in multistatic UWB [14]. We then use the many channels measured by mobile devices to create a map of an area and show that accuracies of 0.25 m can be achieved.

This work is also different from other localization schemes that use narrowband wireless devices. Localization of people inside a building has been demonstrated using calibration measurements on many link lines passing through the network [24], [25] as well as using RTI to image the location of people [1], [19], [20]. In these studies, many static devices were need to achieve high accuracy localization. In addition, narrowband devices provide one measurement for the entire channel. We build upon RTI by showing that through-wall imaging can be performed with fewer devices that move around the perimeter of the area.

Our work focusses on the first few ns of a measured CIR to provide information about the absence or presence of a person, whereas in [26], an image of an environment is produced using the time-delays between a transmitted pulse and a reflected pulse off of an object in the environment. The system is similar to synthetic aperture radar. This work shows that in an otherwise empty room, large conducting objects (e.g. a metal slab, and a large wooden cabinet) located a meter away from the wall can be imaged. Unlike our work, however, no experiments were performed with people.

3.6 Conclusion and Future Work

In this paper, we developed methods for device-free localization using a small number of transceivers in motion. We accomplished this by measuring the energy of the first few nanoseconds of a received UWB signal and observing the changes between past and current measurements. Through several measurement campaigns, we showed that it is possible to detect the presence of a person in the environment when both small-scale fading and shadowing affect the received signal of wideband devices. Our measurement campaigns demonstrated that when a receiver was kept to within a displacement of 0.20 m, we can accurately detect when a person is on a link line more than 80% of the time. In another campaign, we demonstrated that we can estimate the location of a person

to within 0.25 m of their actual location. These results were achieved using our mobile implementation of radio tomographic imaging.

We have used UWB radios as a means to measure energy in the first few nanoseconds of the received signal. Future work includes localizing people in a network using 802.11 links as a means to gather measurements. Additional work could explore alternate statistical methods to detect changes in the received signal.

3.7 Acknowledgements

We would like to acknowledge the formative role that Dr. Cliff Wang played in the generation of the idea to perform RTI using mobile transceivers. This work is supported by the US Army Research Office under Grant #W911NF-12-1-0361, and by the US NSF under Grant 0748206.

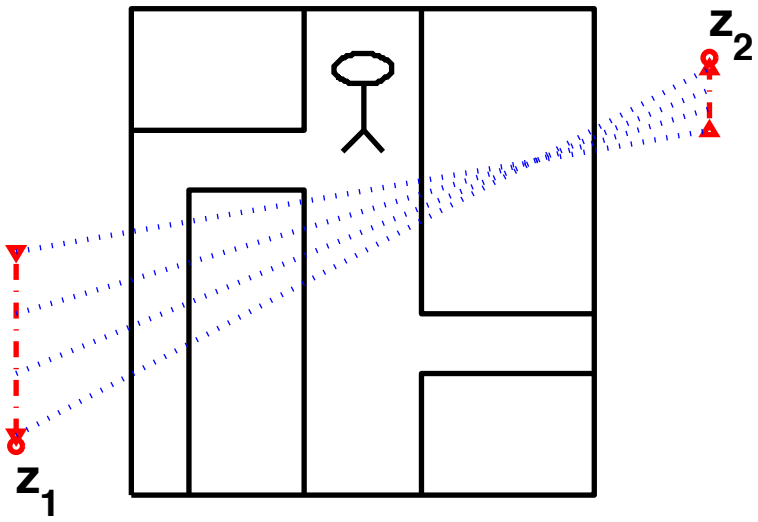

Figure 3.1. In an example deployment, mobile transceivers autonomously move around the perimeter of a building while making measurements of the channel. The person inside the building does not carry any wireless transmitters. Mobile transceivers $\mathbf{z}_1$ and $\mathbf{z}_2$ autonomously move around the perimeter of the building.

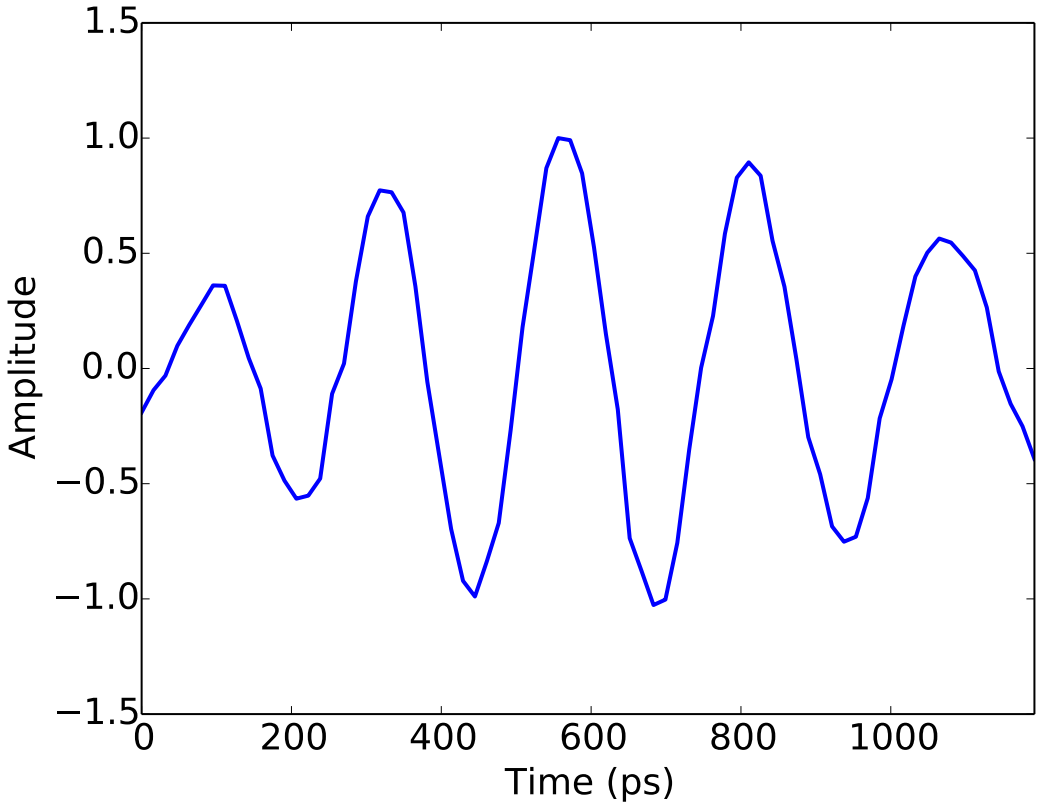

Figure 3.2. Measured Gaussian monocycle pulse $s(t)$ sent by our UWB-IR transmitter.

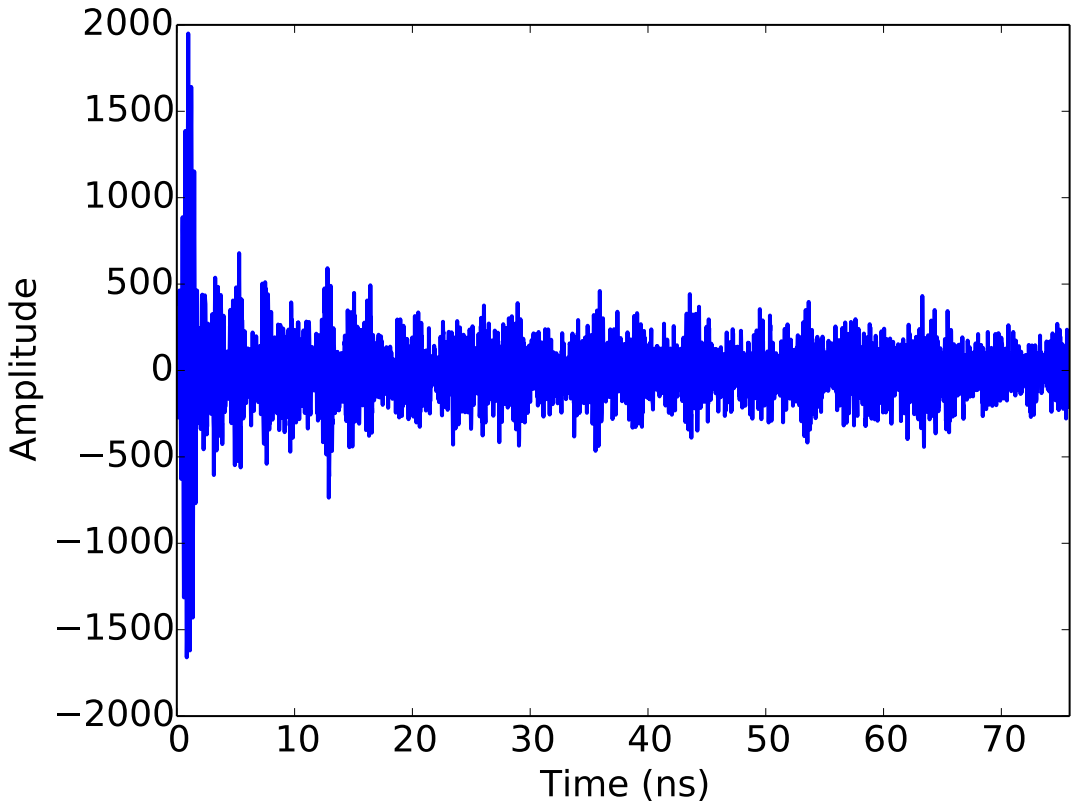

Figure 3.3. An example of a measured impulse response $h(t)$ using UWB-IR.

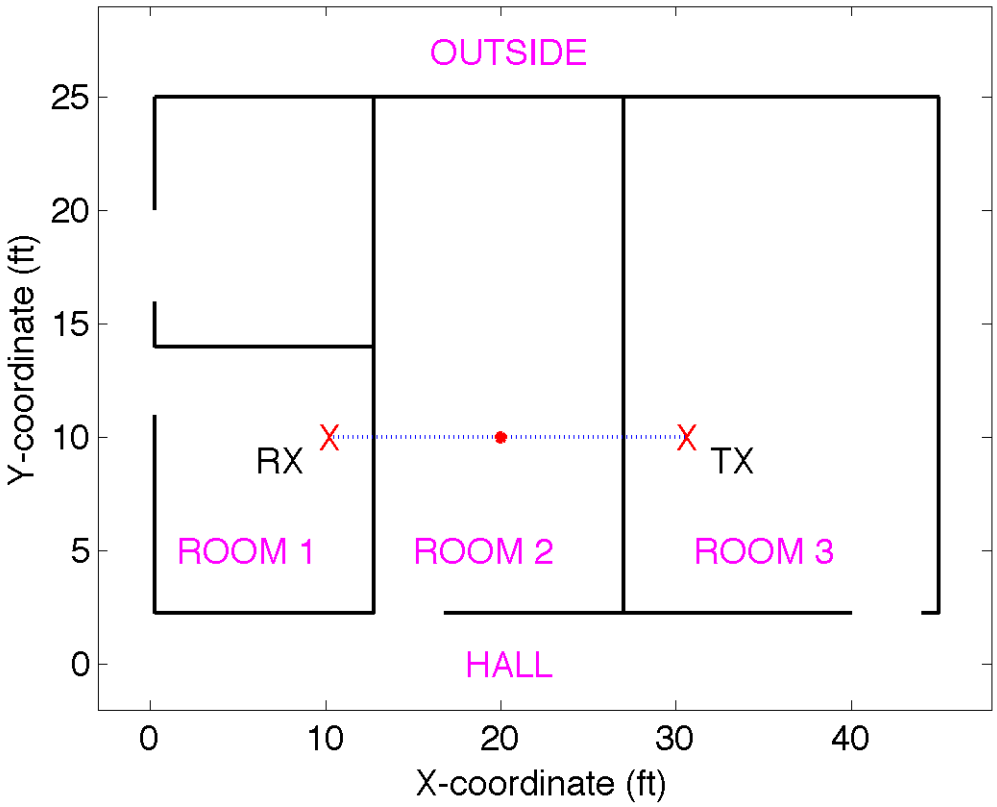

Figure 3.4. The floor plan showing UWB transceiver placement and the standing position of the person. The red dot represents where the person stands while the measurements are taken.

Figure 3.5. One of the transceivers used to collect UWB impulse response measurements.

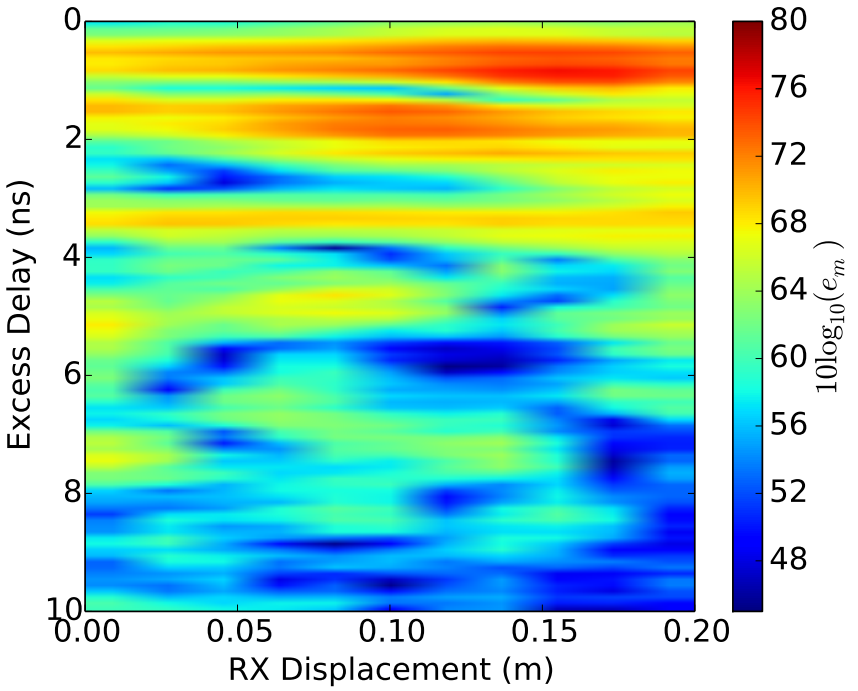

(a)

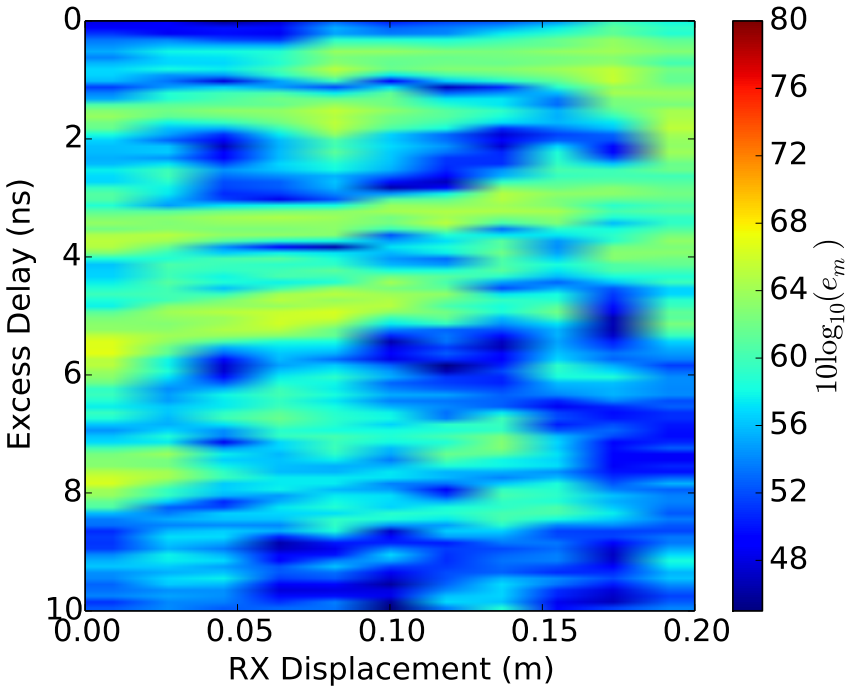

(b)

Figure 3.6. The energy observed in the CIR as a function of excess time delay and receiver displacement when (a) the room is empty and (b) there is a link line presence.

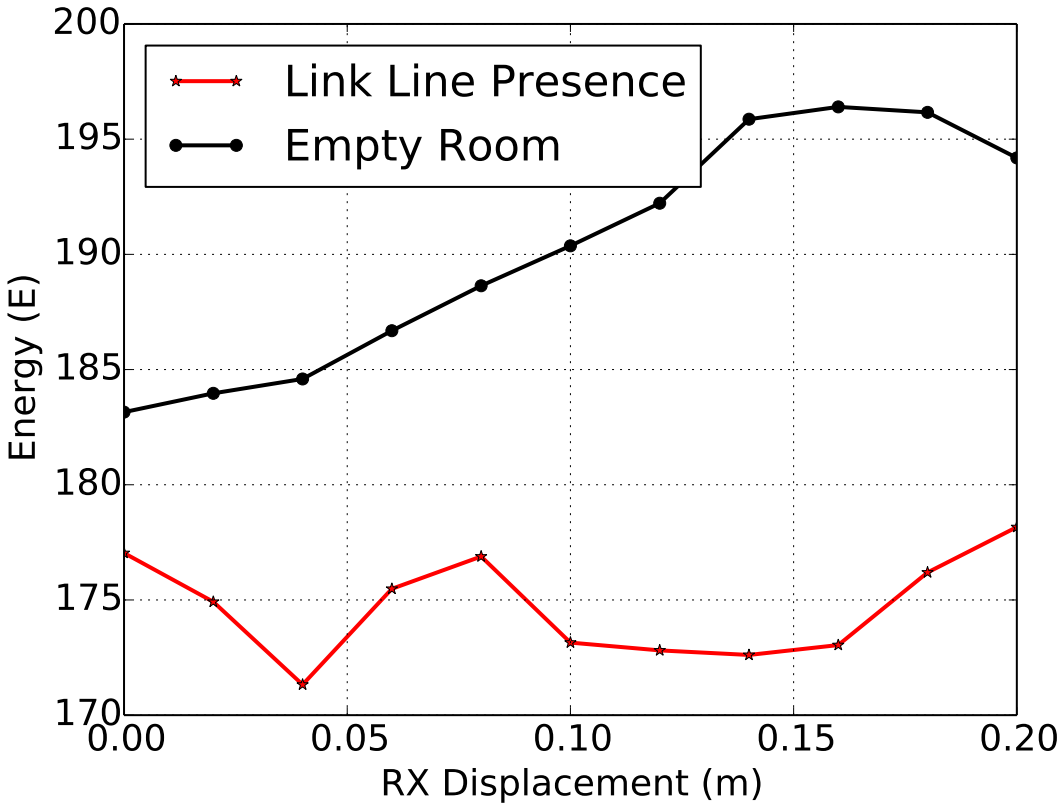

Figure 3.7. The energy E in the near-direct path as a function of receiver displacement for the empty-room case vs. link line presence.

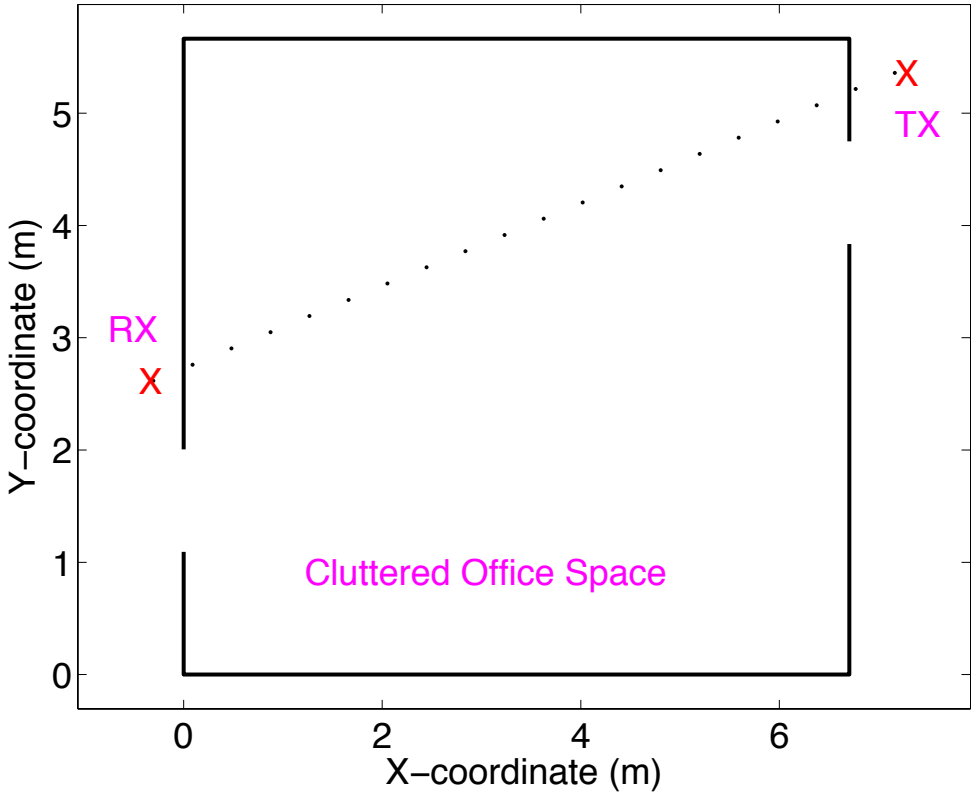

Figure 3.8. The floor plan of the office space used to perform link line crossing tests. The office space is full of office furniture, creating a cluttered environment.

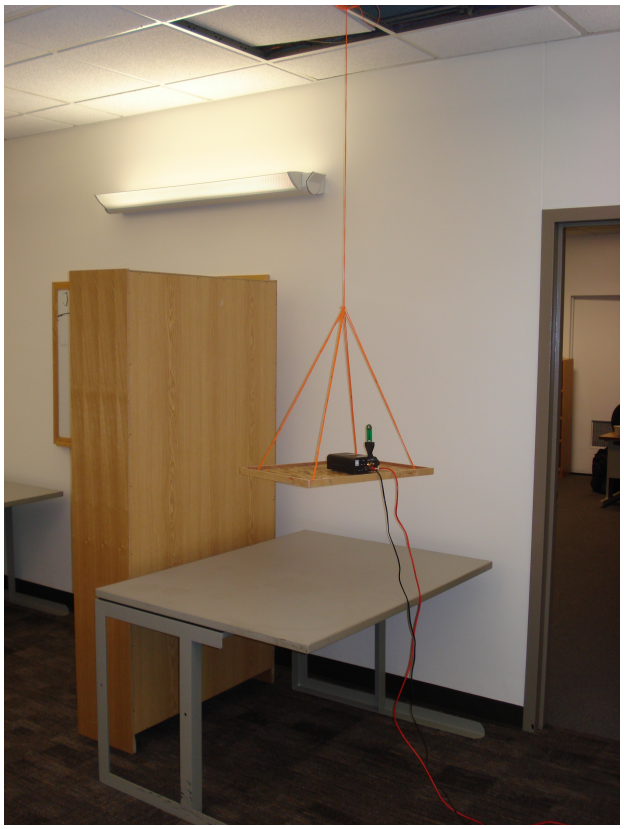

Figure 3.9. The receiver sits on a wooden platform which hangs from the ceiling. The platform is equipped to swing parallel to the wall through 0.20 m.

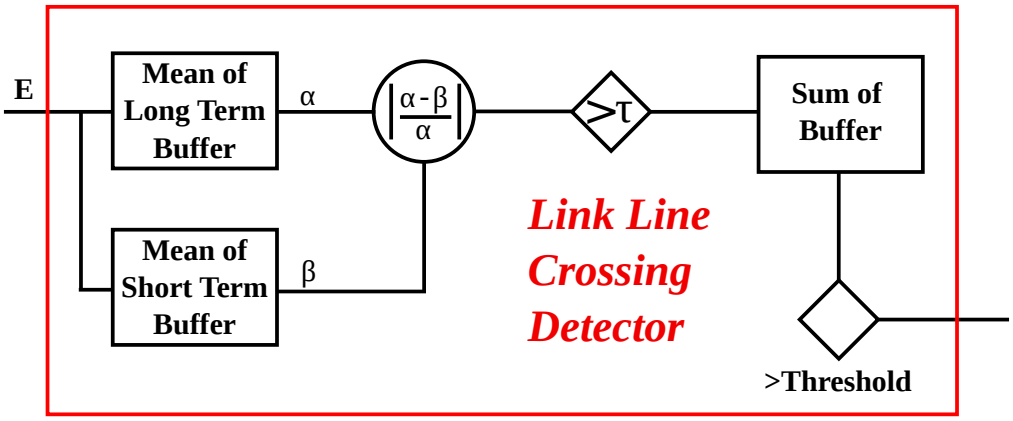

Figure 3.10. Moving average based detection [2]: Detector is 1 if the difference between short-term and long-term average exceeds τ multiple times during a time interval.

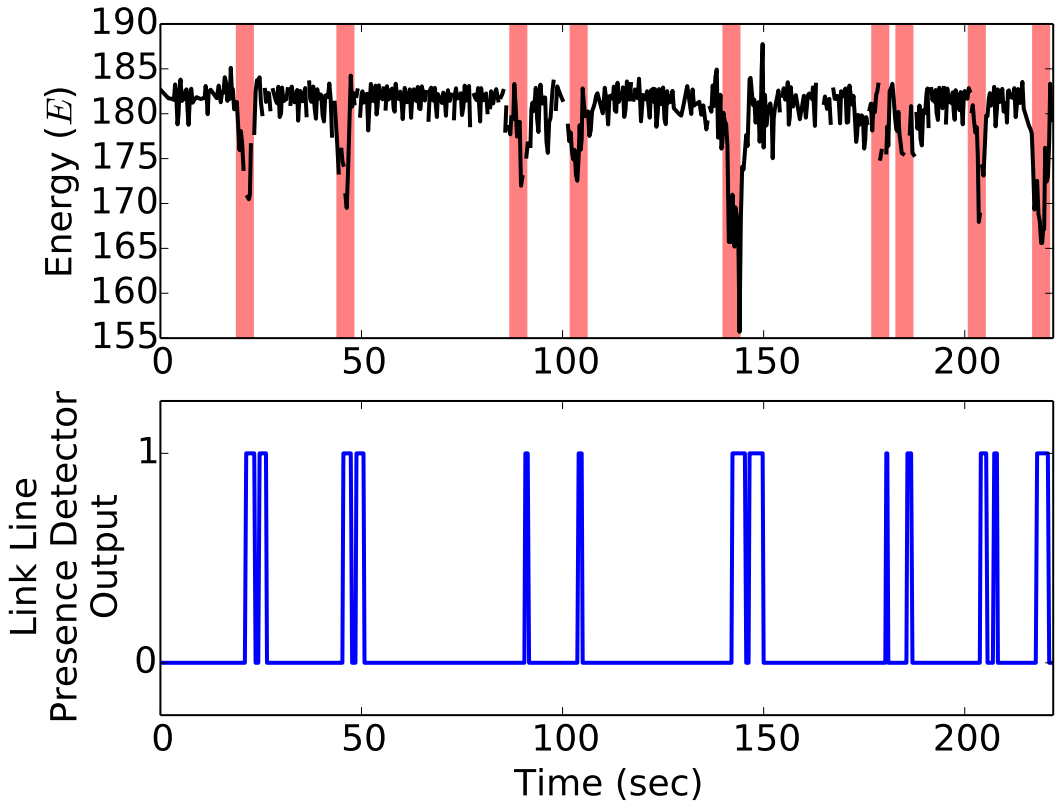

Figure 3.11. Measurements E over time with the output of the link line presence detector when the UWB receiver position is displaced up to 0.10 m.

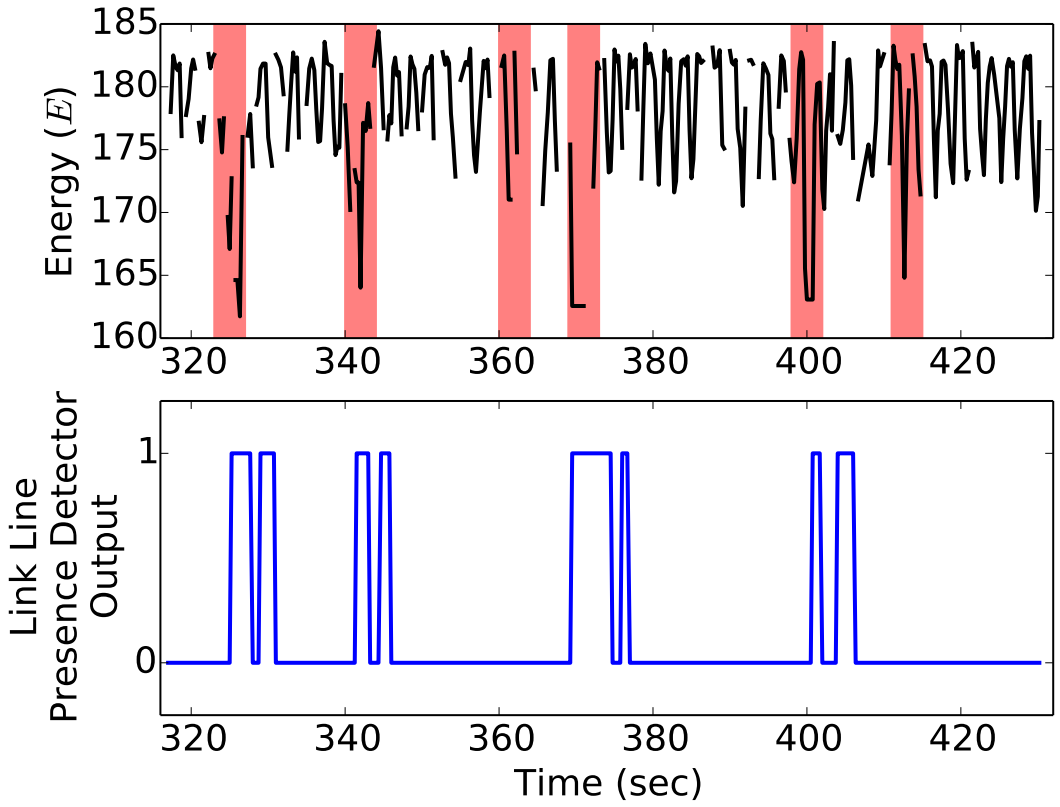

Figure 3.12. Measurements E over time with the output of the link line presence detector when the UWB receiver position is displaced up to 0.20 m.

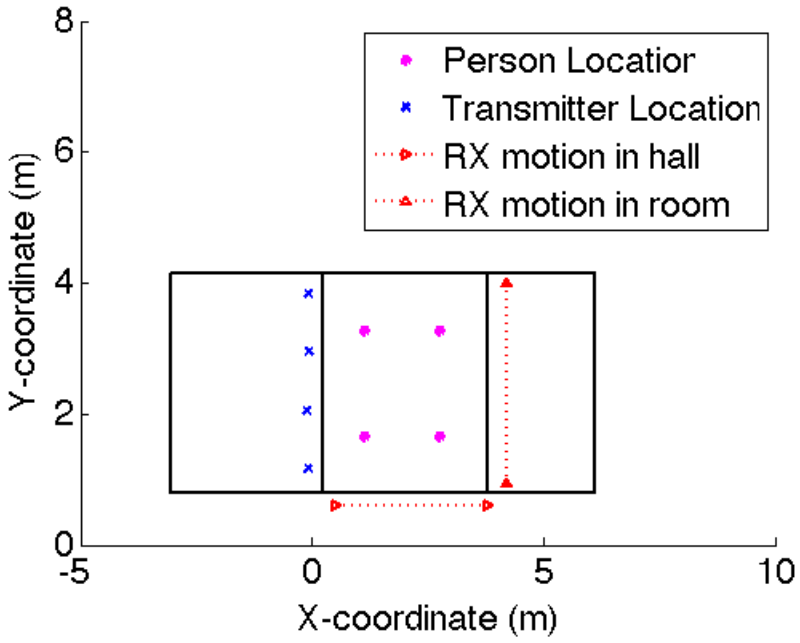

Figure 3.13. A room layout of the test site used to perform localization.

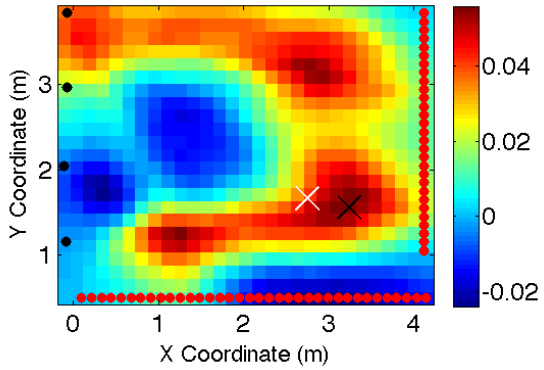

(a) 0.50 m error when the person stands at $j = 1$.

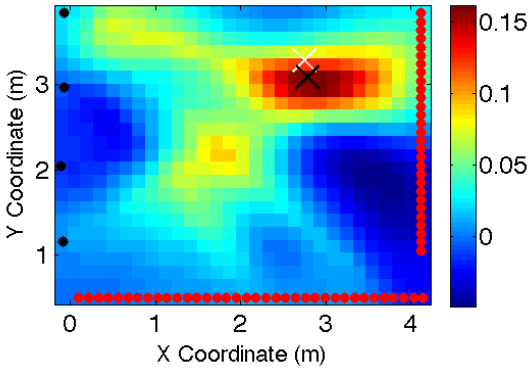

(b) 0.19 m error when the person stands at $j = 2$.

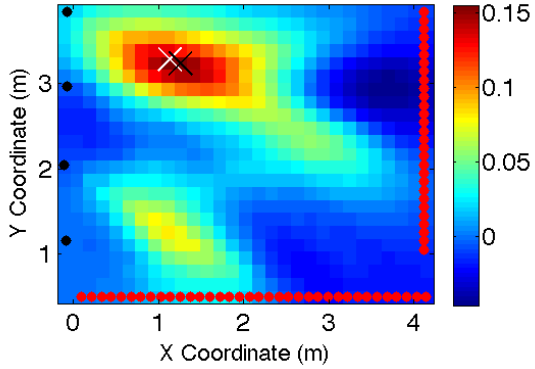

(c) 0.13 m error when the person stands at $j = 3$.

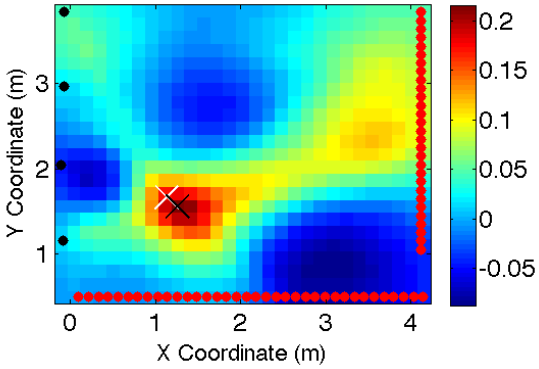

(d) 0.16 m error when the person stands at $j = 4$.

Figure 3.14. Images produced using RTI for the mobile transceiver experiment campaign. The black X's are the true coordinates and the white X's are the estimated coordinates. The black and red dots surrounding the image are the transmitter and reference receiver locations, respectively. Areas in the image with higher intensity suggest a greater ΔM for link lines that pass through that area of the network.

Table 3.1. Error in Person's Estimated and Actual Location

Standing Position	Error
1	0.50 m
2	0.19 m
3	0.13 m
4	0.16 m

3.8 References

[1] J. Wilson and N. Patwari, "Radio tomographic imaging with wireless networks," *IEEE Trans. Mobile Computing*, vol. 9, no. 5, pp. 621–632, May 2010, appeared online 8 January 2010.

[2] M. Youssef, M. Mah, and A. Agrawala, "Challenges: device-free passive localization for wireless environments," in *MobiCom '07: ACM Int'l Conf. Mobile Computing and Networking*, 2007, pp. 222–229.

[3] A. M. Haimovich, R. S. Blum, and L. J. Cimini, "MIMO radar with widely separated antennas," *IEEE Signal Process.*, vol. 25, no. 1, pp. 116–129, Jan. 2008.

[4] C. Chang and A. Sahai, "Object tracking in a 2D UWB sensor network," in *38th Asilomar Conf. on Signals, Sys. and Computers*, vol. 1, Nov. 2004, pp. 1252–1256.

[5] O. Kaltiokallio, M. Bocca, and N. Patwari, "A fade level-based spatial model for radio tomographic imaging," *IEEE Trans. on Mobile Computing*, vol. 13, no. 6, pp. 1159–1172, June 2014.

[6] D. Zhang, J. Ma, Q. Chen, and L. Ni, "An RF-based system for tracking transceiver-free objects," in *5th Annual IEEE Int. Conf. on Pervasive Computing and Commun., 2007. PerCom '07.*, March 2007, pp. 135–144.

[7] X. Chen, A. Edelstein, Y. Li, M. Coates, M. Rabbat, and A. Men, "Sequential monte carlo for simultaneous passive device-free tracking and sensor localization using received signal strength measurements," in *2011 10th Int. Conf. on Inform. Process. in Sensor Networks (IPSN)*, April 2011, pp. 342–353.

[8] J. Wilson and N. Patwari, "A fade level skew-Laplace signal strength model for device-free localization with wireless networks," *IEEE Trans. Mobile Computing*, appeared online 12 May 2011.

[9] Y. Zhao, N. Patwari, J. M. Phillips, and S. Venkatasubramanian, "Radio tomographic imaging and tracking of stationary and moving people via kernel distance," in *Proc. of the 12th Int. Conf. on Inform. Process. in sensor networks*. ACM, 2013, pp. 229–240.

[10] G. D. Durgin and T. S. Rappaport, "Theory of multipath shape factors for small-scale fading wireless channels," *IEEE Trans. Antennas and Propagation*, vol. 48, no. 5, pp. 682–693, April 2000.

[11] N. Patwari, G. D. Durgin, T. S. Rappaport, and R. J. Boyle, "Peer-to-peer low antenna outdoor radio wave propagation measurements at 1.8 GHz," in *IEEE Vehicular Technology Conf.*, vol. 1, May 1999, pp. 371–375.

[12] G. D. Durgin, V. Kukshya, and T. S. Rappaport, "Wideband measurements of angle and delay dispersion for outdoor and indoor peer-to-peer radio channels at 1920 MHz," *IEEE Trans. Antennas and Propagation*, vol. 51, no. 5, pp. 936–944, May 2003.

[13] J. C. Liberti and T. S. Rappaport, "A geometrically based model for line-of-sight multipath radio channels," in *IEEE 46th Vehicular Technology Conf.*, vol. 2, 1996, pp. 844–848.

[14] E. Paolini, A. Giorgetti, M. Chiani, R. Minutolo, and M. Montanari, "Localization capability of cooperative anti-intruder radar systems," *EURASIP J. on Advances in Signal Process.*, pp. 1–14, 2008, article ID 236791.

[15] D. Maas, M. Firooz, J. Zhang, N. Patwari, and S. Kasera, "Channel sounding for the masses: Low complexity gnu 802.11b channel impulse response estimation," *IEEE Trans. on Wireless Commun.*, vol. 11, no. 1, pp. 1 –8, January 2012.

[16] H. Hashemi, "The indoor radio propagation channel," *Proc. IEEE*, vol. 81, no. 7, pp. 943–968, July 1993.

[17] T. Domain, "PulsON©220 Reference Design: Implement and Prototype," http://www.timedomain.com/datasheets/P220aRD.php, 2013, [Online; accessed 10-March-2013].

[18] O. Kaltiokallio, M. Bocca, and N. Patwari, "Follow @grandma: Long-term device-free localization for residential monitoring," in *2012 IEEE 37th Conf. on Local Computer Networks Workshops (LCN Workshops)*, Oct 2012, pp. 991–998.

[19] ——, "Enhancing the accuracy of radio tomographic imaging using channel diversity," in *2012 IEEE 9th Int. Conf. on Mobile Adhoc and Sensor Sys. (MASS)*, Oct 2012, pp. 254–262.

[20] J. Wilson and N. Patwari, "See through walls: motion tracking using variance-based radio tomography networks," *IEEE Trans. Mobile Computing*, vol. 10, no. 5, pp. 612–621, May 2011, appeared online 23 September 2010.

[21] L. Reggiani, M. Rydström, G. Tiberi, E. G. Ström, and A. Monorchio, "Ultra-wide band sensor networks for tracking point scatterers or relays," in *6th Int. Symp. on Wireless Communication Sys. 2009 (ISWCS-09)*, Sept. 2009.

[22] M. Rydström, E. G. Ström, A. Svensson, and L. Reggiani, "An algorithm for positioning relays and point scatterers in wireless systems," *IEEE Signal Process. Lett.*, vol. 15, pp. 381–384, 2008.

[23] M. McCracken and N. Patwari, "Hidden markov estimation of bistatic range from cluttered ultra-wideband impulse responses," in *2012 IEEE Topical Conf. on Wireless Sensors and Sensor Networks (WiSNet)*, jan. 2012, pp. 17 –20.

[24] F. Viani, P. Rocca, M. Benedetti, G. Oliveri, and A. Massa, "Electromagnetic passive localization and tracking of moving targets in a WSN-infrastructured environment," *Inverse Problems*, vol. 26, pp. 1–15, March 2010.

[25] M. Seifeldin and M. Youssef, "Nuzzer: A large-scale device-free passive localization system for wireless environments," Arxiv.org, Tech. Rep. arXiv:0908.0893, Aug. 2009.

[26] M. Aftanas, "Through wall imaging with uwb radar system," Ph.D. dissertation, Technical University of Košice, Košice, Slovakia, 2009.

CHAPTER 4

YOU'RE CROSSING THE LINE: LOCALIZING BORDER CROSSINGS USING WIRELESS RF LINKS

4.1 Abstract

Detecting and localizing a person crossing a line segment, i.e., border, is valuable information in security systems and human context awareness. To that end, we propose a border crossing localization system that uses the changes in measured received signal strength (RSS) on links between transceivers deployed linearly along the border. Any single link has a low signal-to-noise ratio because its RSS also varies due to environmental change, (e.g., branches swaying in wind), and sometimes does not change significantly when a person crosses it. The redundant, overlapping nature of the links between many possible pairs of nodes in the network provides an opportunity to mitigate errors. We propose new classifiers to use the redundancy to estimate where a person crosses the border. Specifically, the solution of these classifiers indicates which pair of neighboring nodes the person crosses between. We demonstrate that in many cases, these classifiers provide more robust border crossing localization compared to a classifier that excludes these noisy, redundant measurements.

4.2 Introduction

Knowing when and where people leave one region and enter another is an important piece of information in an age of increasing security and human context-aware comput-

ing systems. A person illegally crossing a national border, a driver passing through an intersection, or a shopper entering an aisle in a store are examples of "border crossings," i.e., people moving from one region to another by crossing the line segment that separates them.

In this paper, we present methods for localizing a person crossing a border by measuring overlapping line segment crossings. A related idea is shown in movies like *Entrapment*, *Ocean's Twelve*, and *The Return of the Pink Panther*, in which a seemingly impossible-to-bypass mesh of laser beams serves as a security system, and blocking any one laser triggers an alarm. Instead of lasers, we propose using received signal strength (RSS) measurements from a radio frequency (RF) link to detect line segment crossings.As in [1]–[5], we conceptualize a radio link as a *link line*, i.e., the line segment between a transmitter and receiver. Compared to a laser beam, an RF link experiences changes in RSS in a relatively large area around the link line. With some RF links, that area around the link line is small. The RSS on these links experience large changes when a person is on the link line; but when a person is far away from the link line, the RSS shows very little change. However, other RF links can experience large changes even when a person is far away from the link line; moreover, the link can experience very little change even when the person is on the link line (see Figure 4.1). For our purposes it suffices to say that these "noisy" links have low signal and high noise and thus are less reliable as link line crossing detectors.

In this paper, we propose using multiple, overlapping links of varying signal-to-noise ratio (SNR) in methods that not only answer the question of when a border is crossed, but where the border is crossed. To accomplish these goals, we deploy N nodes linearly along a border such that links form between pairs of nodes (see Figure 4.2). Nodes k and l form a link (k,l). Each link has an associated line segment between the positions of nodes k and l, which we call the link line. We denote $\mathcal{L}$ as the set of all links $(k,l), k \neq l$, which are measured in the network. A special subset of $\mathcal{L}$ is what we call the set of "short segments", the links $(j, j+1)$ for $j = 1, \ldots, N-1$. Short segments have neighboring nodes as endpoints. As shorthand notation, we call the link line on $(j, j+1)$ "short segment j".

First, consider a network in which we measure RSS only on the short segments j, for $j = 1, \ldots, N-1$, and have as a goal to estimate which one of these, if any, were crossed by a person. Any single false alarm or missed detection among the $N-1$ links would cause

the system to be unable to determine the crossed short segment.

Next, consider a network in which we measure links (k, l) for many overlapping links $\mathcal{L}$. When a person crosses through a particular short segment j, they also must simultaneously cross some other longer link lines associated with links (k, l) for which $k \leq j < j + 1 \leq l$ (see Figure 4.3). In this paper, we propose that a system that exploits the measurements of the redundant links can be more robust to single link errors. We compare, via experimentation, the redundant links network to the short segment-only network in terms of classification accuracy.

With our goal of analyzing the robustness of both systems, we compare the accuracy of three crossing segment classifiers we propose in this paper. The closest codeword classifier (CCC) and the maximum a posteriori classifier (MAPC) leverage the measurements of the redundant link; the simple classifier (SC), excludes these measurements. Although our focus is on the performance of these classifiers, we must evaluate them by implementing link line crossing detectors (LLCD) [1]–[5]. Algorithms in a LLCD use link RSS measurements to produce link line crossing measurements x_i for each link $i \in \mathcal{L}$. The output x_i is a binary 1 when a crossing is detected and 0 otherwise. A vector $\mathbf{x} = [x_1, \ldots, x_L]^T$ from $L = |\mathcal{L}|$ links is then fed into a crossing segment classifier (see Figure 4.4). In our paper, a LLCD outputs one value for x_i for RSS measurements collected during time interval T_{max}, where r_i is an RSS measurement for link i.

We discuss the details of each classifier in Section 2, compare classifier accuracies through two experiments in Section 3, discuss the results, and conclude.

4.3 Methods

In this section, we propose two crossing segment classifiers that use the noisy, redundant binary measurement vector $\mathbf{x}$ to classify which short segment j a person crossed while passing over a border, or if no crossing took place. In addition, we describe a third simple classification method that excludes the measurements from the redundant links in its decision. We first describe a LLCD that feeds binary vector measurements into the classifiers.

4.3.1 Detecting Link Line Crossings

In order to evaluate our classifiers, we first implement a LLCD. Although any LLCD could be used, we choose to implement the moving average based detection method from Section 4.3.1 in [2] because of its straightforward implementation and its accuracy in detecting link line crossings. In this method, RSS measurements made on a link i feed into a LLCD as shown in Figure 4.5. The moving average based detector adds RSS measurements to a short and long term buffer. The long term buffer stores the static behavior of the link while the short term buffer stores the current behavior. Upon adding a new RSS measurement to the buffers, the detector computes the relative difference between the means of the two buffers. When the relative difference exceeds a threshold τ, an event is detected. These events are stored in a buffer that holds T_{max} amount of samples. When full, the buffer is summed to count the number of events that occurred during T_{max}. If the number of events exceeds another threshold, then $x_i = 1$. The buffer is then cleared to receive the next T_{max} events. A LLCD is created for each link, and we store the binary measurements in $\mathbf{x}$.

If the LLCDs measured link line crossings without error, then a person crossing a particular short segment of the border would result in a unique $\mathbf{x}$. We call these unique binary measurement vectors *codewords* where the codeword for a person crossing short segment j is $\mathbf{w}(j) = [w_1(j), w_2(j), \ldots, w_L(j)]^T$ where $w_i(j) = 1$ if by crossing j, the person also crosses link i, and 0 otherwise. Formally,

$$w_i(j) = \begin{cases} 1, & \text{if } (l_i \leq j) \text{ and } (j+1 \leq k_i) \\ 0, & \text{otherwise} \end{cases} \tag{4.1}$$

where k_i and l_i are the endpoints of link i, and $k_i < l_i$, without loss of generality. We denote the "off" codeword $\mathbf{w}(0)$ whose elements are all 0. We define short segment 0 as the class that no person crossed the border. As a result, an N node system will have N unique codewords, which we denote as set $\mathcal{W} = \{\mathbf{w}(j)\}_{j=0}^{N-1}$.

4.3.2 Closest Codeword Classifier

The first classifier we propose, the CCC, finds the codeword that is closest to $\mathbf{x}$ in terms of Hamming distance. The CCC classifies which short segment j is crossed using

$$\widehat{j} = \arg\min_{j} \|\mathbf{x} - \mathbf{w}(j)\|^2 \tag{4.2}$$

where $\|\cdot\|^2$ is the ℓ_2 norm. Note that if there are no errors in any of the L link line crossing detectors, then $\mathbf{x} = \mathbf{w}(j)$ for the correct short segment j which was crossed. If $\widehat{j} = 0$ then the CCC classifies that there was no crossing.

In some instances, more than one codeword will minimize (4.2), thus the CCC does not definitively classify which of the short line segments were crossed. Under these conditions, the CCC randomly chooses one of the short line segments whose codeword satisfies (4.2). Finding the closest match between $\mathbf{x}$ and $\mathbf{w}(j)$ can be viewed as error correction where $\mathbf{x}$ differs from the true codeword $\mathbf{w}(j)$ in γ places. The CCC corrects γ errors when the detector chooses the correct crossed segment.

4.3.3 Maximum a Posteriori Classifier

Here, we propose the MAPC, which builds upon the CCC by adding in prior knowledge of the accuracy of each LLCD. We capture the accuracy of the detector for link i by its probability of detection, P_i^d, and its probability of false alarm, P_i^{fa}. These probabilities help us make more informed decisions about which short line segment a person crossed based on $\mathbf{x}$.

To learn the prior probabilities, as a proof of concept, we assume that the network is trained by a person crossing each short segment multiple times. The value of P_i^d and P_i^{fa} are then estimated from the training data. To prevent the MAPC from assuming any particular measurement provides certainty, we limit P_i^d and P_i^{fa} to be in the range $\epsilon < P_i^d, P_i^{fa} < 1 - \epsilon$ for some small $\epsilon > 0$. In our experiments, we use $\epsilon = 0.0001$. Future work could explore methods to predict performance via statistics that can be measured without training, e.g., RSS mean or variance.

To formulate the MAPC, we first formulate the likelihood of measurement $\mathbf{x}$ given that a person crossed short segment j. Under the assumption of conditional independence of links, this is $p(\mathbf{x} \mid j) = \prod_{i=1}^{L} p(x_i \mid j)$, where

$$p(x_i \mid j) = \left[(P_i^d)^{x_i}(1 - P_i^d)^{1-x_i}\right]^{w_i(j)} \cdot \left[(P_i^{fa})^{x_i}(1 - P_i^{fa})^{1-x_i}\right]^{1-w_i(j)}. \tag{4.3}$$

Next we consider the prior probabilities of j. If the N nodes are equally spaced along the border, this might make crossing each short segment j equally probable. If, however, N nodes are unevenly distributed along the border, we may want to assume that crossing a longer short segment is more probable than crossing a shorter short segment. We may also

want to modify how likely crossing j is given environmental factors, e.g. thick vegetation, hills, etc. To account for these conditions, we impose a prior, $p_J(j)$, on each j. With a prior on j, we form the more general MAPC, formally defined as

$$\widehat{j} = \arg\max_{j} p_J(j)\, p(\mathbf{x} \mid j). \tag{4.4}$$

Note again that if multiple j have equal joint probability, we randomly choose one of them.

4.3.4 Simple Classifier

A more basic method to classify which short segment was crossed would be to eliminate all the redundant links and measure only the short segments. The third classifier, i.e. SC, in contrast to the CCC and MAPC, only measures link line crossings on $(j, j+1)$ for $j = 1, \ldots, N-1$. If a LLCD for short link i measures a 1 for x_i, then the system would classify short segment i was crossed. In the event that more than one LLCD outputs a 1, SC randomly selects from the candidate short segments for its solution. In like manner, if none of the LLCDs for the short link lines report a crossing, then SC selects the 0 class, for no crossing, as its solution. We show in the next section how each classifier compares in accuracy.

4.4 Experimental Verification

In this section we show the accuracy of the CCC and MAPC compared to the SC using two experimental campaigns.

4.4.1 Equipment and Procedures

The wireless nodes used in the following experiments are Texas Instruments CC2531 USB dongles, each of which transmits at 2.4 GHz with +4.5 dBm. Following a TDMA protocol, each node takes a turn transmitting a packet while the others receive the packet. An additional listen node is connected to a laptop to overhear the wireless traffic and to log RSS measurements for each link. Each node is placed on a tripod that stands 0.91 meters high.

Two experimental sites are chosen to show the accuracy of each classifier in different environments. The first site is in a natural area with many trees. Nine nodes are deployed such that they are 4 meters apart (see Figure 4.6). The second site is inside the Union cafe-

teria at the University of Utah by lunch tables and large pillars. The indoor environment induces more complex fading patterns and is similar to indoor border crossing scenarios (e.g. the aisles of a store). Nine nodes are again equally spaced along the 29.26-meter border (see Figure 4.7).

To test with fewer than nine nodes, we keep the deployment along the same total border length, and four nodes are removed such that five evenly spaced nodes remain. Next, two of the remaining five nodes are removed, leaving three evenly spaced nodes. Under these conditions, the data from the nine node configuration can be used for the five and three node case by removing the appropriate links' RSS measurements.

In each experiment, a border crosser indicates into a voice recorder the start of the experiment. RSS values for all of the links are then logged in a computer as the person crosses the border. The border crosser then indicates into the voice recorder the end of the T_{max}-long crossing experiment and the computer stops logging the RSS values. This process is repeated thirty times for each short segment j, for $j = 1, \ldots, N-1$. In addition to crossing each short segment, the border crosser then walks back and forth 2.4 meters away from and parallel to the border, so that we can evaluate what happens when a person walks near but never crosses the border. The above procedures are carried out twice, first for a training data set, and second for a testing data set.

In this paper, the LLCDs use the same best parameters recorded for the long term and short term buffers in the last of Section 3.4.1 of [2] in both the indoor and outdoor experiments. However, we vary the threshold τ to achieve varying levels of detection and false alarm accuracy for the LLCDs. We compare the accuracy of the classifiers using the following metrics: the probability of correct classification (P_{cc}), meaning $\widehat{j}$ matches the true short segment crossed; and the probability of border crossing false alarm (P_{fb}), meaning $\widehat{j} \neq 0$ when the border was not crossed. We envision that a border crossing localization system should have a low P_{fb} (at the expense of a lower P_{cc}) in some applications, because a false alarm could result in wasted time and resources devoted to investigate a falsely reported border crossing.

4.4.2 Experiment 1 (Outdoor) Results

In this section, we compare the probability of P_{cc} and P_{fb} as a function of τ using the MAPC, CCC, and SC in the outdoor environment experiment. We show the relationship between τ and these probabilities in Figure 4.8 and 4.9 where five nodes were deployed. Figure 4.8 shows that as τ approaches 0, P_{fb} increases. A low τ causes an LLCD to frequently output a binary 1 even when the person does not cross the link. When many of the LLCDs output a one, the classifiers tend to decide that multiple short segments were crossed. Thus, even when the border is not crossed, the classifiers yield a high false alarm classification probability. Moreover, when the border is crossed, the classifier must randomly choose between the classified crossed segments, thus lowering P_{cc} (see Figure 4.9).

In contrast, when τ is large, few, if any, link lines will be detected as crossed. When many of the LLCDs output a zero, the classifiers tend to decide that no short segments were crossed, i.e. $\widehat{j} = 0$. This reduces P_{fb}, but we also observe a decrease in P_{cc} since we are unlikely to classify the correct crossed short segment.

For the remainder of this paper, we let τ be the value that maximizes P_{cc} while keeping $P_{fb} \leq 0.01$ for each classifier. In Figure 4.10, we show P_{cc} for each classifier when three, five, and nine nodes are deployed.

Both the MAPC and the CCC improve in P_{cc} as the number of nodes increases, achieving almost perfect classification for $N = 5$ and 9. Adding more nodes to the system creates greater distance between codewords and $\mathbf{x}$ and therefore allows us to make more correct classifications. We also observe that the MAPC outperforms the CCC for $N = 3$. By adding in probabilistic conditions in the MAPC, we improve the accuracy compared to the CCC, which does not take into account these probabilities. When we compare the SC to the MAPC and CCC, we observe that the SC achieves a comparable P_{cc} to the MAPC for $N = 3$ and 5, but suffers when $N = 9$. So whereas MAPC and CCC strictly increase in P_{cc} with more nodes, the SC can perform worse. The SC relies on the short link lines for classification, and when one or more short link lines are poor line segment crossing detectors, the SC can suffer in accuracy.

4.4.3 Experiment 2 (Indoor) Results

In this section, we again compare P_{cc} of the three classifiers by using the τ that maximizes P_{cc} while keeping $P_{fb} \leq 0.01$ (see Figure 4.11). We observe dramatically reduced P_{cc} for almost all node configurations and classifiers compared to the outdoor case. One explanation for this reduction is that an indoor setting introduces more multipath fading than an outdoor environment, which in turn causes more links to be poor line segment crossing detectors.

In spite of the significant drop in P_{cc}, we observe the same general improvement in classification as N increases for the MAPC and CCC. We also observe that the SC shares this same improving behavior, which we did not observe in the outdoor case. It is probable that all short link lines were sufficiently reliable line segment crossing detectors in this setting and SC improved as a result with increasing N.

A surprising result is that the CCC and SC perform twice as well as the MAPC when $N = 5$. The MAPC uses probabilities estimated from training data, and we would therefore anticipate that the MAPC would always perform at least as well as the CCC and SC. However, the probability estimates may be inaccurate. The inaccuracies are influenced by the places a person walks with relation to the border during training. Ideally, we would want a person to train the MAPC by visiting several locations near and on the border and then record the link accuracies. But this would take a significant amount of time to train. When the estimates are close to the true probability, the performance gain of the MAPC can be as great as two times, as in the $N = 9$ case.

In a practical outdoor border crossing localization system, we might conclude that using the CCD would be a ideal choice since it achieves a high accuracy and does not need to be trained. However, if the number of nodes were limited, the SC may be the better choice for its accuracy and plug-and-play nature. However, in the more complicated indoor environment, the MAPC would achieve a higher P_{cc} using a large number of nodes. Although the MAPC must be trained, this may only have to be done occasionally.

4.5 Conclusion

In this paper, we proposed two new classifiers that provide robust border crossing localization using RSS measurements on redundant RF links. Each classifier localized a

border crossing by deciding which short segment was crossed. The CCC obtained near perfect classification at a 0.01 false alarm rate in the outdoor border for five and nine nodes and did not have to be trained. The MAPC matched or exceeded the CCC in accuracy but required a training period. The SC achieved the highest accuracy with three nodes, but can degrade as the number of nodes increases. In the indoor environment, however, nine nodes were required for any classifier to reach adequate accuracy; the MAPC reached a 0.86 probability of correct classification while the SC reached 0.72. The CCC was not a reliable classifier in this environment in any of the node configurations. Future experiments will test performance in other environments and with higher numbers of nodes.

We found that the number of nodes and the border environment were critical components in determining which of these three classifiers would be best. We found that leveraging redundancy improved accuracy when the number of nodes was high. However, when fewer nodes were deployed and thus little redundancy was present, methods that exploit redundancy performed as well or worse than a method that excluded redundant measurements. For an indoor border localization system, none of the classifiers worked well when three and five nodes were deployed. However, when we used nine nodes, using the redundant measurements provided more robustness despite noisy links.

In summary, we have demonstrated that when many nodes are employed in either indoor or outdoor environments, it is in our best interest to use a classifier that leverages redundancy.

4.6 Acknowledgements

This material is based upon work supported by the National Science Foundation under Grant Nos. #1407949 and #1035565.

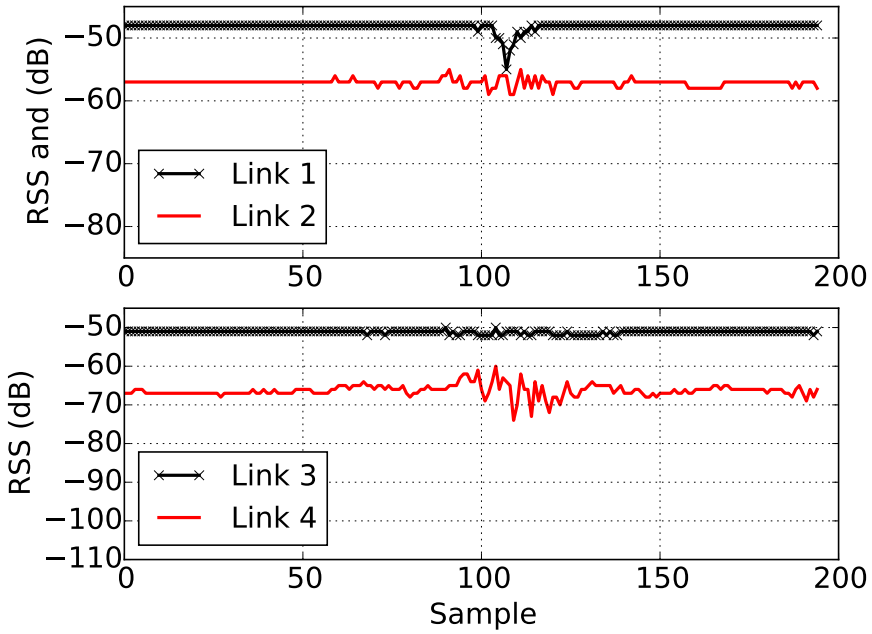

Figure 4.1. (top) The drop in Link 1 RSS at sample 108 correctly indicates that a person is crossing the link line. Link 2 sees small RSS changes and fails to detect the crossing. (bottom) No person is near the link line. Link 3 shows little change, but link 4 shows a significant drop in RSS at sample 108, which would incorrectly be detected as a crossing.

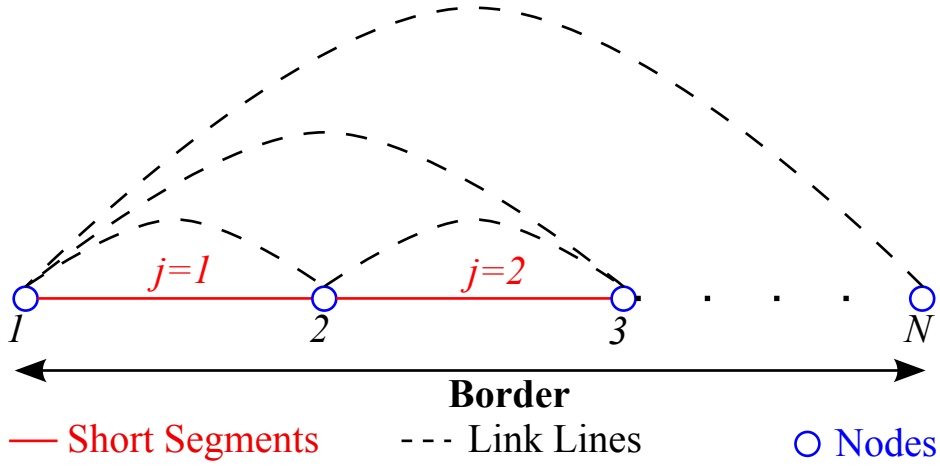

Figure 4.2. Border crossing system with N nodes aligned linearly. Short segments are created between neighboring pairs of nodes. Link lines are curved in this figure for visual purposes only. In practice, the link lines are viewed as line segments with the nodes as their endpoints.

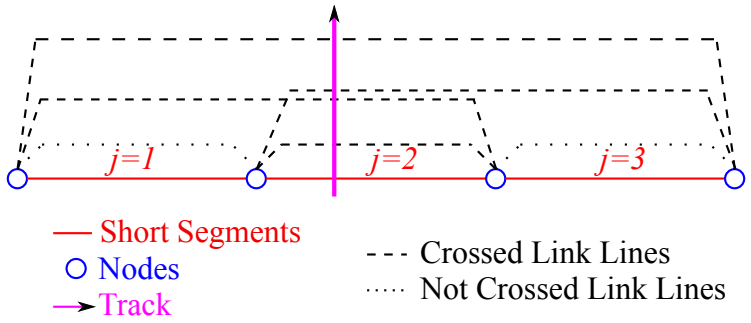

Figure 4.3. A certain set of links are crossed when a person passes over short segment s_2.

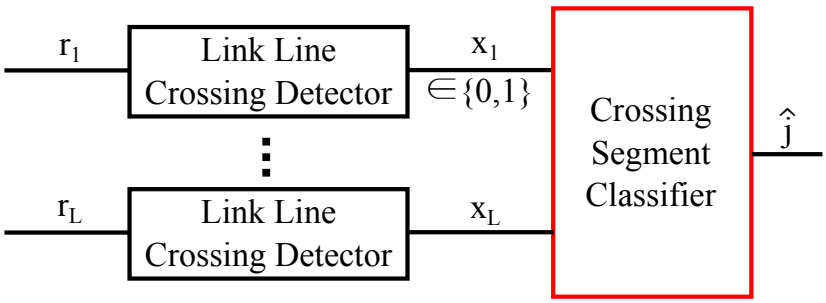

Figure 4.4. Block diagram of a border crossing localization system.

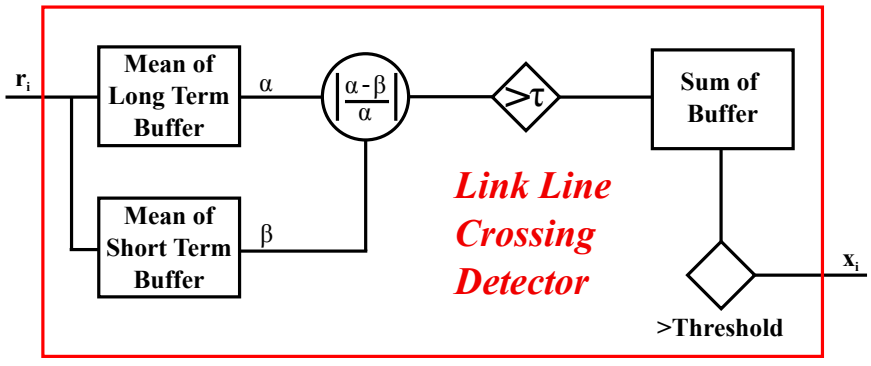

Figure 4.5. Moving average based detection [2]: Detector is 1 if the difference between short-term and long-term average exceeds τ multiple times during a time interval.

Figure 4.6. Experiment in outdoor environment.

Figure 4.7. Experiment near cafeteria tables.

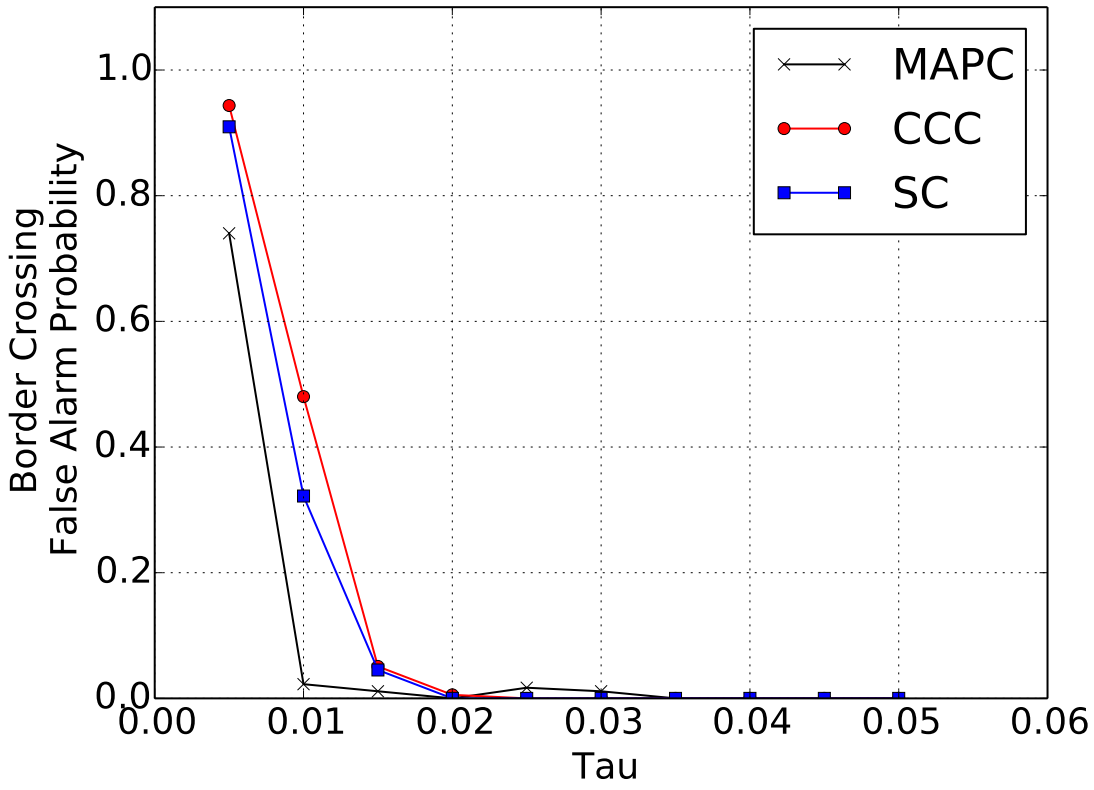

Figure 4.8. Probability of border crossing false alarm as a function of τ for $N = 5$.

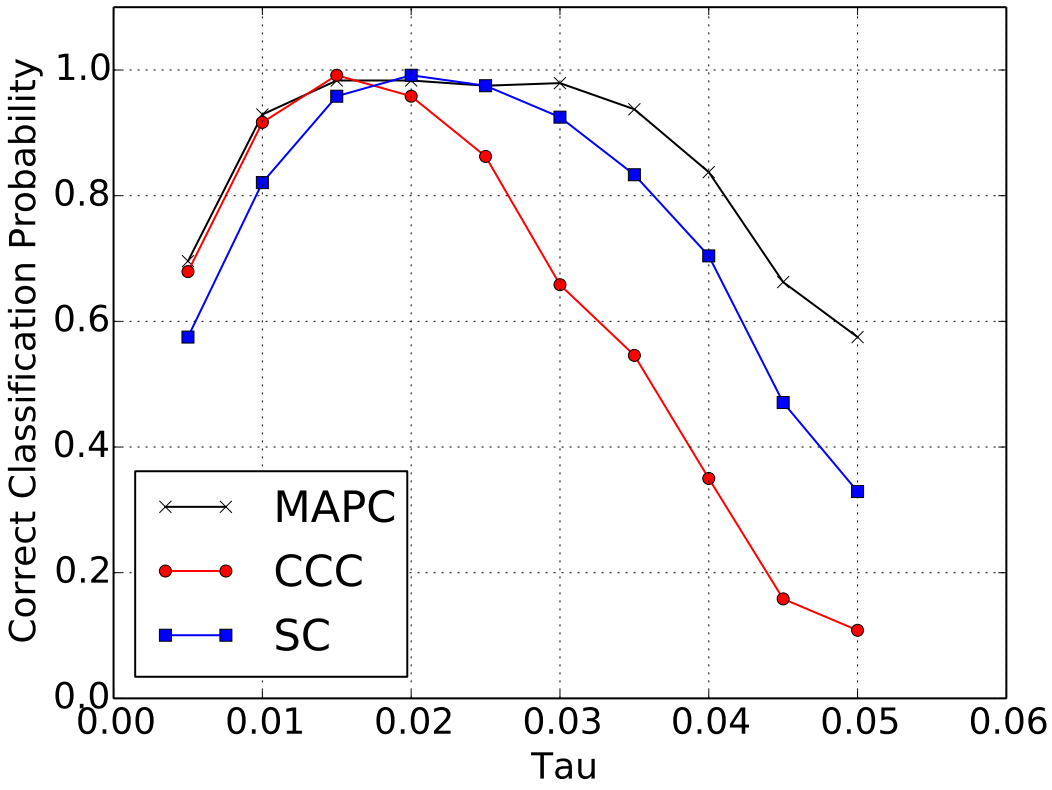

Figure 4.9. Probability of correct classification as a function of τ for $N = 5$.

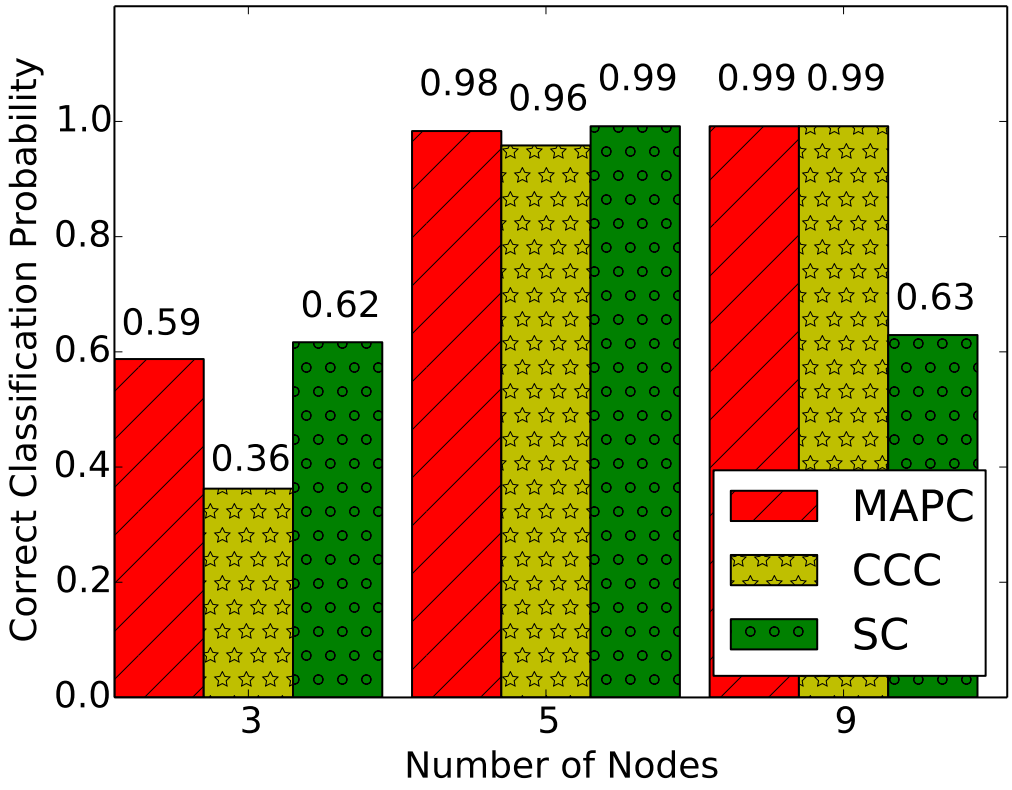

Figure 4.10. Probability of correct classification in the outdoor environment using the MAPC, CCC, and SC with a 0.01 probability of border crossing false alarm.

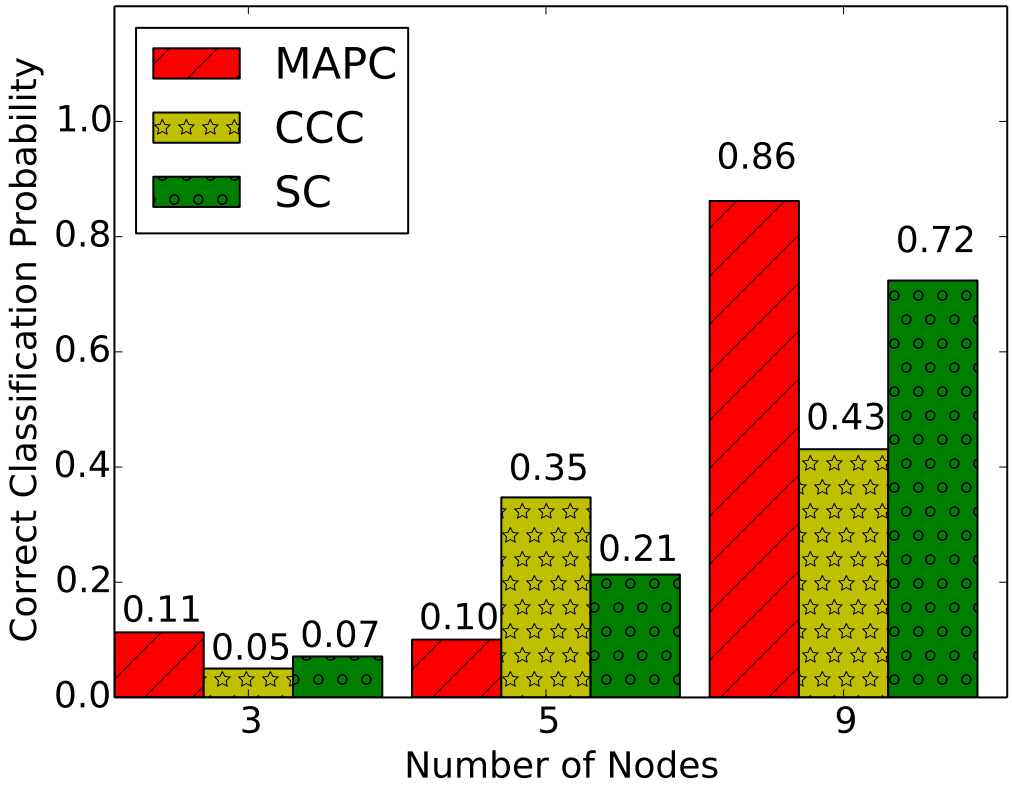

Figure 4.11. Probability of correct classification in the indoor environment using the MAPC, CCC, and SC with a 0.01 probability of border crossing false alarm.

4.7 References

[1] Ossi Kaltiokallio and Maurizio Bocca, "Real-time intrusion detection and tracking in indoor environment through distributed rssi processing," in *2011 IEEE 17th Int. Conf. Embedded and Real-Time Computing Sys. and Applications (RTCSA)*, Aug. 2011, vol. 1, pp. 61 –70.

[2] Moustafa Youssef, Matthew Mah, and Ashok Agrawala, "Challenges: device-free passive localization for wireless environments," in *MobiCom '07: ACM Int. Conf. Mobile Computing and Networking*, 2007, pp. 222–229.

[3] Yang Zhao, Neal Patwari, Jeff M. Phillips, and Suresh Venkatasubramanian, "Radio tomographic imaging and tracking of stationary and moving people via kernel distance," in *Proc. of the 12th Int. Conf. on Inform. Process. in Sensor Networks*, New York, NY, USA, 2013, IPSN '13, pp. 229–240, ACM.

[4] J. Wilson and N. Patwari, "A fade-level skew-laplace signal strength model for device-free localization with wireless networks," *IEEE Trans. on Mobile Computing*, vol. 11, no. 6, pp. 947–958, 2012.

[5] Yi Zheng and Aidong Men, "Through-wall tracking with radio tomography networks using foreground detection," in *2012 IEEE Wireless Commun. and Networking Conf. (WCNC)*. IEEE, 2012, pp. 3278–3283.

CHAPTER 5

HIGHLY RELIABLE SIGNAL STRENGTH-BASED BOUNDARY CROSSING LOCALIZATION IN OUTDOOR TIME-VARYING ENVIRONMENTS

5.1 Abstract

Detecting and locating outdoor boundary crossing events is valuable information in curbing drug trafficking, reducing poaching, and protecting high-asset equipment and goods. However, boundary sensing is notoriously challenging, prone to false alarms and missed detections, with serious consequences. Weather events, like rain and wind, make it even more challenging to maintain a low level of missed detections and false alarms. In this paper, we propose and test an automated system of wireless sensors which uses received signal strength (RSS) measurements to localize where a boundary crossing occurs. In addition, we develop new RSS-based statistical models and methods that can quickly be initialized and updated on-line by using link RSS statistics to adapt to time-varying RSS changes due to weather events. These models are implemented in two new classifiers that localize boundary crossings with few missed detections and false alarms. We validate our proposed methods by implementing one of the classifiers in a three month long deployment of a solar-powered, real-time system that captures images of the boundary for ground truth validation. Furthermore, over 75 hours of RSS measurements are collected

with an emphasis on collection during weather events, like rain and wind, during which we expect our classifiers to perform the worst. We demonstrate that the proposed classifiers outperform four other baseline classifiers in terms of false alarm probability by 1 to 4 orders of magnitude, and in terms of the misclassification probability by 1 to 2 orders of magnitude.

5.2 Introduction

In many situations, it is important to know when a person or other object crosses over a border or boundary in an outdoor environment. Wildlife preservation agencies wish to know when poachers have illegally crossed into a preservation area; national agencies wish to curb drug trafficking across national borders; farmers want to prevent loss of crop to thieves [1]. In many cases, the economic cost is too high to hire personnel to patrol the boundary of interest. In this paper, we propose and test an automated system of wireless sensors that detects and localizes when and where a boundary crossing occurs.

The idea of detecting and locating a tag-free person in sensor networks has already been developed and tested using several device-free localization (DFL) technologies. Using radio frequency (RF) links as the sensing method has been increasingly studied because of the ability to sense through walls and other objects opaque to light. Radio tomographic imaging [2], for example, measures received signal strength (RSS) on many wireless RF links and can achieve sub-meter localization errors in indoor environments. In this paper, we develop new DFL methods that are built specifically for the outdoor border crossing localization problem and we show that our methods can outperform current DFL methods.

One of the features of a boundary is that it is typically made up of a series of piecewise linear sections that divide two regions. A natural way of covering the boundary is to match the sensing system's geometry with that of the boundary: straight line segments. To this end, we build on the concept of using a wireless RF link as a line segment sensor [3], [4] where, if a person crosses the imaginary line segment between a transmitter and receiver, i.e. "link line," an algorithm can detect the crossing based on changes in the RSS measurements of the wireless channel.

Border sensing is notoriously challenging since sensors are prone to false alarms and missed detections, which have serious consequences [5]. In this paper, we propose to

deploy wireless nodes linearly along a boundary, partitioning the boundary into multiple short segments between neighboring nodes. The mesh network the nodes form creates many overlapping RF links. Limited in accuracy by themselves, the RF links, when overlapped in this deployment geometry, provide redundancy to improve crossing detection reliability and better localize which partition of the boundary is crossed [6].

We develop two new classifiers which use noisy RSS data from RF links in the network to determine the state of the boundary, either vacant or being crossed, and if being crossed, between which two nodes. This work contributes in several ways to the state-of-the-art:

- The new classifiers use soft decisions on each link, rather than hard decisions [6], and we show these allow significantly improved performance.

- Our classifiers do not use any labelled training. Rather, we develop simple statistical models whose parameters are estimated from a 5 second calibration period when it is known that the boundary is not being crossed. These parameters are re-estimated periodically during operation to adjust for time-varying changes in RSS measurements like those caused by weather events [7]–[9].

- We build and test a system running one of the classifiers in real-time for a three month outdoor deployment. We also recorded and make available over 77 hours of RSS data from the network [10], predominantly during weather events like rainstorms and wind when we anticipated the boundary monitoring would perform the worst.

- We use the data to compare the proposed classifiers with four baseline classifiers and show that the proposed classifiers can reduce the false alarm rate by 1 to 4 orders of magnitude or the misclassification rate by 1 to 2 orders of magnitude.

The remainder of this paper is organized as follows. Section 5.3 describes the overall boundary crossing localization system, the two proposed classifiers, and the adaptive RSS models we develop. Section 5.4 outlines the equipment used, the data collection experiments performed, and the validation metrics used to evaluate the proposed classifiers. Section 5.5 reports the results of the experiments. We describe related research in Section 5.6 and conclude the paper in Section 5.5.

5.3 Methods

5.3.1 Boundary Crossing Localization System

In our border crossing localization system, N nodes are deployed linearly along a border (see Figure 5.1). The nodes provide a natural series of line segments between neighbouring nodes that partition the boundary. We call the line segment between node j and $j+1$ "short segment j." The system we propose performs boundary crossing localization by classifying which short segment j a person is crossing. At any given time, our system outputs $\hat{j}$ where $\hat{j} \in \{0, 1, \ldots, N-1\}$. When $\hat{j} = 0$, our system indicates that no one is crossing the boundary at any location. In this wireless network, RF links form between each pair of nodes. For each of these links, the RSS, also called the received power in decibel units, is measured as r_i for wireless link i. The RSS is typically a discrete-valued measurement, and we denote its possible values as $\mathcal{S}$. We note that $\mathcal{S}$ also includes $\oslash$, the event that there was a missed packet and as such RSS was not measured. We observe a vector $\mathbf{r} = [r_1, r_2, \ldots, r_L]$ on L links.

Our boundary crossing localization system also consists of a model parameter update module and a crossing segment classifier (see Figure 5.2). The vector $\mathbf{r}$ is passed to the crossing segment classifier where we classify which section of the boundary the person crossed. The vector $\mathbf{r}$ is also passed to the model parameter update module where a buffer of recent RSS samplesIn an outdoor environment, we cannot count on the measurement statistics to stay the same over time. To address this reality, measurement statistics are periodically passed to the crossing segment classifier to update the models to account for time-varying changes in the RF channels. Later sections give further explanations of the update module and classifier.

5.3.2 Link Line Obstruction Model

In our proposed crossing segment classifiers, RSS measurements are used as evidence of a person being on or off of the link lines in the wireless network. Several statistical models currently exist that map RSS values or changes in RSS to probabilities of a person being on or off a link line [11]–[13]. The models in [11], [13], built using indoor measurements, can be used if the node locations are known. The model in [12] is independent of node locations, but there are eight tunable parameters. The models that we develop, which

have three tunable parameters and are independent of node locations, are initialized and updated by using the statistics of the RSS measurements. Our models allow us to quickly and easily adapt to time-varying outdoor environments caused by rain and humidity [9], wind [7], and temperature [8].

Our model is based on the probability distribution of RSS measurements when a person moves along any point of the link line, and when a person moves somewhere away from the link line. We conduct a short experiment to demonstrate the differences in the distributions for these two cases. A person first walks along a link line, back and forth between the two nodes, for several seconds. The person then walks 6 ft away from and parallel to the link line for several seconds. We show the histograms of a link's RSS in Figure 5.3. We observe that when a person is off the link line, the RSS measurements tend to have very little variance. When no objects move near the link line, multipath are not likely to change, and thus, RSS remain relatively constant. However, when a person is on the link line, we observe large variations in RSS. The distribution has a larger variance and the mean value has shifted.

We use these observations to model the on and off link line distribution of RSS in dB as Gaussian, but modified to account for missed packets $r_i = \oslash$ and for numerical stability. We define the "off link line" probability mass function (pmf) for link i as,

$$f(r_i \mid \text{Off}) = \begin{cases} \rho, & r_i = \oslash \\ \frac{1}{\gamma} \max\left\{\epsilon, \mathcal{N}(r_i; \nu_i, \sigma_i^2)\right\}, & r_i \neq \oslash \end{cases} \tag{5.1}$$

where r_i is the RSS measurement, ρ is the probability of a missed packet, $\mathcal{N}(r_i; \nu_i, \sigma_i^2)$ is the normal function evaluated at r_i for mean ν_i and variance σ_i^2, $\epsilon > 0$ is a small-valued lower bound on the probability value away from zero, and γ is a constant such that the sum of the pmf equals one. The use of the minimum probability ϵ is due to the fact that in practice, we may observe values far from the mean more often than described by (5.1) and (5.2) because temporal fading does not always fit the log-normal distribution [14]. Using a small value ϵ conveys the model uncertainty and avoids numerical issues with very low probabilities in the proposed classifiers. Unless otherwise stated, we let $\epsilon = 0.0001$, and $\rho = 0.03$.

To estimate the mean and variance of link i's off pmf is not known a priori, we estimate these parameters from a 5 second calibration period in which it is known that the boundary

is not being crossed. To estimate ν_i, we use the median of the RSS measurements during calibration since the sample median is more robust to outliers than the sample average. To estimate σ_i^2, we use the maximum of the sample variance of the RSS measurements during calibration and a minimum constant $\omega^2 > 0$. Due to quantization of RSS, the sample variance may be zero even though the true real-valued received power would have had a positive variance. We impose a minimum variance of $\omega^2 > 0$ to avoid numerical instability. Unless otherwise stated, we let $\omega = 0.75$(dB).

Since our classifiers do not use labelled training data, we do not have access to RSS measurements when a person is crossing the boundary and thus have no way of knowing the pmf of RSS during a link line crossing. In outdoor deployments where line-of-sight exists, our experience is that we are likely to see a decrease in RSS. Thus, in an effort to make the model simple to compute, we set the "on link line" pmf for link i as,

$$f(r_i \mid \text{On}) = \begin{cases} \rho, & r_i = \oslash \\ \frac{1}{\gamma} \max\left\{\epsilon, \mathcal{N}(r_i; \nu_i - \Delta, \eta\sigma_i^2)\right\}, & r_i \neq \oslash \end{cases} \tag{5.2}$$

where Δ is the average decrease in RSS on a link due to a person's presence, and $\eta > 0$ is a factor by which the variance is increased due to a moving person on the link line. We use the same estimate for ν_i and σ_i^2 as we used for link i's off pmf, and unless otherwise stated, we let $\Delta = 5.0$ dB and $\eta = 4.0$.

5.3.3 Maximum Likelihood Classifier

In this section, we describe our first proposed classifier which we call the maximum likelihood classifier (MLC). Given that a person is either crossing one of the short segments j or not crossing the boundary at all ($j = 0$), we know for each link i whether or not the RSS should be in the on or off link line state. We map the relationship between crossing short segment j and crossing link line i as a *codeword*. The codeword for a person crossing short segment j is $\mathbf{w}(j) = [w_1(j), w_2(j), \ldots, w_L(j)]^T$ where $w_i(j) = 1$ if by crossing j, the person also crosses link i. Formally,

$$w_i(j) = \begin{cases} 1, & \text{if } (l_i \leq j) \text{ and } (j+1 \leq k_i) \\ 0, & \text{otherwise} \end{cases} \tag{5.3}$$

where k_i and l_i are the endpoints of link i, and $k_i < l_i$, without loss of generality.

From the codeword, we can decide if r_i is a sample from $f(r_i \mid \text{Off})$ or $f(r_i \mid \text{On})$. The probability of observing r_i given short segment j is crossed can be computed as $b_j(r_i) =$

$f(r_i \mid \text{On})^{w_i(j)} f(r_i \mid \text{Off})^{1-w_i(j)}$. Since $w_i(j) \in \{0, 1\}$, we pick off the probability of observing r_i given the crossed short segment. By applying independence between RSS measurements on the links, we obtain the likelihood of observing $\mathbf{r}$ by

$$b_j(\mathbf{r}) = \prod_{i=1}^{L} f(r_i \mid \text{On})^{w_i(j)} f(r_i \mid \text{Off})^{1-w_i(j)}. \tag{5.4}$$

The MLC decides which short segment j was crossed as,

$$\hat{j} = \arg\max_{0 \le j \le N-1} b_j(\mathbf{r}). \tag{5.5}$$

5.3.4 Hidden Markov Model Classifier

In this section, we describe a hidden Markov model (HMM) classifier that decides what short segment j was crossed. The HMM classifier (HMMC) is based on the forward algorithm [15]. We say that the boundary can be in one of N states at any given time: an "off" state which is when no short segment is being crossed; or a state that short segment j is currently being crossed. We denote the off state as S_0 and crossing-short-segment-j state as S_j. The probability that the HMM begins in S_j is denoted $\boldsymbol{\pi} = \{\pi_j\}$ where

$$\pi_j = P[q_1 = S_j], \quad 0 \le j \le N-1 \tag{5.6}$$

and q_1 is the state of the HMM for the first RSS measurement. In this paper, we let $\pi_0 = 0.9$ and $\pi_j = \frac{1}{N-1}(1 - \pi_0)$ for $j \neq 0$. The one-step transition probability from state i to state j, a_{ij}, is defined as

$$a_{ij} = P[q_{t+1} = S_j \mid q_t = S_i], \quad 0 \le i, j \le N-1. \tag{5.7}$$

In this paper, we assume that the boundary will be crossed infrequently and so the HMM will likely stay in S_0. Under this assumption, we let $a_{00} = 0.75$ and $a_{0j} = \frac{1}{N-1}(1 - a_{00})$ for $j \neq 0$. When the boundary is crossed, we assume that the person moves off the boundary quickly. As such, we let the probability $a_{jj} = 0.6$ for $j \neq 0$ and $a_{j0} = 1 - a_{jj}$ for $j \neq 0$. All other entries not specified are 0 since a boundary crosser will only cross one short segment at a time. The HMM uses (5.4) to describe the probability of observing $\mathbf{r}$ given state j.

With this model, we are interested in solving the problem of: what is the most likely current state given a history of past $\mathbf{r}$ observations? The forward solution to the HMM answers this question with computational efficiency [16], inductively computing a vector

$\alpha_t(j)$ at each time t for each state j, and then estimating the crossed short segment as $\hat{j} = \arg\max_{0 \le j \le N-1} \alpha_{t+1}(j)$. The forward algorithm initializes $\alpha_1(j) = \pi_j b_j(\mathbf{r}_1)$, and then computes $\alpha_{t+1}(j) = \left[\sum_{i=0}^{N-1} \alpha_t(i) a_{ij}\right] b_j(\mathbf{r}_{t+1})$ for each $t > 0$ and for $0 \le j \le N-1$.

5.3.5 On-the-fly Model Update

For wireless RF links, changes in temperature, humidity and movement of foliage during windy periods can cause the distributions of RSS to change compared to those taken at a prior time [7]–[9]. An example of changes caused by heavy rainfall can be seen from our own data collection in Figure 5.4. We observe that as the rain starts, the RSS on this link drops steadily by approximately 8 dB in five minutes. After the rain stops, the RSS on the link increases, over two hours, back to approximately the same value prior to the start of the rain. This happens because, as the rain collects on the surface of the soil, the electromagnetic properties of the soil also change [17]. The phases and amplitudes of any reflection from the soil change, and thus the RSS changes as a result. As the rain abates, the water gradually evaporates or is drawn into the soil and over the course of hours, the electromagnetic properties of the soil are restored to the pre-rain state.

Gone unchecked, these time-varying changes to RSS caused by weather conditions would degrade the performance of the classifiers. To address these realities, we periodically update each link's on and off pmf using a history of RSS measurement. However, the history of measurements only include those that are observed when it is likely that no one is crossing the boundary, i.e. $\hat{j} = 0$. To accomplish this, we add the current RSS measurement r_i into a M-length FIFO buffer when $b_0(\mathbf{r}) > \kappa$ for the MLC and $\alpha_{t+1}(0) > \kappa$ for the HMMC. After β new RSS measurements are added into the buffer, ν_i and σ_i^2 are re-estimated for each link i using the measurements from their buffers. The re-estimated parameters are then used to update the off and on pmfs for each link simultaneously. In this paper, we set $\kappa = 0.6$, $M = 50$, and $\beta = 18$. The buffer size allows us to update our models approximately every 5 seconds. Our model-update can quickly adapt to RSS changes caused by weather events because the rate of change of RSS during a weather event, like rain, is typically hundreds of times slower than the change caused by a person crossing.

5.3.6 Baseline Classifiers

In this section, we briefly describe four baseline classifiers against which we compare our proposed classifiers. The first two classifiers, from [6], make use of a binary vector that is produced by link line crossing detectors that determine the crossed-state of each link. The closest codeword classifier (CCC) finds the closest match, in Hamming distance, between the binary vector measurement and the same codewords referenced in Section 5.3.3. The short segment j whose codeword is closest in Hamming distance to the observed binary vector is used as the classified short segment crossed. Unlike the CCC, the simple classifier (SC) operates on a network of nodes where links form only between nodes j and $j+1$, for $j \in \{1, \ldots, N-1\}$. The SC decides short segment j is crossed only when its associated link measures a crossing. The SC ignores the measurements on longer links thus relying only on the individual shorter links for classification.

The third classifier is based on radio tomographic imaging (RTI) [2] and we refer to it as the radio tomographic imaging classifier (RTIC). The objective of RTI is to estimate an image of RF signal attenuation using RSS measurements on a network of RF links. The implementation of RTI in this paper uses the difference between a short and long term RSS average as the measurement vector from which we estimate the image. The image is estimated for each new vector measurement and the pixel with the greatest value is chosen as the location of the person. However, if the maximum pixel value is below a threshold, the boundary is assumed to be vacant. When RTI is applied to the boundary crossing localization system in this paper, the image we wish to estimate is one row of pixels that extends from node 1 to node N. Each pixel maps to one short segment, thus the RTIC maps the location estimate from RTI to the short segment j crossed. When the maximum pixel value is below a threshold, RTIC decides $\hat{j} = 0$.

The last classifier is based on the fingerprint-based system, *Nuzzer* [18]. In *Nuzzer*, training RSS measurements are recorded as a person moves around in several distinct locations. Histograms of the RSS for each link are saved in a database for each of the areas in which the person is moving. In the *Nuzzer* classifier (NC) used in this paper, RSS measurements are recorded when a person stands far from the boundary, when a person walks along each short segment j, and when a person walks 1.21 m away from and parallel to each short segment. As explained in [18], the likelihood of $\mathbf{r}$ collected during

testing is computed for each location using the probabilities from the training histograms. Smoothing is applied by multiplying a number of consecutive likelihoods. The NC decides $\hat{j} = 0$ if the maximum "smoothed" likelihood maps to any of the locations where the person was far from the boundary or if they were walking parallel to a short segment. Otherwise, the short segment with the maximum smoothed likelihood is classified as the crossed short segment. We apply a similar update method to NC as we designed for the MLC and HMMC in Section 5.3.5. In this update method, $\mathbf{r}$ is added to a buffer when $\hat{j} = 0$. When β new measurements have been added to the buffer, the histograms associated with a person far from the boundary are updated.

5.4 Experimentation

In this section, we describe the equipment, environment, experimental setup and metrics we use to quantify the performance of the proposed and baseline classifiers.

5.4.1 Equipment and Setup

Our nodes are Texas Instrument CC2531 USB dongles which follow a TDMA protocol and transmit +4.5 dBm power in the 2.4 GHz ISM band. An extra node overhears the wireless traffic and records $\mathbf{r}$ on a computer. On 1 meter tall stands, six nodes are deployed 4.6 m apart, making the total border length 23 m long. We measure RSS on all links and on four channels every 100 ms. Although we measure on four channels, it requires additional transmit energy and bandwidth compared to one channel. As such, in this paper, we analyze the performance of the classifiers when RSS measurements on one or on all four channels are available.

Using different deployments, we show how one of the proposed classifiers performs in a real-time system. We also demonstrate how the performance of the proposed classifiers compare to the baseline classifiers in post-processing. One contribution of this paper is that we test the HMMC in a real-time system over a three month period. We build and deploy a system in which each node is powered by solar-rechargeable batteries. Additionally, a solar-powered BeagleBone Black is used to record RSS measurements and run the HMMC to perform real-time boundary crossing localization. We envision that the result could be sent to a server and used to remotely monitor or dispatch someone to the boundary; our

deployed system simply captures and saves a webcam image along with the date, time, and estimated crossing location, to file [19]. We use these photos to establish the ground truth.

The HMMC in our deployment operates on the RSS measurements from all four channels, using 75% more power than when it measures on only one channel. However, we ran our three month deployment using four channels because it was within the capacity of our solar-rechargeable batteries, and we wanted to achieve the best performance possible.

In addition to the real-time setup, we also show how the performance would be affected in the real-time system if other classifiers or classifier parameters had been used. To that end, we perform many experiments where we record RSS measurements to file and run our proposed and baseline classifiers on those data sets in post-processing. In this paper, nodes are deployed in a variety of locations and weather conditions. The RSS measurements on all four channels are recorded in these cases. Note we evaluate the classifiers using data from either one or all four channels in Section 5.5.2.1.

5.4.2 Experiments

5.4.2.1 Experiments for Post-Processing

To compare the performance of our proposed and baseline classifiers, we conduct a total of nine data collection experiments over the course of a month and a half at three different locations shown in Figure 5.5. We refer to these locations as the field, the school, and the natural area. There are two large deciduous trees that stand within 6.1 meters of the nodes at the field, and five deciduous trees that stand within 1.5 meters of the nodes at the school. However the natural area is marked with high grasses, low shrubs, and deciduous seedlings and trees. Seven of the nine data collection experiments are conducted in the field. In three of these seven experiments, measurements are recorded on sunny, calm days. In the other four experiments, we record several hours of RSS before, during, and after light to heavy rainfall. The experiments at the school and at the natural area are performed during times of wind with gusts up to 5.4 m/s measured by an anemometer. Since weather events, such as rain, cause time-varying changes in RSS, we expect that classifiers would perform the worst during these times. As a result, we purposefully chose to over-represent periods of rain so that we could learn more about the system when classification was most

challenging. In all, 77.6 hours worth of RSS measurements are recorded over the nine experiments.

For each of the nine experiments, a person crosses the boundary at least 100 times and he or she records the crossing time and the short segment crossed. In most cases, ten seconds separate each of the crossings, although as much as 60 s elapse between some crossings to ensure the crossing times are properly logged. Data is then recorded for a time period when no one crosses the boundary, but when there may be activity near the boundary. An experiment lasts anywhere from one to fifteen hours. During this time, a rain meter and/or anemometer are used to collect the amount of rainfall and the wind speed near the deployment. We use these data sets to analyze the performance of each classifier during different weather events.

5.4.2.2 Experiments for Real-Time System

Two types of experiments are performed in the real-time system, which is deployed for three months in the field location. As the real-time system runs, we perform controlled tests where we record the time and location of 2887 boundary crossings. We then compare the true crossing times with the images saved to file on the BeagleBone Black. The second type of experiment we perform captures images during detected boundary crossings without a person purposefully crossing the boundary. The field is in the backyard of a residence, and some of these crossings (as shown by the captured images) are due to residents or animals crossing, and some are false alarms.

5.4.3 Validation Metrics

Each classifier may produce false alarms or misclassify the true crossed short segment. A false alarm occurs when, at any observation, the boundary is vacant, i.e. $j = 0$, but the classifier reports $\hat{j} \neq 0$. We compute the probability of false alarm, P_{fa}, by counting the number of false alarms and dividing it by the total number of samples measured when no person is crossing the boundary. Next, a classifier makes a correct classification $\hat{j} = j$ for $j \neq 0$. In the experiments, we record the ground truth time of crossing and the short segment crossed. Due to small errors in the recorded true time of crossing and many samples worth of delay in the baseline classifier algorithms, a classifier may report the correct j but at a delayed time compared to the true crossing. To be fair to all classifiers,

a correct classification in our paper occurs when $\hat{j} = j$ for $j \neq 0$ at any time during a ± 3 second time window. The probability of correct classification, P_{cc}, is thus the number correct classifications divided by the number of boundary crossings. We show an example of the HMMC output for a short test experiment in Figure 5.6. In this short experiment, the HMMC achieves a $P_{cc} = 10/10$ classification rate and produces no false alarms, $P_{fa} = 0$.

None of the classifiers we implement are able to achieve the ideal of $P_{cc} = 1$ and $P_{fa} = 0$ over all experiments. Instead, compromises must be made so that a classifier's tunable parameters are selected to penalize one type of error more than the other. For example, in some scenarios, missing a classification may cost €1000 in stolen goods while a false alarm may only cost €100 to have a worker turn on a video-surveillance system. In a different scenario, a false alarm may waste €1000 in man-power and fuel to investigate a distant boundary, while a misclassification may only cost €100. To quantify the tradeoff between the probability of misclassification, $1 - P_{cc}$, and P_{fa}, we define a cost function C_k:

$$C_k = c_{k0} \cdot P_{fa} + c_{k1} \cdot (1 - P_{cc}) \tag{5.8}$$

where k is the cost function number. The choice of c_{k0} and c_{k1} quantify the cost of each type of error.

5.5 Results

5.5.1 Sensitivity to Parameter Choice

Our classifiers rely on the selection of three tunable parameters. One important feature of our work is that few parameters need to be adjusted to maintain a high performance. With few parameters to adjust, this system can be deployed quickly. In this section, we show how the choice of the parameters affects the performance metrics described in Section 5.4.3. We evaluate performance using the data in post-processing by averaging over all seven data collection experiments, and over all four channels, but using one channel at a time.

5.5.1.1 Link Line Model Parameters

Section 5.3.2 describes the Gaussian models we use for the distributions of RSS when a person is off or on a link line. In this section, we vary the model's tunable parameters Δ, η, and ω. We observe in Figure 5.7 the affect of η and ω and $\Delta = 5$ on performance. In Figure

5.7, we observe a few trends that are common to both the MLC and the HMMC. First, when η increases, both P_{cc} and P_{fa} increase. The η parameter determines the scale of the on link line distribution. A higher η, and thus a wider "on link line" pmf, favors RSS observations coming from the on link line distribution for all links. As a result, we are more likely to correctly classify crossings. But we also increase the chance of misclassifying boundary crossing locations. This trade-off does not seem to be as significant with the choice of ω. When using either the classifier, the user must consider the cost of false alarms and misclassifications when choosing η. Although we have included figures for $\Delta = 5$, we found that Δ should remain between 3 and 7 for best results. For $\Delta < 3$, the on and off link line distributions are considerably overlapped and cause a low classification rate. For $\Delta > 7$, the on link line distribution falls too far away from the observations to reliably classify crossings.

Another important observation from Figure 5.7 is the effect of the classifier on performance. The MLC shows a higher variability in P_{fa} than for the HMMC. Over the parameters tested, the highest false alarm probability for HMMC is $P_{fa} = 7 \times 10^{-5}$ whereas MLC reaches $P_{fa} = 2.5 \times 10^{-4}$. We suspect that this difference is because the HMMC tends to smooth out crossing detections by placing a prior on the observation likelihood. This smoothing characteristic tends to reduce the number of false alarms. However, the smoothing characteristic on the HMMC also reduces the probability of correct classification compared to MLC. The HMMC achieves a maximum of $P_{cc} = 0.9968$ while the MLC achieves a maximum $P_{cc} = 0.9978$. The HMMC is, in general, better when the application asks for few false alarms, but the MLC is more accurate when the application demands a high classification rate.

5.5.1.2 One-Step Transition Probabilities

Both the MLC and the HMMC rely on the likelihood model (5.4) to perform classification. However, the HMMC also makes use of the one-step transition probabilities a_{ij} for $0 \leq i, j \leq N-1$. These are additional parameters that the user must select when implementing the HMMC, so we would like to know how performance responds to the choice of these transition probabilities. In Section 5.3.4, we described how the transition probabilities could be defined in terms of a_{00} and a_{jj} for $j \neq 0$. We loop over many values

for these parameters and record P_{cc} and P_{fa} for the HMMC. We observe in Figure 5.7 the affect of a_{00} and a_{jj} on performance.

In Figure 5.7, we observe distinct features common to both P_{fa} and P_{cc}. First, the general trend shows that as a_{00} increases, P_{cc} decreases while P_{fa} increases. When a_{00} is small, we increase the probability that on the next RSS observation, the HMM will transition from S_0 to S_j for $j \neq 0$. The model favors leaving S_0. Thus, we observe a high P_{cc} and a high P_{fa}. However, when a_{00} is high, the model favors staying in S_0. Thus we observe fewer false alarms but also fewer correct classifications. The opposite trend is true for a_{jj}: P_{cc} and P_{fa} tend to increase as a_{jj} increases. A small a_{jj} favors transitions to S_0 if the HMM is currently in state S_j for $j \neq 0$. In this case, it is likely the HMMC will result in $\hat{j} = 0$ which yields a low P_{fa} and P_{cc}. However, when a_{jj} is large, the model favors staying in S_j for $j \neq 0$ on the next observation. As a result, we observe increases in both P_{cc} and P_{fa}.

One very distinct part of the relationship between P_{fa}, P_{cc}, and the transition probabilities is the contour between the relatively flat sections and steep sections. The flat regions suggest that when a_{00} and a_{jj} are appropriately chosen, the transition probabilities carry much less significance in the classification process. But poorly chosen transition probabilities can be significantly detrimental by causing a sharp increase in P_{fa} without a equally significant increase in P_{cc}. The take away from this analysis is to choose a_{00} and a_{jj} inside of the flat region to avoid costly increases in P_{fa}.

5.5.2 Classifier Comparison

In this section, we compare the performance of the proposed and baseline classifiers discussed in Section 5.3.6. We foresee two kinds of deployments in which one may implement any of these classifiers. In the first type of deployment, the system remains in the same location and the user has time to tune the parameters of the classifier. A person who wishes to monitor a relatively short boundary and never moves the nodes may fall in this category. In the second type of deployment, the user must quickly deploy the system in any type of environment, and there is no time to tune the classifier parameters. This situation may be common to a group who must protect miles of boundary and tuning parameters would require an inordinate amount of time. In either case, we are interested in implementing the classifier with the best performance.

In the following sections, we show the performance of all six classifiers when we are able to tune their parameters. Then, using the parameters that provide an optimal performance, we show how these classifiers perform when the system encounters a variety of weather conditions and when it is moved to a new location. By doing so, we analyze the performance of each classifier when no parameter tuning is performed.

5.5.2.1 Performance With Tuning

We begin by running the six classifiers on the data from the seven field experiments on each of the four channels individually. For each classifier, we loop through several combinations of parameter values and record the average P_{cc} and P_{fa} over the four channels. We show the results of this process in Figure 5.8.

The ROC shows the relationship between P_{cc} and P_{fa} as the classifier parameters change. Even though none of the classifiers achieve the ideal of $P_{cc} = 1$ and $P_{fa} = 0$, some classifiers are able to approach this ideal better than others. The first observation is that NC performs the worst of the classifiers. The performance of NC suffers since the "on link line" training measurements collected on the first day gradually drift. The NC tends to have few false alarms since the histograms associated with $j = 0$ (off link line) are being updated. As new measurements are observed, the new measurements will tend to match the measurements from these updated histograms more than the histograms associated with a person moving on a short segment.

We also observe that the SC does not perform as well as the other classifiers. We suspect that this is because the SC does not incorporate the measurements from the longer links of the network for classification. Next, we compare the final 4 classifiers. The inset of the ROC in Figure 5.8 shows that RTIC, CCC, HMMC, and MLC all come close to achieving the ideal. However, MLC and HMMC appear to come closest to the ideal, followed by the CCC and then the RTIC. Although the CCC, which relies on binary measurements, outperforms the RTIC, it is outperformed by both MLC and HMMC. The proposed classifiers differ from the CCC in that they use soft values in classification whereas the CCC uses binary values.

To get a better sense of how these classifiers compare, we fix the classification rate to be $P_{cc} = 0.995$ and find the lowest false alarm rate for each classifier. We then fix the

false alarm rate to be $P_{fa} = 5.0 \times 10^{-5}$ and find the lowest misclassification rate for each classifier. We show the results in Table 5.1. We observe that for a fixed P_{cc}, the MLC and the HMMC outperform the CCC by one order of magnitude and the SC by four orders of magnitude. For fixed P_{fa}, the MLC and the HMMC outperform the CCC and RTIC by an order of magnitude and the SC by two orders of magnitude.

We have only considered the case of measuring RSS on one channel. Now we analyze the performance of the MLC and the HMMC when RSS is measured on four channels. We again run the MLC and HMMC with many parameter combinations on the data from the seven field experiments. For many of these parameter combinations, the MLC and HMMC both achieve 100% classification of all 901 boundary crossings. The MLC and HMMC, in terms of misclassification, is therefore no greater than $1/901 = 1.11 \times 10^{-3}$. We show in Table 5.2 that, for a fixed $P_{fa} = 2.5 \times 10^{-5}$, the classifiers that operate on RSS measurements from four channels reduces the misclassification rate by at least one order of magnitude. Although the additional channels provide even better performance than for a single channel, this advantage must be weighed against the increased power usage to transmit on the additional channels. When power consumption must be minimized, measuring on one channel reduces the power usage by 75% compared to a network that measures on four channels.

5.5.2.2 Performance Without Tuning

In the previous section, we analyzed the performance of all six classifiers in the case when we were able to tune their parameters for a deployment in one location. In this section, we consider the case where the parameters for each classifier have already be optimized to meet some specification. We then test the performance of these classifiers in a variety of weather conditions and at different experimental locations. By doing this, we analyze how each classifier performs in a variety of environments when the parameters are fixed. Next we describe the data sets we use and how we choose optimal parameters for each classifier.

Different from the previous sections, we organize data-collection experiments by the type of weather condition: sun, rain, wind, and all-weather which are mentioned in Section 5.4.2. The all-weather group is the sun, rain, and wind data combined into one. Note

the wind data is composed of data collected at the school and at the natural area. The sun and rain data, however, come from only the field location. For each weather type, we separately log the number of correct classifications, the number of true crossings, the number of false alarms, and the total number of RSS observations in the four types of weather conditions. We run all classifiers except the NC on each channel separately and then average the number of correct classifications and the number of false alarms for all four channels. We obtain P_{cc} and P_{fa} for each classifier in each weather condition. We note here that we do not consider the performance of the NC since we saw in the previous section that it is unable to achieve a high classification rate; furthermore, retraining such a classifier, in many situations, would be too costly.

Next, two sets of optimized parameters for each classifier are chosen through an optimization process. Using the P_{cc} and P_{fa} results from Section 5.5.2.1, we record the parameters that minimize two cost functions, C_0 and C_1, defined in (5.8). The cost function C_0 penalizes false alarms the most by setting $c_{00} = 1000$ and $c_{01} = 100$. The optimal parameters for each classifier with this cost function would be ideal for situations where the cost of investigating a boundary crossing costs time and resources. On the other hand, the cost function C_1 penalizes misclassifications the most by setting $c_{10} = 100$ and $c_{11} = 1000$. The optimal parameters for each classifier with this cost function would be ideal for situations where knowing the true crossing state is imperative while risking the chance of some false alarms is allowable.

Using the optimized parameters, we run the classifiers on all four weather data sets and record P_{cc} and P_{fa}. We use these new P_{cc} and P_{fa} values to compute new cost values, C_0' and C_1', using the same c_{k0} and c_{k1}, for each classifier and each weather condition. We show these new costs of running each classifier on the data sets mentioned above in Figure 5.9.

In Figure 5.9, we observe, first, that the SC performs the worst in all weather conditions regardless of the optimized parameters used. The SC does not make use of all of the RSS measurements in this network configuration so it performs the worst. The best classifiers are the CCC, MLC, and HMMC when comparing the sun, rain, and all-weather data and in both optimized regimes. But in both optimized regimes, either the MLC or the HMMC perform the best. The numeric values for the CCC, MLC, and HMMC costs are shown

in Table 5.3. The HMMC performs the best in these three weather conditions when the parameters are optimized to reduce false alarms. The HMMC showed this property in Section 5.5.1.1 where compared to the MLC, the HMMC was a better classifier for reducing false alarms. In contrast, the MLC outperforms the HMMC in the all-weather and rain conditions when we optimize parameters for correct classifications. The HMMC and the MLC are both comparable in the sunny weather. Again, this characteristic of the MLC appeared in Section 5.5.1.1 where compared to the HMMC, it was the superior classifier for correct classification.

We also see that the CCC is the second best classifier in many of the weather conditions and optimization regimes. This comes at little surprise in that the ROC curve in Figure 5.8 showed the CCC was only slightly less accurate than the HMMC and MLC. Perhaps the more surprising result is that the RTIC is the best classifier in windy locations and when optimizing for correct classifications. And, since the windy data sets were performed at two different locations, the RTIC performs the best out of the classifiers when the system is moved to new locations and when the classifier parameters are fixed. The MLC, however, is the best choice in windy conditions when we want to minimize false alarms.

We separately obtain cost values for the MLC and the HMMC when we disable the on-line model update feature. In both the C_0' and C_1' regime, the MLC and HMMC with the update feature enabled lowered the cost by 1 to 2 orders of magnitude with the sun data and lowered the cost by 2 to 3 orders of magnitude with the rain data compared to these classifiers when the update feature was disabled.

From this analysis, we draw a few conclusions about our classifiers. First, the on-line model update feature is necessary to operate reliably during weather events. Second, when we take all weather conditions (sun, rain, and wind) into account, the MLC is the best classifier when correct classifications are important, but the HMMC is the best classifier when minimizing false alarms. However, it is advantageous to use the RTIC in windy conditions when correct classification is needed; the MLC, however, is the best choice in windy conditions when false alarms must be minimized.

5.5.3 Relative Costs

In this evaluation, we compare the costs of using the MLC and the HMMC by optimizing their parameters over many cost functions (5.8). In the previous section, we considered cases where the cost of a misclassification or a false alarm was ten times as costly as the other rate. However, there are an infinite number of cost parameters c_{k0} and c_{k1} a user may want to consider. To address this, we consider a relative cost C_{rel} which is a function of a ratio of the cost parameters where one of the cost parameters is fixed. In this section, we fix $c_{k0} = 1000$ and vary c_{k1} to be values between 1 and 100,000. Using the results from Section 5.5.2.1, we then obtain the parameters for the MLC and the HMMC that minimize C_{rel}. We then run the MLC and the HMMC using their optimized parameters on the all-weather data described in 5.5.2.2 to obtain values for P_{cc} and P_{fa}. These rates are then used to compute new relative costs C'_{rel}. We show the new relative costs in Figure 5.10.

We observe that when the cost of a misclassification is 2 or more times as expensive as the cost of a false alarm, the MLC can save more in cost compared to the HMMC. When the cost parameter ratio is in this regime, the classifier parameters are optimized to minimize misclassifications. When the cost parameter ratio, however, is less than 0.2, the HMMC generally reduces the overall cost. When the cost parameter ratio is in this regime, the parameters are optimized to minimize false alarms. Due to limited space we do not include plots, but the same general results are seen in the sun and all-weather data sets. In windy conditions, the MLC is the preferred classifier regardless of cost ratio.

5.5.4 Real-Time Performance

In this final evaluation, we report the results of the real-time, three month deployment. We captured webcam images of when the system detected a boundary crossing during both controlled and uncontrolled periods. During the controlled experiments, a person crossed the boundary 2887 times. Of those crossings, 81.6% were correctly classified by the real-time HMMC. We note that the classification rate is 18% less than what is reported in the previous sections. Further investigation of the real-time system showed that approximately one out of six seconds worth of RSS measurements was not recorded by the BeagleBone Black. During the one second of missing measurements, the BeagleBone requests weather data from a website and saves it to file. We did not anticipate that the

web request and saving would result in missed RSS measurements when we deployed the real-time system. As a result, 1/6 or 16.6% of the RSS measurements during a crossing were missing. This percent of missed measurements gives some explanation about the 18% lower classification rate between the real-time and post-processing results.

After changing the real-time system to refrain from requesting weather data, we run the real-time system for an additional five days, during which, a person crosses the boundary 1502 times. All 1502 crossings were correctly classified, which indicates that the probability of misclassification $1 - P_{cc}$ is less than $1/1502 = 6.7 \times 10^{-4}$. This classification performance matches values reported for post-processing in Section 5.5.2.1.

During the three month long uncontrolled deployment, the real-time system operated continuously during sunny, rainy, and windy weather. In all, 850 boundary crossing locations by people and animals were correctly classified. The true classification rate is unknown, however, because the total number of true crossings during the uncontrolled period is unknown. The system also reported 298 false alarms. Roughly 69 million RSS measurements were taken during this deployment, which results in a false alarm probability of 4.3×10^{-6}, or an average of 3.7 false alarms per day. We note that this rate is lower than the lowest 21.6 false alarms per day average achieved in post-processing. To reduce this rate, another row of nodes could be deployed to verify crossing detections. For example, the extra nodes could be placed at lower or higher heights or they could be deployed parallel to the first row of nodes. This adds yet another layer of redundancy to mitigate errors. We also found that false alarms were more likely to occur during weather events. False alarms could be further reduced by ignoring RSS measurements that have the same signature as those cause by wind or rain.

5.6 Related Research

Outdoor boundary crossing localization using sensing systems has been a topic of research for many years. Since it cannot be assumed that the boundary crosser carries a tag that cooperates with the sensing system, boundary crossing localization typically revolves around DFL technologies. The sensing devices, however, vary considerably. Proximity sensors have been widely used. For example, significant research has been conducted using passive infrared (PIR) sensors for outdoor localization [20], [21] where

the sensors detect thermal radiation from a person. These studies have investigated not only the localization algorithms [20], but also their energy efficiency [21]. A major disadvantage of PIR sensors is that they lose the ability to track moving objects in forested or vegetated landscapes where obstructions occlude the sensors' field of view. In addition, PIR sensors' performance suffers during daylight times when the infrared radiation from the sun saturates the sensor. Cameras have also been proposed as a sensing technology for boundary surveillance [22]. When boundaries are monitored day and night, cameras become useless at night or in fog when it is not possible to image and thus detect and localize boundary crossers. Moreover, cameras mounted on aerial units cannot image objects that are occluded from above, e.g. by a forest canopy.

Fiber optic and pressure sensors have been used in boundary security applications to detect when a person's footsteps [23]. These sensors are either buried underneath the boundary or are strung along a fence. Installing buried sensors involves heavy equipment digging up earth. Maintenance also poses a problem since the cable must be unearthed for visual inspections and to perform repairs. Pressure sensors strung along the fence first requires the fence which is economically costly operation.

In contrast, RF signals, which we use in this paper, operate day and night, can pass through leaves and other vegetation, and can operate during fog and other weather conditions. The sensors are easily deployed, can be easily maintained, and do not require a fence to perform sensing. One type of RF sensing includes radar which has been used to detect human presence in wooded areas [24]–[26] and even distinguish human presence from a soldier and a vehicle [27]. We note one well-reported commercial radar system used for boundary crossing localization produced false crossings during weather events and only worked 30% of the time [26], [28]. Radar uses a signal whose power decays with distance d as $1/d^4$, thus transmit power must be increased dramatically to increase sensing range. Our work closely matches other DFL methods that measure changes in the channel of RF links and whose power decays as $1/d^2$. These methods have been heavily tested in indoor environments.The work in [6] is optimized for linearly deployed nodes, but no testing is performed during weather events. Furthermore, [6] uses binary link line crossings. We show that methods using soft link line crossing measurements outperform localization methods that use hard crossing decisions. The methods we develop in this

paper are optimized for linearly deployed sensors, and we show that they outperform current DFL technologies. Additionally, our model update feature allows us to achieve low error rates despite weather-induced propagation changes.

5.7 Conclusion

In this paper, we developed and tested two RSS-based crossing segment classifiers to localize boundary crossings. These classifiers used models whose parameters could be re-estimated from a history of RSS to adapt to changes caused by weather events. We evaluated our classifiers from experiments performed in three locations and in a variety of weather conditions. Using 77.6 hours worth of RSS measurements, we analyzed our classifiers in terms of sensitivity to system parameters. We found that the HMMC is better when the application asks for few false alarms, but the MLC performs better when the application demands a high classification rate.

When we compared the MLC and HMMC to four baseline classifiers, we found that the MLC and HMMC outperformed the other classifiers by 1 to 4 orders of magnitude in terms of false alarm probability. We also showed that the MLC and HMMC were the best classifiers in sunny, rainy, windy and in overall weather conditions when we fixed the classifier parameters to avoid false alarms. In addition, the MLC was more accurate than the HMMC when parameters were optimized to minimize misclassifications. Our three-month duration real-time six node boundary crossing system deployment achieves high reliability, with a misclassification rate of less than 7×10^{-4} and false alarm rate of 4×10^{-6}. In summary, using an MLC and HMMC algorithm on RSS data from a linearly-deployed network provides highly reliable boundary crossing localization across a variety of weather conditions and in multiple locations. We demonstrated that these classifiers can perform better than baseline DFL classifiers by tuning system parameters or using fixed, optimized parameters.

5.8 Acknowledgment

This material is based upon work supported by the National Science Foundation under Grant Nos. #1407949 and #1035565.

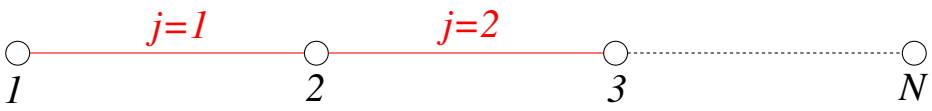

Figure 5.1. Nodes and short segments j in localization system.

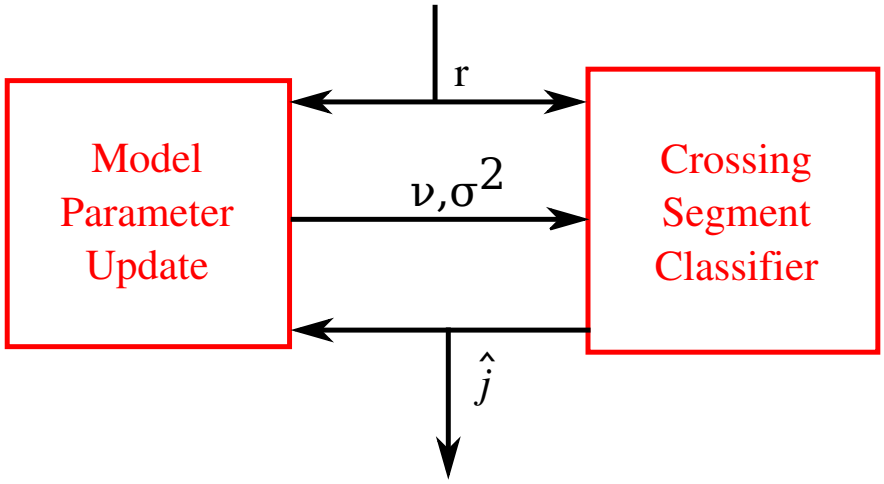

Figure 5.2. Block diagram of the proposed localization system.

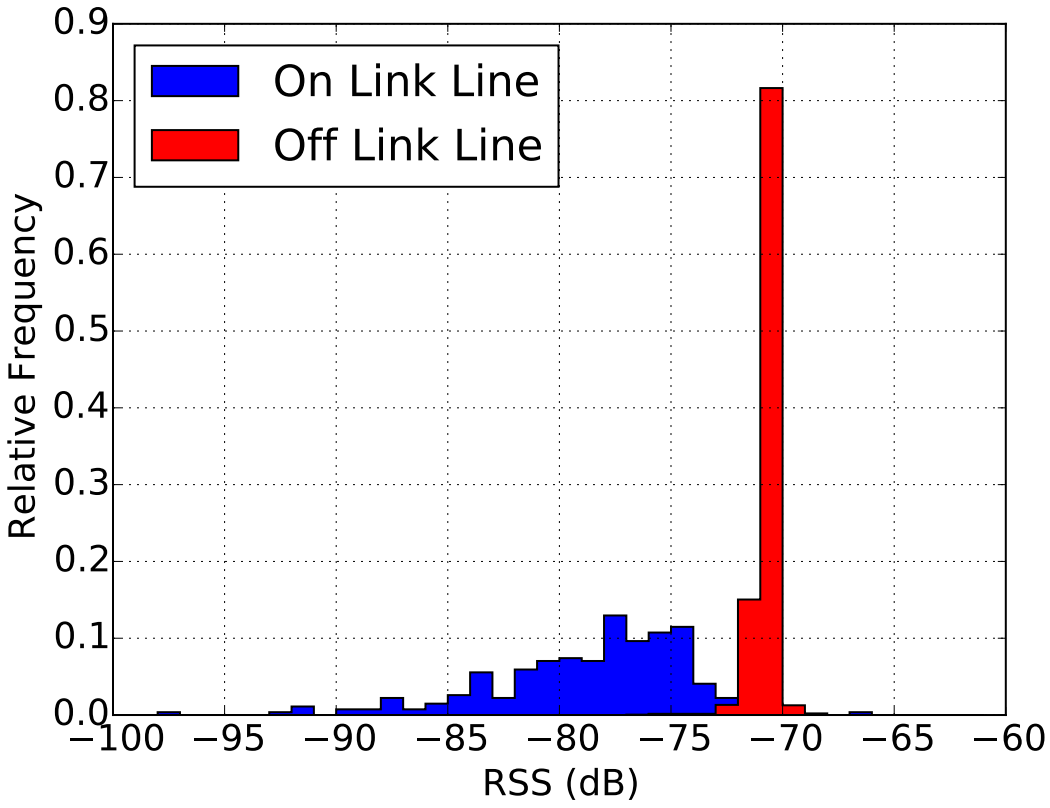

Figure 5.3. Relative frequencies of RSS measurements when a person is on, and off, a link line.

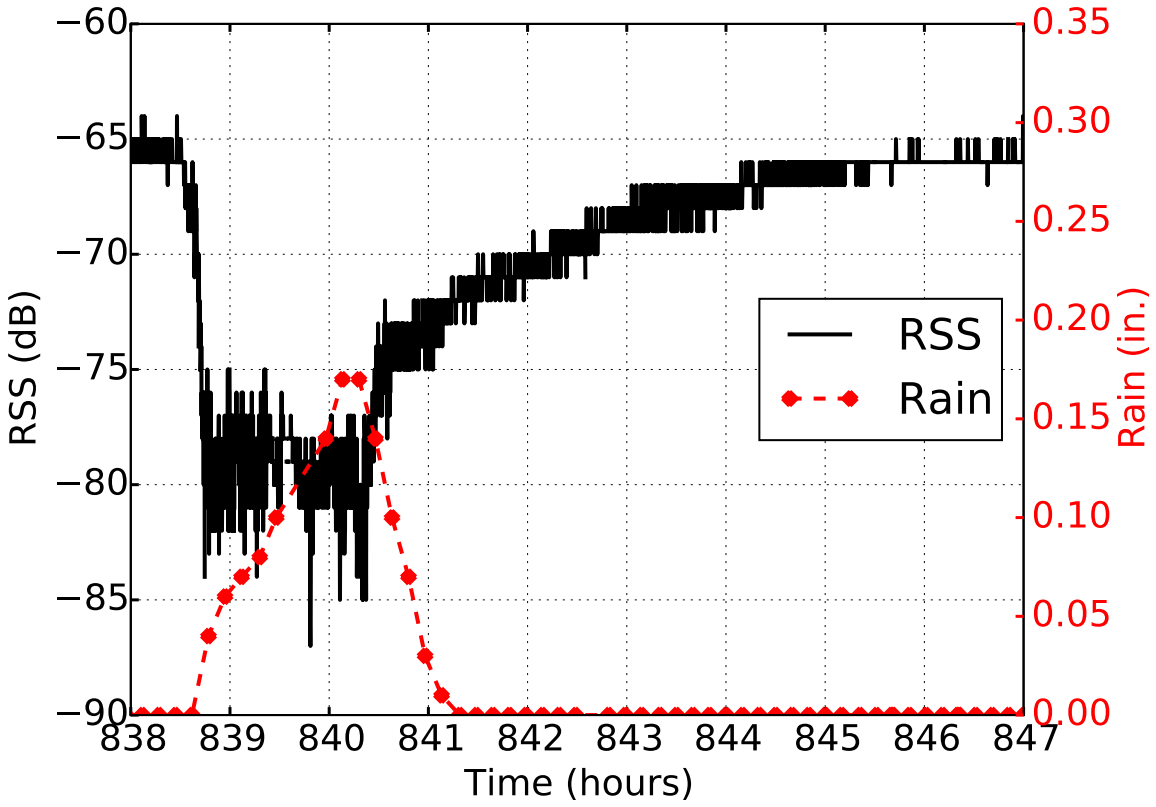

Figure 5.4. A link's RSS decreases over minutes during the start of rain and returns to the pre-rain level after the rain subsides.

Figure 5.5. Experiment locations: (left) Field (middle) School (right) Natural Area.

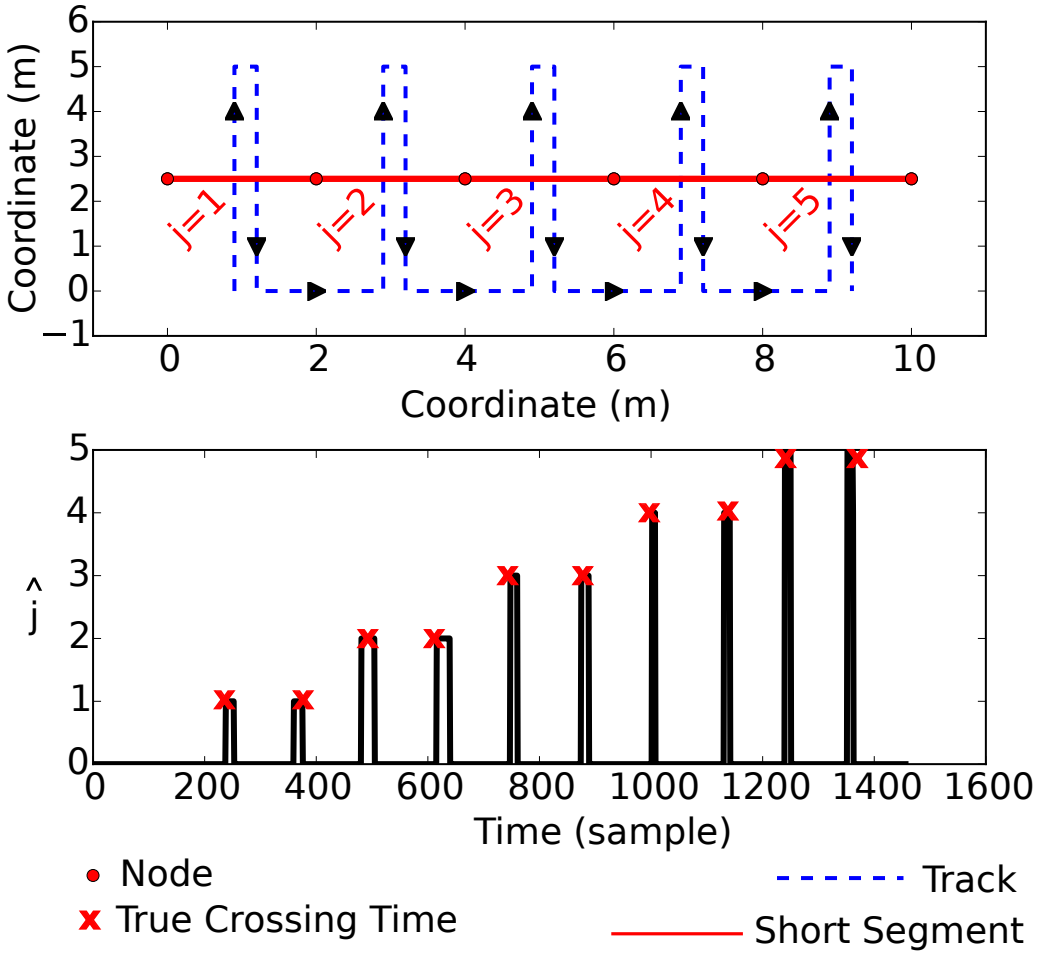

Figure 5.6. (above) The track of the person. (below) Output of HMMC for a short experiment.

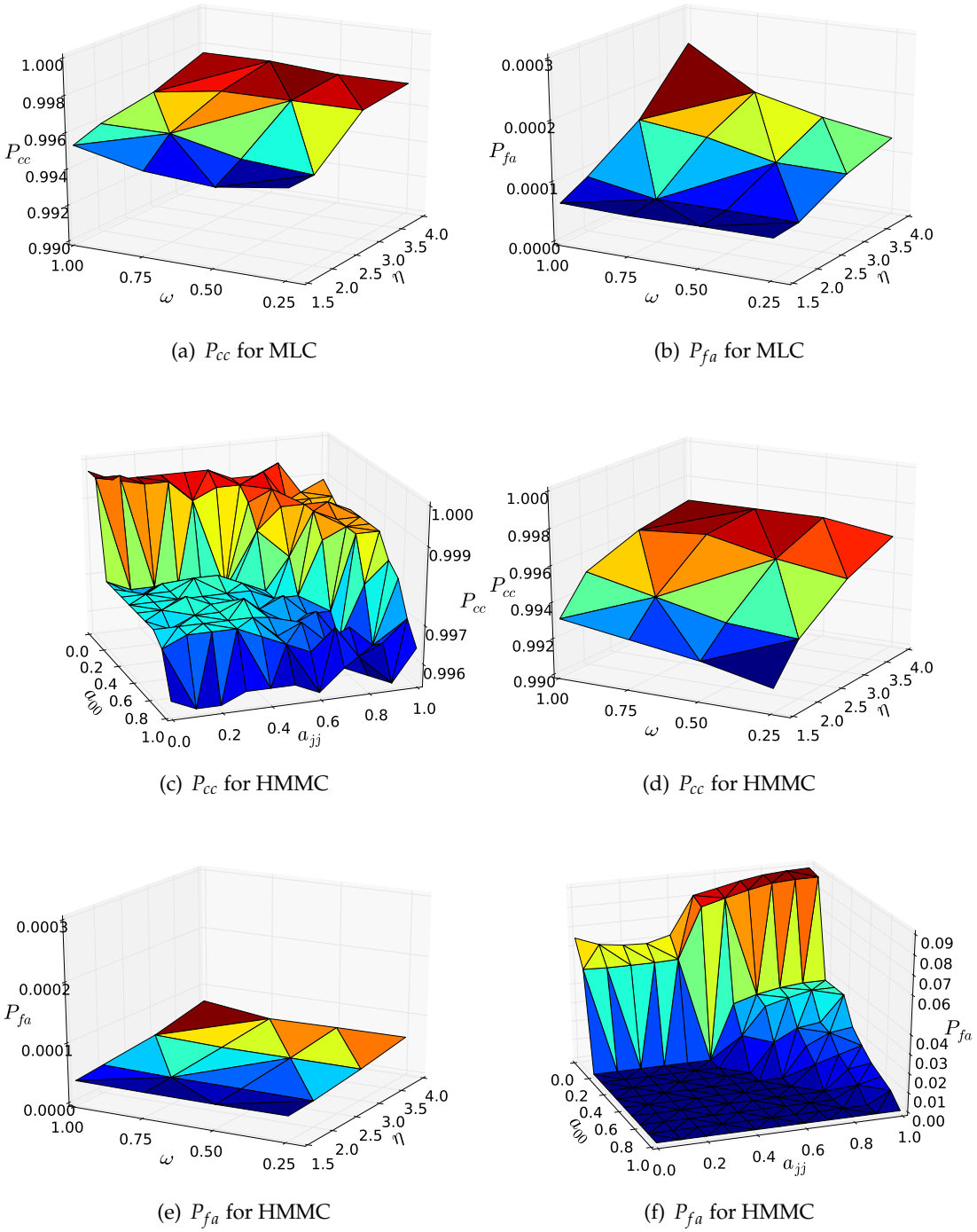

(a) P_{cc} for MLC

(b) P_{fa} for MLC

(c) P_{cc} for HMMC

(d) P_{cc} for HMMC

(e) P_{fa} for HMMC

(f) P_{fa} for HMMC

Figure 5.7. Effect of link line obstruction model parameters on MLC and HMMC (a)-(d); and one-step transition probabilities on HMMC performance (e)-(f).

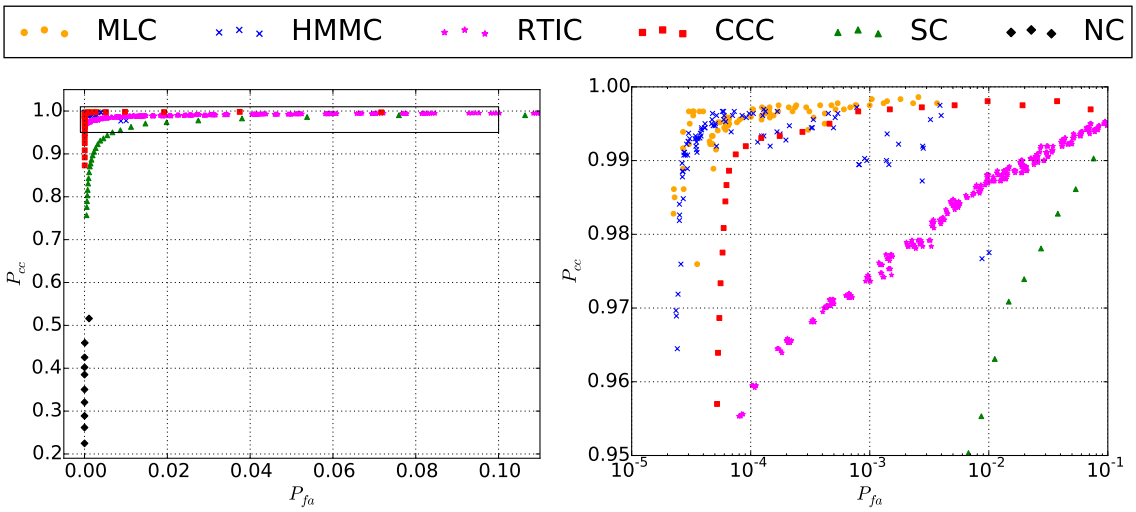

Figure 5.8. (left) ROC curves for six classifiers. Inset box in top left. (right) Inset of the ROC curve.

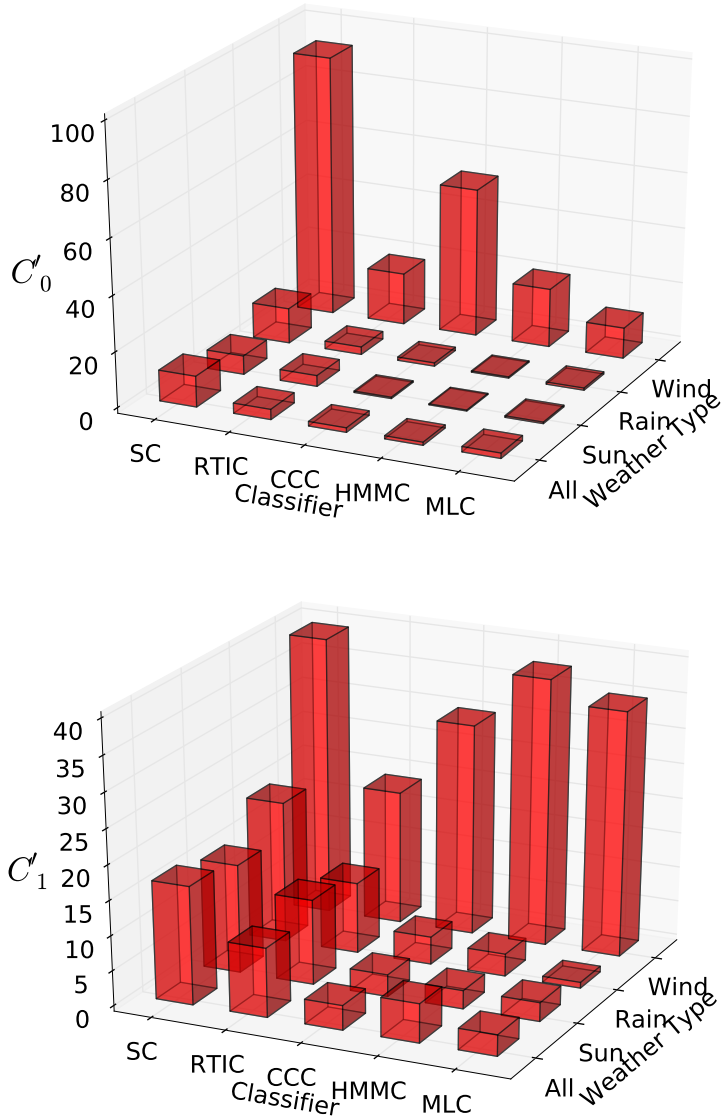

Figure 5.9. (top) C'_0: parameters optimized to minimize false alarms. (bottom) C'_1: parameters optimized to minimize misclassifications.

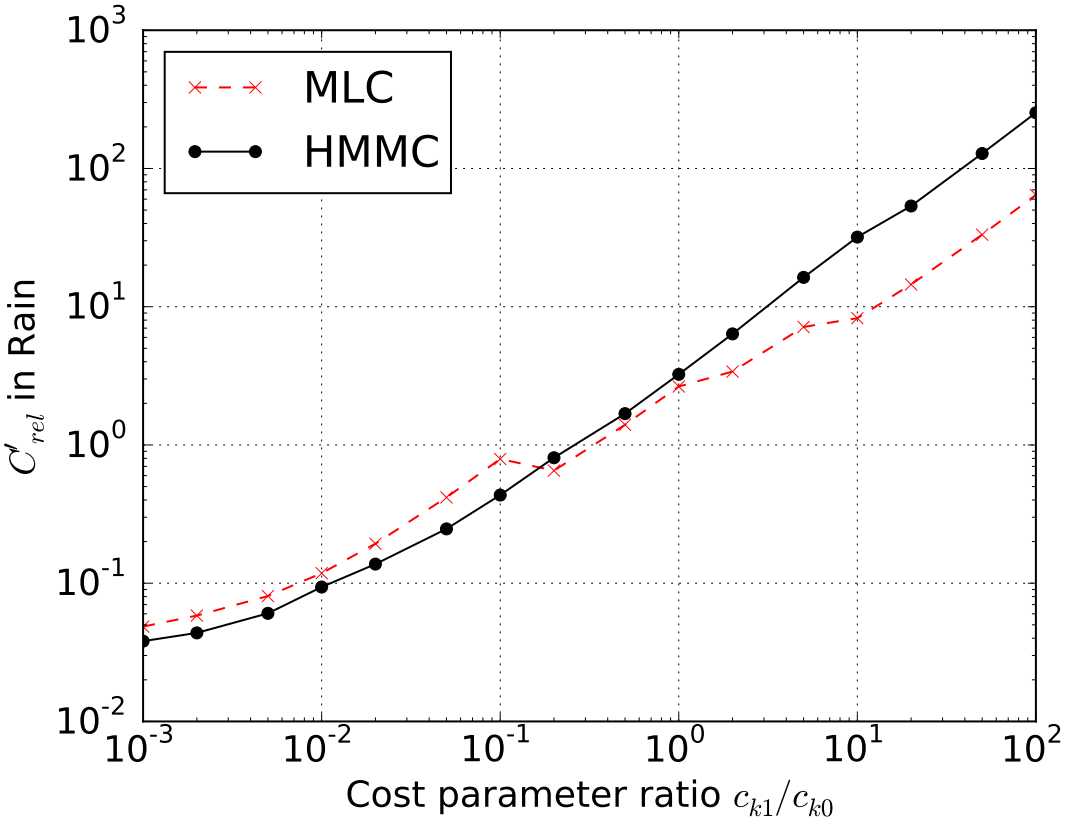

Figure 5.10. C'_{rel} for both the MLC and HMMC using the rain weather data sets.

Table 5.1. Classifier Performance for Fixed P_{cc} or P_{fa}.

	P_{fa} for fixed $P_{cc} = 0.995$	$1 - P_{cc}$ for fixed $P_{fa} = 5.0 \times 10^{-5}$
MLC	3.05×10^{-5}	3.33×10^{-3}
HMMC	4.11×10^{-5}	3.61×10^{-3}
CCC	4.58×10^{-4}	5.80×10^{-2}
RTIC	7.10×10^{-2}	9.16×10^{-2}
SC	2.04×10^{-1}	$> 2.50 \times 10^{-1}$

Table 5.2. Perf. vs. Channels for Fixed $P_{fa} = 2.5 \times 10^{-5}$.

	MLC	HMMC
1 channel $1 - P_{cc}$	1.37×10^{-2}	2.80×10^{-2}
4 channel $1 - P_{cc}$	$< 1.11 \times 10^{-3}$	$< 1.11 \times 10^{-3}$

Table 5.3. Numeric Cost Values.

	C_0'			C_1'		
	All	Sun	Rain	All	Sun	Rain
MLC	1.93	0.56	0.79	3.04	2.69	0.83
HMMC	1.11	0.34	0.43	5.59	2.63	3.19
CCC	1.62	0.50	1.18	3.52	3.12	3.96

5.9 References

[1] M. Thomas, "Over 35,000kg mangoes stolen from orchards - the times of india," 2015. [Online]. Available: http://timesofindia.indiatimes.com/city/surat/Over-35000kg-mangoes-stolen-from-orchards/articleshow/47573009.cms

[2] J. Wilson and N. Patwari, "Radio tomographic imaging with wireless networks," *IEEE Trans. on Mobile Computing*, vol. 9, no. 5, pp. 621–632, May 2010.

[3] K. Woyach, D. Puccinelli, and M. Haenggi, "Sensorless sensing in wireless networks: Implementation and measurements," in *2006 4th Int. Symp. on Modeling and Optimization in Mobile, Ad Hoc and Wireless Networks*, 2006.

[4] M. Youssef, M. Mah, and A. Agrawala, "Challenges: device-free passive localization for wireless environments," in *Proc. of the 13th Annu. ACM Int. Conf. on Mobile Computing and Networking*. ACM, 2007, pp. 222–229.

[5] R. Beckhusen, "Homeland security delays plan to place sensors on u.s.-mexico border," 2013. [Online]. Available: http://www.wired.com/2013/02/border-sensors/

[6] P. Hillyard, N. Patwari, S. Daruki, and S. Venkatasubramanian, "You're crossing the line: localizing border crossings using wireless rf links," *IEEE Signal Process. and SP Educ. Workshop (SPW-2015)*, 2015.

[7] M. H. Hashim and S. Stavrou, "Measurements and modelling of wind influence on radiowave propagation through vegetation," *IEEE Trans. Wireless Commun.*, 2006.

[8] K. Bannister, G. Giorgetti, and S. K. Gupta, "Wireless sensor networking for hot applications: Effects of temperature on signal strength, data collection and localization," in *Proc. of the 5th Workshop on Embedded Networked Sensors (HotEmNets 08)*. Citeseer, 2008.

[9] J. Thelen, D. Goense, and K. Langendoen, "Radio wave propagation in potato fields," in *1st Workshop on Wireless Network Measurements*, vol. 2, 2005, pp. 331–338.

[10] P. Hillyard, "Border crossing data," 2016. [Online]. Available: https://sites.google.com/site/peterhillyard/home/border-crossing-data

[11] O. Kaltiokallio, M. Bocca, and N. Patwari, "A fade level-based spatial model for radio tomographic imaging," *IEEE Trans. Mobile Computing*, vol. 13, no. 6, pp. 1159–1172, 2014.

[12] Y. Zheng and A. Men, "Through-wall tracking with radio tomography networks using foreground detection," *IEEE Wireless Commun. Networking Conf. WCNC*, pp. 3278–3283, 2012.

[13] J. Wilson and N. Patwari, "A Fade-level skew-Laplace signal strength model for device-free localization with wireless networks," *IEEE Trans. Mobile Computing*, vol. 11, no. 6, pp. 947–958, 2012.

[14] H. Hashemi, "A study of temporal and spatial variations of the indoor radio propagation channel," in *PIMRC-94*, vol. 1, Sep 1994, pp. 127–134.

[15] L. Rabiner, "A tutorial on hidden Markov models and selected applications in speech recognition," *Proc. IEEE*, vol. 77, no. 2, pp. 257–286, 1989.

[16] L. E. Baum, J. A. Eagon *et al.*, "An inequality with applications to statistical estimation for probabilistic functions of markov processes and to a model for ecology," *Bull. Amer. Math. Soc.*, vol. 73, no. 3, pp. 360–363, 1967.

[17] M. G. Pelletier, S. Karthikeyan, T. R. Green, R. C. Schwartz, J. D. Wanjura, and G. A. Holt, "Soil moisture sensing via swept frequency based microwave sensors," *Sensors*, vol. 12, no. 1, pp. 753–767, 2012.

[18] M. Seifeldin, A. Saeed, A. E. Kosba, A. El-Keyi, and M. Youssef, "Nuzzer: A large-scale device-free passive localization system for wireless environments," *IEEE Trans. on Mobile Computing*, vol. 12, no. 7, pp. 1321–1334, 2013.

[19] D. Molloy, "Beaglebone: Video capture and image processing on embedded linux using opencv," 2015. [Online]. Available: http://www.youtube.com/watch?v=8QouvYMfmQo

[20] S. Kumar, T. H. Lai, and A. Arora, "Barrier coverage with wireless sensors," in *Proc. of the 11th Annu. Int. Conf. on Mobile Computing and Networking*, ser. MobiCom '05. New York, NY, USA: ACM, 2005, pp. 284–298.

[21] T. Yang, D. Mu, W. Hu, and H. Zhang, "Energy-efficient border intrusion detection using wireless sensors network," *EURASIP J. on Wireless Commun. and Networking*, vol. 2014, no. 1, 2014.

[22] Z. Sun, P. Wang, M. C. Vuran, M. A. Al-Rodhaan, A. M. Al-Dhelaan, and I. F. Akyildiz, "Bordersense: Border patrol through advanced wireless sensor networks," *Ad Hoc Networks*, vol. 9, no. 3, pp. 468 – 477, 2011.

[23] X. Li, Q. Sun, J. Wo, M. Zhang, and D. Liu, "Hybrid TDM/WDM-based fiber-optic sensor network for perimeter intrusion detection," *J. of Lightwave Technology*, vol. 30, no. 8, pp. 1113–1120, April 2012.

[24] D. Tahmoush and J. Silvious, "Remote detection of humans and animals," in *2009 IEEEApplied Imagery Pattern Recognition Workshop (AIPRW)*, Oct 2009, pp. 1–8.

[25] R. Lane and S. Hayward, "Detecting personnel in wooded areas using mimo radar," in *2007 IET Int. Conf. on Radar Sys.*, Oct 2007, pp. 1–5.

[26] M. Chishti and C. Bergeron, "Virtual border fence given mixed assessment in first test," *Washington, DC: Migration Policy Institute*, 2008.

[27] A. Arora, P. Dutta, S. Bapat, V. Kulathumani, H. Zhang, V. Naik, V. Mittal, H. Cao, M. Demirbas, M. Gouda, Y. Choi, T. Herman, S. Kulkarni, U. Arumugam, M. Nesterenko, A. Vora, and M. Miyashita, "A line in the sand: A wireless sensor network for target detection, classification, and tracking," *Computer Networking*, vol. 46, no. 5, pp. 605–634, Dec. 2004.

[28] B. Krawczeniuk, "Carney focuses on illegal immigration," 2008. [Online]. Available: http://bit.ly/1nwEt2v

CHAPTER 6

FOCUSING THROUGH WALLS: AN E-SHAPED PATCH ANTENNA IMPROVES WHOLE-HOME RADIO TOMOGRAPHY

6.1 Abstract

Tagless identification and tracking with through-wall received signal strength-based radio tomographic imaging (RTI) allows emergency responders to learn where people are inside of a building before entering the building. Use of directional antennas in RTI nodes focuses RF power along the link line, improving system performance. However, antennas placed on a building's exterior wall can be detuned by their close proximity to the dielectric, thus sending power across wider angles and resulting in less accurate imaging. In this paper, we improve through-wall RTI by using an E-shaped patch antenna we design to be mounted to an exterior wall. Along with its directionality, the E-shaped patch antenna is designed to avoid impedance mismatches when brought into close proximity of a dielectric material, thus increasing radiation through the exterior wall and along the link line. From our experiments, we demonstrate that the E-shaped patch antenna can reduce the median root mean square localization error by up to 43% when compared to microstrip patch and omnidirectional antennas. For equal error performance, the E-shaped patch antenna allows an RTI system to reduce power and bandwidth usage by using fewer nodes and measuring on fewer channels.

6.2 Introduction

First responders, security personnel, and tactical forces can operate with increased safety when they know where people are located in a building prior to entering the building. RF sensing has been a popular choice for localizing people through walls because of its ability to sense moving people through non-metallic obstructions, through smoke, in any lighting condition, and *without tags* [1]–[4]. Prior research has shown how radio tomographic imaging (RTI) provides a low power and low cost-per-unit solution for imaging motion through walls and buildings and thus locate people inside [1], [5], [6]. To use RTI in security scenarios, first responders deploy nodes around the perimeter of the building. Facilitating rapid (and thus safer) deployment of the nodes is of great importance. For example, a requirement for SWAT use of an RTI system is that the system is easily deployable to keep first responders safe [7]. We propose attaching nodes to the exterior wall as a means of making the system easily deployable. We envision first responders launching or opportunistically placing nodes directly on the exterior walls of a building. After the nodes are attached to the walls, the nodes record pairwise received signal strength (RSS) measurements, and an image map is estimated of the motion inside of the building.

There are particular challenges with RTI for through-wall imaging in these tactical scenarios. First, multipath fading does not always match the assumed spatial model. RTI is based on the assumption that changes in RSS on a link are due to the presence of a person on the *link line*, the imaginary line segment that connects the two nodes. If most of the power does not travel along the link line, then the person's presence on the link line does not have a strong impact on the RSS, thus degrading the accuracy of RTI. A second challenge is that, with nodes attached to a wall and their antenna main lobe directed through the wall, the antenna impedance can be detuned. The antenna's center frequency can shift and its radiation pattern can be altered. A detuned antenna results in high attenuation of the multipath components which travel along the link line. RTI's localization performance, in turn, is negatively affected by the model mismatch.

In this paper, we propose addressing these two challenges and improving localization performance of RTI by equipping nodes with an E-shaped patch antenna we specifically develop to be attached to an exterior building wall [8]. Our E-shaped patch antenna is a directional antenna that focuses most of its power through the wall to which it is attached

and thereby amplifies multipath on or near the link line and attenuates those far from the link line.

Prior research has addressed the use of directional antennas for RTI [5], [6]. In particular, [5] used directional antennas for through-wall RTI, but localization accuracy results, in comparison to omnidirectional antennas, were mixed. We address this counter-intuitive result by showing that the classical microstrip patch antenna used in [5] is detuned when placed against common building materials. Our E-shaped patch antenna naturally has a wider operating bandwidth such that it is not strongly negatively affected when it is brought into close proximity to a dielectric material [9].

In experiments we perform, we compare the performance of our E-shaped patch antenna against both omnidirectional antennas and microstrip patch antennas at two different houses, one made of brick and the other of fiber cement siding. Both materials are known to have high RF losses, and thus through-wall localization should be particularly challenging. Using moving average-based and variance-based RTI [1], we show that the E-shaped patch antennas reduce the median root mean squared error (RMSE) by up to 43% compared to the omnidirectional and microstrip patch antennas. Alternatively, we demonstrate that we can deploy fewer nodes and measure fewer channels, and thus use less power and bandwidth, with the E-shaped patch antenna and achieve the same or lower median RMSE compared to the omnidirectional and microstrip patch antennas.

The remainder of this paper is organized as follows. In Section 6.4, we describe the design and characteristics of the E-shaped patch antenna. We then describe in Section 6.5 the two variations of RTI we use to test the influence of antenna type on localization performance. In Section 6.6, we describe the two test locations and the experiments performed at those locations. We finish this paper by showing and evaluating the results of those experiments in Section 6.7.

6.3 Related Work

Being able to localize a person has opened many new technological advances. With RF tag-based localization, for example, a person wears or carries an RF tag or radio which can be localized with time of flight or signal strength measurements [10]. However, there are cases where localization is needed but a person or object may not have an RF tag.

Device-free localization (DFL) [11], passive localization [12], or sensorless sensing [13] all describe the method of using wireless sensor networks to localize people without RF tags. Our work fits into this method type.

DFL is well-suited for security and first-response scenarios where entering a building can be life-threatening. Wireless RF devices are placed around the exterior of a building to "see" people inside. Ultra-wideband radars, for example, have been used to image the reflections a person creates from high-frequency pulses [2]–[4]. DFL is complementary to radar in that we image the location of a person, however, we form the image based on loss in received power (RSS) measured between many pairwise RF nodes which are deployed around the exterior of the building. One advantage of devices used for DFL is that the sensor signal power decays with distance d as $1/d^2$ as opposed to $1/d^4$ for radar. This means that to increase the sensing range for radars, the transmit power for radar must be increased dramatically more than devices used for DFL. This is a important design criteria for larger buildings with potentially many obstructions inside.

Many types of DFL have been proposed to perform through-wall localization including fingerprint-based methods [14], [15], particle filters [16], [17], and radio tomographic imaging (RTI) [18], [19]. Of these methods, RTI requires the least calibration and is computationally efficient. In our work, we explore the idea of using specially-made antennas that are attached to a wall to improve the localization accuracy of RTI. Prior research has addressed the use of directional antennas for RTI [5], [6]. In particular, [5] used directional antennas for through-wall RTI, but localization accuracy results, in comparison to omnidirectional antennas, were mixed. Our work expands upon these prior works by creating an antenna that does not become detuned when placed against an exterior wall. We show how our antenna improves the localization performance of RTI-based methods.

6.4 Antenna Comparison

When placed in close proximity with a dielectric material, an antenna with narrow bandwidth will have an impedance mismatch because of impedance detuning. This detuning results in a shift in the center frequency and losses in efficiency at the desired frequency. In contrast, the E-shaped patch antenna, as presented in [9], has several properties that make it an excellent fit for applications where the antenna is attached to the surface of

an exterior wall. It is designed to maintain a wide bandwidth and reduce impedance mismatches. The E-shaped patch antenna is also designed to have a 75° horizontal half-power beamwidth and 80° vertical half-power beamwidth. This size of beam, when placed against an exterior wall, will direct most of the RF power into the building.

The E-shaped patch antenna is derived from a microstrip patch antenna which behaves like a cavity resonator, or equivalently, an LC resonant circuit. The outline of the E-shaped patch antenna is $L1$ by $W1$, with a feed point at $(W1/2, Lp)$, as shown in Figure 6.1(a). The primary design feature of the E-shaped patch antenna is to introduce a secondary resonance by placing two identical slots with a length Ls and a width Ws into the microstrip patch antenna [8]. The slots are symmetrical on the feed point with distance Ds. We simulate and optimize the E-shaped patch antenna on an FR-4 dielectric with a relative permittivity of 3.66, a loss tangent of 0.0127 at 2.4 GHz, and thickness of 3.2mm (two layers of a 1.6mm thick substrates), using ANSYS HFSS software. The antenna is targeted to be 50 Ohm. Figure 6.1(b) shows the E-shaped patch antenna fabricated on the same substrate with that in the simulation.

In this paper, we compare our E-shaped patch antenna to a commercially-available circular polarized microstrip patch antenna [20] and monopole antenna both of which are tuned to 2.4 GHz. These antennas are shown in Figure 6.2. We present experimental values for the reflection coefficient of the E-shaped patch antenna, microstrip patch antenna, and omnidirectional antenna when in free space and when placed against a brick and cement board. The dielectric constant of the brick approximates to 3.58, and cement has a dielectric constant around 4.5. We show an example of our setup in Figure 6.2. The reflection coefficient of the E-shaped patch antenna at 2.4 GHz, shown in Figure 6.3, remains less than -10 dB for all materials, while that of the microstrip patch antenna, shown in Figure 6.3, exceeds -10 dB after detuning caused by the brick and cement board. Hence, the wideband E-shaped patch antenna is more robust in terms of reflection coefficient when placed upon various materials than the microstrip patch antenna. Figure 6.3 also shows that the reflection coefficient of omnidirectional antenna remains less than -10 dB when attached to the brick but exceeds -10 dB after being detuned by the cement board.

We make some additional observations from Figure 6.3. We first note that the microstrip patch antenna appears to have been tuned for 2.3 instead of 2.4 GHz. Since these

are commercially available antennas, we had little control over their tuning. However, we note that all antennas have a return loss of -10 dB or lower at 2.4 GHz in freespace, meaning they are all at least 90% efficient in the operating frequency. In context of this paper, one of the most important observations is the detuning that occurs when the antenna is placed against the material. The omnidirectional and microstrip patch antenna are most negatively effected, whereas the E-shaped patch antenna improves. These improvements, though small in terms of efficiency, add up in big ways when evaluating antenna gains.

Figure 6.4 presents the measured H-plane dB radiation patterns of the E-shaped patch, microstrip patch, and omnidirectional antenna in free space and attached to brick and cement board. Measurements were made with an open-air rooftop range using a network analyzer and a reference E-shape patch antenna. The E-shaped patch antenna has higher gain in free space than the ordinary microstrip patch antenna and omnidirectional antenna at 2.4 GHz. When attached to either the brick or cement board, the E-shaped patch antenna achieves higher directivity than the microstrip patch antenna and omnidirectional antenna. When attached to brick, the radiation pattern of the microstrip patch antenna degrades severely, while the E-shaped patch antenna maintains a similar radiation pattern as measured in free space. Furthermore, because free space has a higher impedance than that of brick and cement board, the omnidirectional antenna radiates more power into the materials than it does into free space. Therefore, omnidirectional antenna has higher gain than the microstrip patch antenna when attached to the materials.

6.5 Radio Tomographic Imaging

In this section, we describe two algorithms for RTI that we use to compare localization performance when using different antennas.

The purpose of RTI is to create an image of an area of interest in order to locate an object or person inside. To that end, we deploy N nodes around the exterior periphery of a building. The nodes take turns transmitting a packet in a TDMA fashion. After all nodes have transmitted, each node has measured the RSS from all other nodes. We denote the RSS measured on link $l = (i, j, c)$ formed by transmitting node i and receiving node j on channel c as r_l. As a person moves inside the area of interest, new multipath are created while others are changed in phase and magnitude, which cause changes in r_l. We use a

history of r_l to compute a link statistic y_l which quantifies the RSS change on link l. The link statistic from each link is sent to RTI to estimate an discretized image of where motion is observed. We describe two ways of computing link statistics in Section 6.5.1. First, we describe how the image is estimated.

In RTI, we want to estimate an $M \times 1$ image $\mathbf{x}$ from the link statistics stored in the $L \times 1$ vector $\mathbf{y} = [y_1, y_2, \ldots, y_L]^T$, where L is the number of links. The relationship between $\mathbf{y}$ and $\mathbf{x}$ has historically been modeled as the linear relationship

$$\mathbf{y} = \mathbf{A}\mathbf{x} + \mathbf{n} \tag{6.1}$$

where $\mathbf{A}$ is $L \times M$ and $\mathbf{n}$ is a $L \times 1$ noise vector. The (l, k) element of $\mathbf{A}$, $A_{l,k}$, quantifies the influence of pixel k on the link statistic for link l. We set $A_{l,k} = 1/p_l$ if $d^i_{l,k} + d^j_{l,k} < d_l + \lambda$ and zero otherwise, where $d^n_{l,k}$ is the distance from node n of link l to pixel k, d_l is the distance between the transmitting and receiving node of link l, λ is the ellipse width, and p_l is the number of pixels inside the link l ellipse.

Estimating the image $\mathbf{x}$ is an ill-posed problem. To address this issue, we use the regularized least-squares solution, which constrains the estimated image to be smooth [21]. The result of RTI is an image $\hat{\mathbf{x}}$. We choose the center coordinate of the pixel with the greatest value in $\hat{\mathbf{x}}$ to be the estimated location of the person. We show an image generated by RTI during one of the experiments in Figure 6.5.

6.5.1 Link Statistics

An essential part of RTI is the computation of the link statistics vector $\mathbf{y}$. The elements of the vector represent that amount of change that has occurred in the RSS for each link. Some research has used the difference between the current RSS and the average RSS during an empty-room calibration period to compute the link statistics [18]. However, in emergency applications, it is unlikely we will have the opportunity to measure an empty-room average RSS. We alternatively describe two methods to compute link statistics by using a history of RSS measurements to quantify which links' RSS have recently changed. Although we avoid requiring an empty-room calibration, we note that these two methods cannot image people who are completely stationary.

The first method, which we call moving average-based RTI (MARTI), computes the absolute relative fractional change between a long and short term average RSS. In MARTI,

we compute the link statistic for link l by first adding r_l into both a short and long term buffer where the length of the short and long term buffer can be tuned. We denote the average of the short term buffer as α_l and the average of the long term buffer as β_l. When a new r_l is measured, we compute the link statistic $y_l = |(\beta_l - \alpha_l)/\beta_l|$ [11].

The second method uses variance-based RTI (VRTI) [1] to compute the sample variance of a short buffer of RSS values. The length of the buffer can be tuned for optimal performance. When a new RSS measurement comes in for r_l, we add it to the buffer and let y_l equal the sample variance of the buffer.

6.6 Experimentation

To evaluate the performance of the proposed E-shaped patch antenna design, we perform a series of experiments at two different houses. In this section, we describe the hardware, the pertinent information about the houses, and the test procedures we use to collect data used in post-processing.

6.6.1 Equipment

The wireless nodes deployed in the experiments use a Texas Instruments CC2530 radio module with an SMA interface to connect the antennas. We program twenty nodes to use a token passing protocol in a TDMA fashion to operate on four different channels in the 2.4 GHz ISM band. We package the nodes and antennas into sealed containers as shown in Figure 6.6 and attach the container to the exterior walls so that the antennas' main lobe are directed into the house. We use our fabricated E-shaped patch antennas, microstrip patch antennas, and omnidirectional antennas. The nodes begin the communication protocol and an extra node is used to overhear the transmissions and save to file the measured RSS from each node. We note that a real-time implementation of RTI is possible, but post-processing is used in this paper for data analysis.

6.6.2 Experiment Locations

We compare the performance of the antenna types at two different locations. The first house is a 875 square foot home whose exterior walls are made of brick. The home was fully furnished with beds, dressers, a kitchen table, a couch and two armchairs. The second house is a 1277 square foot home whose exterior walls are made of fiber cement siding

which is a mixture of cement, sand and fibers. This house is also fully furnished. The two types of exterior walls gives us a way to demonstrate the E-shaped patch antenna's ability to keep its impedance tuned in the presence of different building materials. We choose these materials because of the houses' availability, however, we know from our testing that brick and cement board induce large losses in antenna gain and thus these are particularly challenging scenarios. The exterior walls of these two houses and the locations of the nodes are shown in Figure 6.7.

6.6.3 Experiment Procedures

At each house, one experiment consists of a person walking inside at predefined locations at predefined times so that we know the ground truth location. When a new set of RSS measurements from each link is recorded, we compute the current link statistic vector $\mathbf{y}$ using both MARTI and VRTI, and estimate the current location from $\hat{\mathbf{x}}$. We denote the current estimated location coordinates at sample time n as $\hat{\mathbf{w}}(n)$ and the true location coordinates as $\mathbf{w}(n)$. The RMSE is computed as

$$RMSE = \left[\frac{1}{E_{len}} \sum_{n=1}^{E_{len}} \|\hat{\mathbf{w}}(n) - \mathbf{w}(n)\|^2 \right]^{1/2} \tag{6.2}$$

where E_{len} is the number of link statistic vectors $\mathbf{y}$ computed during the experiment. At each house, three individuals perform two experiments each while the E-shaped patch antenna is installed. In the same fashion, we perform two more sets of six experiments, one for the microstrip patch antenna and another for the omnidirectional antenna. The time duration of each experiment is 3.5 minutes and so in total, we collect over 2 hours of RSS measurements which we make publicly available at [22].

6.7 Results

In this section, we report the localization performance of each antenna type from our brick and cement board experiment sites. In addition, we show the localization performance of each antenna type as a function of the number of nodes deployed and the number of channels measured.

6.7.1 Overall Localization Performance

To compare the localization performance of each antenna, we take the median of the RMSE achieved over all six experiments that were performed using one antenna type. For reference, the minimum achievable median RMSE is 0.3 feet in the brick house and 0.35 feet in the cement board house using a 1 foot squared pixel. We show the median RMSE for the RTI methods in Figure 6.8. We observe that the E-shaped patch antenna achieves a lower median RMSE than the other antennas using MARTI and VRTI in both the brick house and the cement board house. We show in Table 6.1 the percent decrease in median RMSE when comparing the E-shaped patch antenna to the omnidirectional and microstrip patch antenna. The E-shaped patch antenna reduces the median RMSE by more than 20% using either RTI method in the brick house with the microstrip patch antenna. The localization gains are more pronounced in the cement board house. The median RMSE, when using MARTI and the E-shaped patch, reduces by 37% compared to the omnidirectional antenna and 43% compared to the microstrip patch antenna.

We note that when we use MARTI in the brick house, the omnidirectional antenna performs almost as well as the E-shaped patch antenna. But this is not too surprising of a result since the size of the material and the dielectric properties can often work against one another to inadvertently make a resonance at the desired frequency of operation. We would expect a narrowband antenna to occasionally achieve a low median RMSE over a range of construction types and materials. But the E-shaped patch antenna is uniquely designed to capture a wide range of geometries and dielectric properties.

We also observe from Figure 6.8 that the median RMSE achieved by the E-shaped patch antenna in the brick and cement house using either RTI method has a maximum difference of only 0.5 feet. In contrast, the difference for the omnidirectional antenna is 1.7 feet and 1.6 feet for the microstrip patch antenna. We see the E-shaped patch antenna makes through-wall RTI localization more robust across house size and building material compared to the omnidirectional and microstrip patch antenna.

The results shown in Figure 6.8 are well explained by the measured reflection coefficient and radiation patterns shown in Figures 6.3 and 6.4. We observe that the microstrip patch antenna's center frequency shifts away from 2.4 GHz after becoming detuned when it is placed against either brick or cement board. As a result, its median RMSE suffers the

worst of all the antennas. One other interesting result is the lower median RMSE in the brick house compared to the cement house for all antenna types. Two factors that support our experimental results is that the reflection coefficients at 2.4 GHz for the antennas are lower in the brick house than the cement board house and that the brick house has a smaller footprint than cement board house. These results suggest that the size of the area being monitored and the building material both play a role in localization accuracy.

6.7.2 Localization Performance vs. Nodes Deployed

Although we deploy twenty nodes in our experiments, we wish to show how the median RMSE is affected when we deploy fewer nodes. To do this, we iterate through all combinations of $\binom{20}{a}$ nodes for $a \in \{16, 17, 18, 19, 20\}$ and compute the median RMSE over all iterations for a. We show the results in Figure 6.9. From Figure 6.9, we observe that the E-shaped patch antenna outperforms the other antenna types for any number of nodes deployed, for both RTI methods, and for both building materials. We also observe that, for all antenna types and building material, VRTI outperforms MARTI as the number of nodes decreases. The figure also shows that the percent increase of the median RMSE for using MARTI over VRTI at the brick house and using sixteen nodes is 31% for the mcirostrip patch antenna, 25% for the omnidirectional antenna, and 10% for the E-shaped patch antenna. If we instead use the cement house, the percent increase changes to 10% for the mcirostrip patch antenna, 13% for the omnidirectional antenna, and 13% for the E-shaped patch antenna. Our experimental results suggests that the percent increase in median RMSE with the E-shaped patch antenna is much less dependent on building material and RTI method than it is for the microstrip patch and omnidirectional antenna.

Another interesting result is that at the cement board house, the E-shaped patch antenna achieves the same median RMSE using sixteen nodes with VRTI and seventeen nodes with MARTI as the patch and omnidirectional antenna achieves with twenty nodes using either RTI method. Despite the cement board house's large footprint and the decreased number of nodes, the E-shaped patch antenna is still able to achieve similar or better localization performance than the other two antennas. Thus, we can use fewer nodes and consume less power by using the E-shaped patch antenna and still localize as well or better than when we use an omnidirectional or microstrip patch antenna.

6.7.3 Localization Performance vs. Channels Used

In our experiments, we program our nodes to measure on four channels in the 2.4 GHz band. But we are interested in how the median RMSE is influenced by the number of channels used. To do this, we iterate through all combinations of $\binom{4}{C}$ channels for $C \in \{1, 2, 3, 4\}$ and compute the median RMSE over all iterations for C. We show the results in Figure 6.10. We observe that in all cases, the E-shaped patch antenna achieves a lower median RMSE than the omnidirectional and microstrip patch antenna. And in general, MARTI is a more robust localization method than VRTI when we measure RSS on fewer channels.

In the cement board house, we find that the we can measure on just one channel with the E-shaped patch and outperform the omnidirectional and microstrip patch antenna by 0.75 feet to 1.75 feet depending on the RTI method. In an application that is power-limited, the E-shaped patch antenna can achieve a lower RMSE but save power and bandwidth by only measuring on one channel. These power savings can also be seen if we consider both RTI methods and house types and only use the E-shaped patch antenna. We observe that in this case, using two channels instead of four only increases the median RMSE by up to 0.2 feet but reduces the power and bandwidth consumption by half.

6.8 Future Work

There are some interesting ideas that are worth investigating in additional research. The first idea is that when nodes are placed against a wall in security or hostage scenarios, they may not be oriented in the correct way. The E-shaped patch antenna we use in this paper is linearly polarized. We were able to control the orientation of the antennas during the experiments so that polarization was not a concern. But in other cases, the antennas could be inadvertently oriented in a way that does not match the linearly polarization of the antenna, thus incurring losses. A possible solution is to create a circular polarized E-shaped patch antenna where the antennas could be oriented in any way on the exterior wall.

Another point of further investigation is how localization accuracy with RTI is a function of the link budget. We observed in Figures 6.3 and 6.4 that the E-shaped patch antenna suffered the least loss in power when placed against a dielectric material and performed

the best in terms of localization accuracy. To show that localization accuracy is a function of antenna design and not just received signal power, future work can simply reduce the transmit power of the nodes and perform a similar localization comparison of different antenna types.

6.9 Conclusion

In this paper, we presented improvements to through-wall RTI systems using a new E-shaped patch antenna. We designed the E-shaped patch to avoid impedance mismatches when placed in contact with an exterior wall. Avoiding impedance mismatches, along with its directionality, allow the E-shaped patch to radiate its power along the link line and improve localization. When compared to traditional omnidirectional and microstrip patch antennas, the E-shaped patch is more appropriate for use in security and first response scenarios where the antenna needs to be secured to an exterior wall.

We demonstrated that the E-shaped patch antenna reduced the median RMSE by up to 43% compared to a microstrip patch antenna and an omnidirectional antenna at a house made of brick and another made of cement board. The E-shaped patch antenna outperformed the other antennas in two studied RTI methods. We showed that the E-shaped patch antenna achieves a lower localization RMSE even when using fewer nodes and measuring RSS on fewer channels. These performance gains demonstrated that the E-shaped patch antenna can not only reduce localization errors, but it can do so on a tighter power and bandwidth budget. In applications where nodes are attached to the exterior wall of a building, the E-shaped patch can provide superior localization performance compared to other commonly used antennas.

6.10 Acknowledgment

This material is based upon work supported by the National Science Foundation under Grant Nos. #1407949 and #1408464. We would also like to thank Xandem Technology for lending the nodes we used during the experiments. And a special thanks to Charissa Che who provided invaluable editorial feedback.

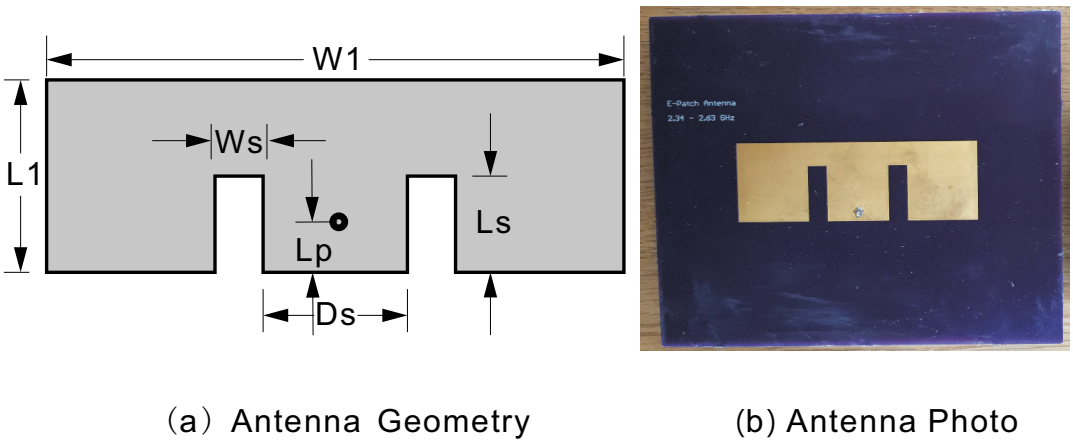

Figure 6.1. (a) Geometry of a wide-band E-shaped patch antenna at $(W1/2, Lp)$ (b) Picture of fabricated E-shaped patch antenna targeted to be 50 Ohm

Figure 6.2. A commercially-available monopole antenna (left) and a microstrip patch antenna (middle) are used to compare against our E-shaped patch antenna in RTI experiments. An example test setup (right) to collect reflection coefficient and radiation pattern data.

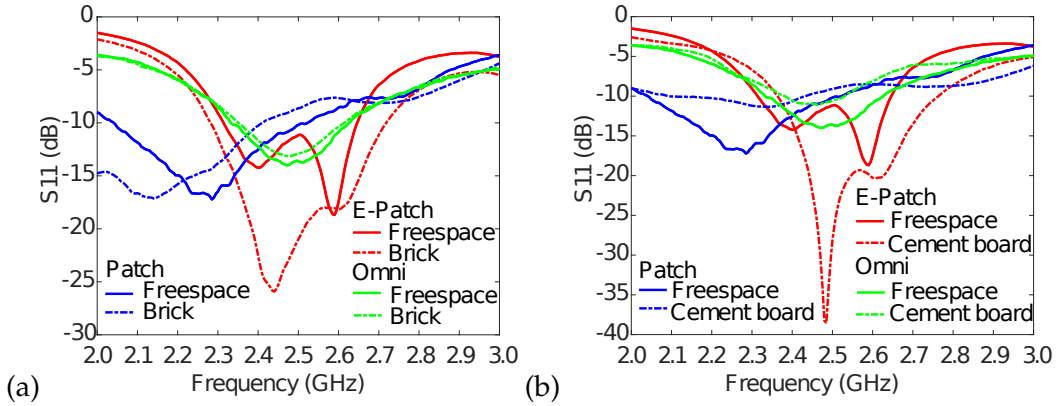

Figure 6.3. Measured reflection coefficients (S11) for the E-shaped patch, the microstrip patch antenna, and the omnidirectional antenna in free space and attached to (a) brick and (b) cement board.

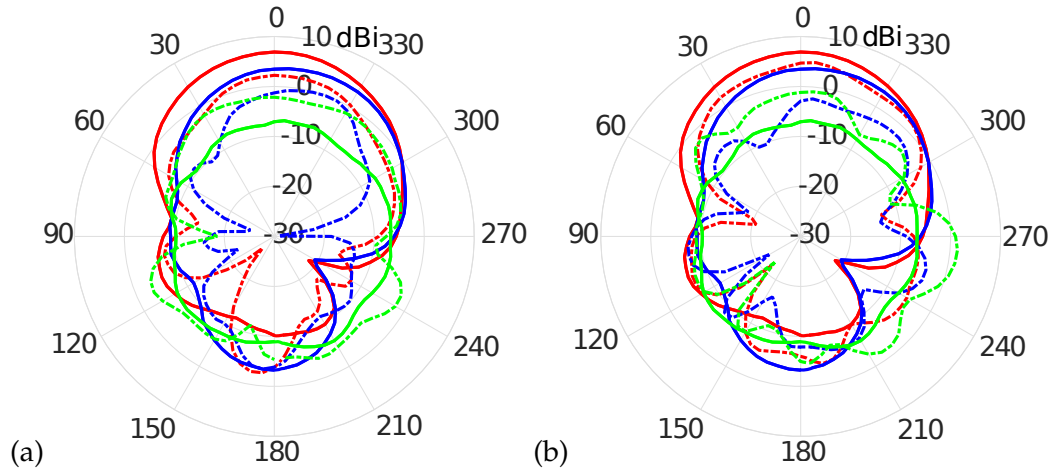

Figure 6.4. Horizontal gain pattern (dB) of the E-shaped patch, the microstrip patch antenna, and the omnidirectional antenna in free space and attached to brick and cement board. Solid lines represent free space and dashed lines represent (a) brick and (b) cement board. The red lines represent E-shaped patch antenna, green lines represent omnidirectional antenna, and blue lines represent microstrip patch antenna.

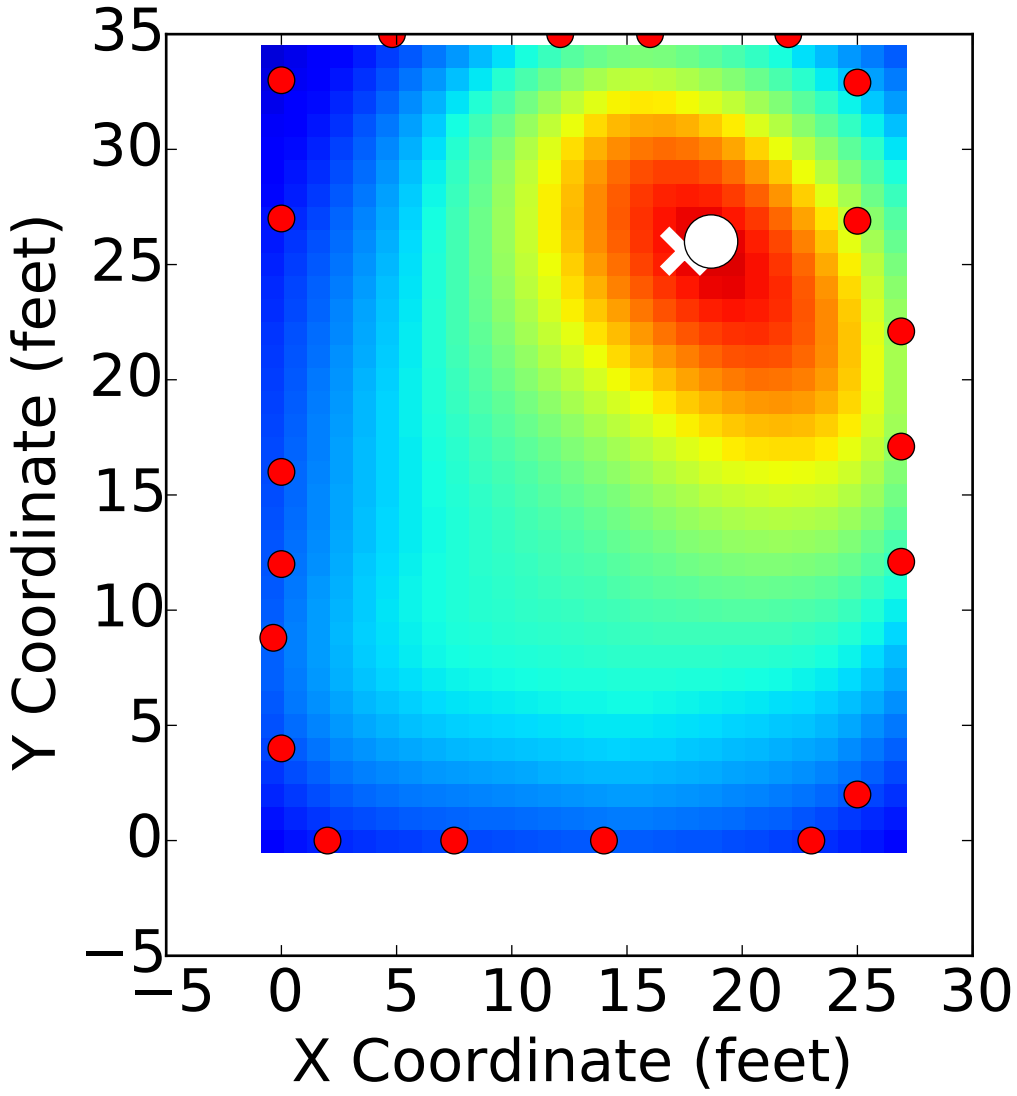

Figure 6.5. An image generated by RTI during one of the experiments. The red circles are the nodes, the white X is true location, and the white circle is the estimated location.

Figure 6.6. The assembled node, antenna, and battery packet in an enclosure. These containers are then attached to the exterior walls with the antennas' main lobe directed inside the house.

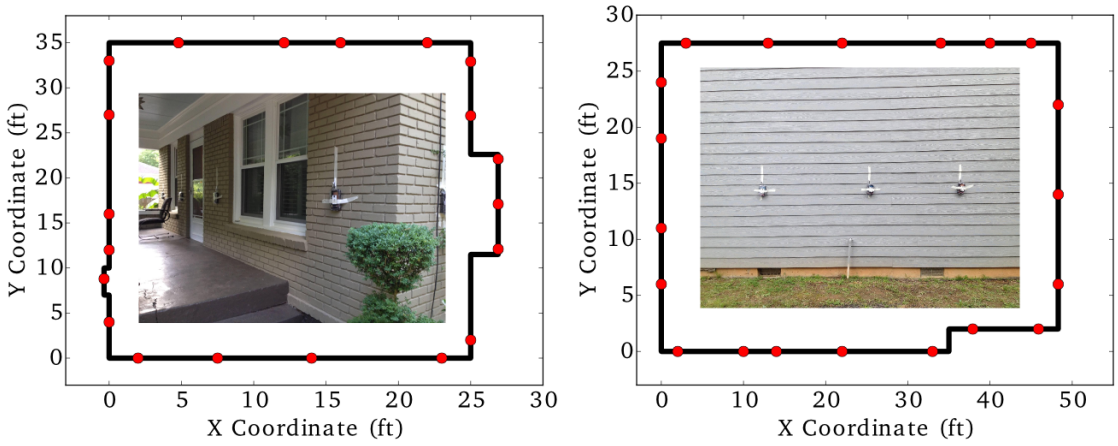

Figure 6.7. Exterior walls and node coordinates with photo inset of (left) brick house and (right) cement board house.

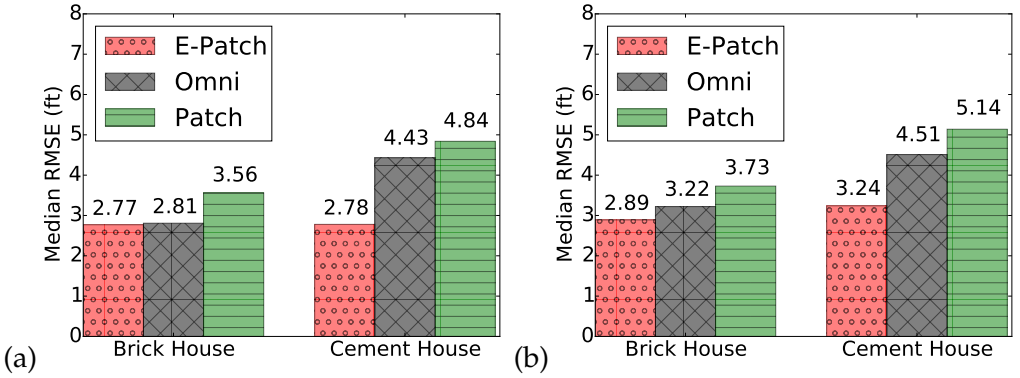

Figure 6.8. Median RMSE achieved for a given antenna and material for (a) MARTI and (b) VRTI.

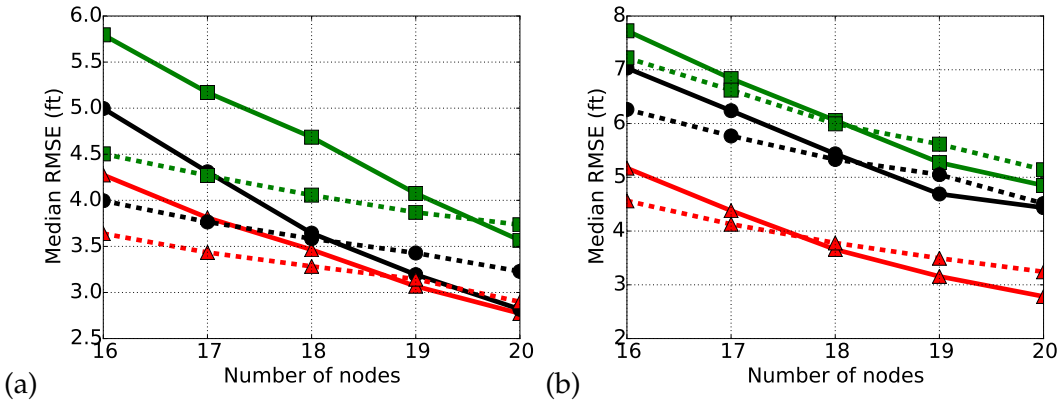

Figure 6.9. Median RMSE achieved as a function of the number of nodes deployed for (a) brick house and (b) cement board house. Solid lines use MARTI while dashed lines use VRTI. The ▲ shows E-shaped patch antenna data points, ● shows omnidirectional antenna data points, and ■ shows microstrip patch antenna data points.

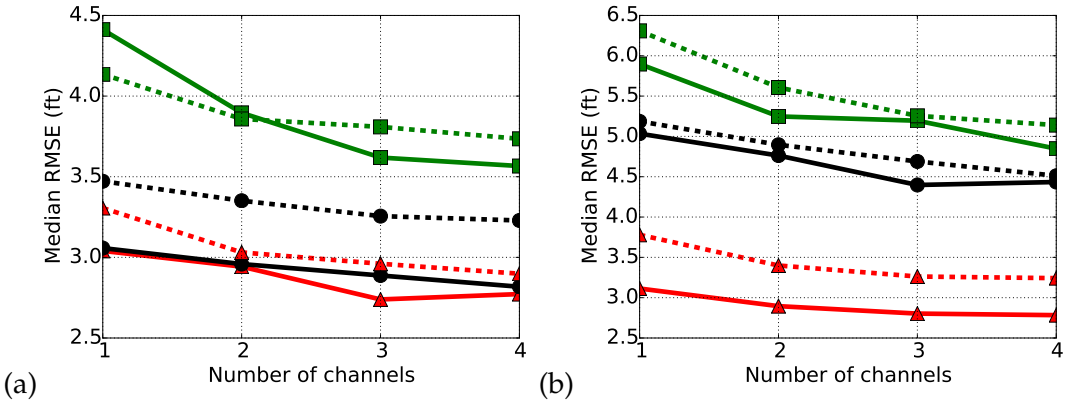

Figure 6.10. Median RMSE achieved as a function of the number of channels measured for (a) brick house and (b) cement board house. Solid lines use MARTI while dashed lines use VRTI. The ▲ shows E-shaped patch antenna data points, ● shows omnidirectional antenna data points, and ■ shows microstrip patch antenna data points.

Table 6.1. Percent Decrease in Median RMSE Achieved by Using E-shaped Patch Antenna Instead of the Antenna Listed

	House	
RTI method and antenna type	Brick	Cement
MARTI with microstrip patch antenna	22	43
VRTI with microstrip patch antenna	23	37
MARTI with omnidirectional antenna	1	37
VRTI with omnidirectional antenna	10	28

6.11 References

[1] J. Wilson and N. Patwari, "See-through walls: Motion tracking using variance-based radio tomography networks," *IEEE Trans. on Mobile Computing*, vol. 10, no. 5, pp. 612–621, May 2011.

[2] M. McCracken, M. Bocca, and N. Patwari, "Joint ultra-wideband and signal strength-based through-building tracking for tactical operations," in *2013 IEEE Int. Conf. on Sensing, Commun. and Networking (SECON)*, June 2013, pp. 309–317.

[3] J. T. Gonzalez-Partida, P. Almorox-Gonzalez, M. Burgos-Garcia, B. P. Dorta-Naranjo, and J. I. Alonso, "Through-the-wall surveillance with millimeter-wave LFMCW radars," *IEEE Trans. on Geoscience and Remote Sensing*, vol. 47, no. 6, pp. 1796–1805, June 2009.

[4] J. Li, Z. Zeng, J. Sun, and F. Liu, "Through-wall detection of human being's movement by UWB radar," *IEEE Geoscience and Remote Sensing Lett.*, vol. 9, no. 6, pp. 1079–1083, Nov 2012.

[5] D. Maas, J. Wilson, and N. Patwari, "Toward a rapidly deployable radio tomographic imaging system for tactical operations," in *IEEE SenseApp 2013*, Oct 2013, pp. 203–210.

[6] B. Wei, A. Varshney, N. Patwari, W. Hu, T. Voigt, and C. T. Chou, "dRTI: Directional radio tomographic imaging," in *Proc. of the 14th Int. Conf. on Inform. Process. in Sensor Networks*, ser. IPSN '15, 2015, pp. 166–177.

[7] Xandem Technology, "Xandem interview with swat commander - tactical through-wall tracking prototype," 2017. [Online]. Available: https://www.youtube.com/watch?v=QnQKfz-AEi4

[8] F. Yang, X.-X. Zhang, X. Ye, and Y. Rahmat-Samii, "Wide-band E-shaped patch antennas for wireless communications," *IEEE Trans. on Antennas and Propagation*, vol. 49, no. 7, pp. 1094–1100, Jul 2001.

[9] C. Qi, M. B. Akbar, and G. D. Durgin, "Analysis of E-patch antenna performance over various dielectric materials at 2.4 GHz," in *2016 IEEE Int. Symp. on Antennas and Propagation (APSURSI)*, June 2016, pp. 1807–1808.

[10] L. M. Ni, Y. Liu, Y. C. Lau, and A. P. Patil, "Landmarc: Indoor location sensing using active RFID," in *Proc. of the 1st IEEE Int. Conf. on Pervasive Computing and Commun., 2003. (PerCom 2003).*, March 2003, pp. 407–415.

[11] M. Youssef, M. Mah, and A. Agrawala, "Challenges: Device-free passive localization for wireless environments," in *Proc. of the 13th Annu. ACM Int. Conf. on Mobile Computing and Networking*, ser. MobiCom '07, 2007, pp. 222–229.

[12] F. Viani, P. Rocca, M. Benedetti, G. Oliveri, and A. Massa, "Electromagnetic passive localization and tracking of moving targets in a WSN-infrastructured environment," *Inverse Problems*, vol. 26, no. 7, p. 074003, 2010.

[13] K. Woyach, D. Puccinelli, and M. Haenggi, "Sensorless sensing in wireless networks: Implementation and measurements," in *2006 4th Int. Symp. on Modeling and Optimization in Mobile, Ad Hoc and Wireless Networks*, April 2006, pp. 1–8.

[14] C. Xu, B. Firner, Y. Zhang, R. Howard, J. Li, and X. Lin, "Improving rf-based device-free passive localization in cluttered indoor environments through probabilistic classification methods," in *2012 ACM/IEEE 11th Int. Conf. on Inform. Process. in Sensor Networks (IPSN)*, April 2012, pp. 209–220.

[15] B. Mager, P. Lundrigan, and N. Patwari, "Fingerprint-based device-free localization performance in changing environments," *IEEE J. on Selected Areas in Commun.*, vol. 33, no. 11, pp. 2429–2438, Nov 2015.

[16] J. Wilson and N. Patwari, "A fade-level skew-Laplace signal strength model for device-free localization with wireless networks," *IEEE Trans. on Mobile Computing*, vol. 11, no. 6, pp. 947–958, June 2012.

[17] X. Chen, A. Edelstein, Y. Li, M. Coates, M. Rabbat, and A. Men, "Sequential Monte Carlo for simultaneous passive device-free tracking and sensor localization using received signal strength measurements," in *Proc. of the 10th ACM/IEEE Int. Conf. on Inform. Process. in Sensor Networks*, April 2011, pp. 342–353.

[18] J. Wilson and N. Patwari, "Radio tomographic imaging with wireless networks," *IEEE Trans. on Mobile Computing*, vol. 9, no. 5, pp. 621–632, May 2010.

[19] O. Kaltiokallio, M. Bocca, and N. Patwari, "Enhancing the accuracy of radio tomographic imaging using channel diversity," in *2012 IEEE 9th Int. Conf. on Mobile Ad-Hoc and Sensor Sys. (MASS 2012)*, Oct 2012, pp. 254–262.

[20] L-Com Global Connectivity, "2.4 GHz 8 dBi LH Circular Polarized Patch Antenna - 4ft SMA Male Connector," http://bit.ly/2oCVhWv, 2017, [Online; accessed 7-March-2017].

[21] J. Wilson, N. Patwari, and O. G. Vasquez, "Regularization methods for radio tomographic imaging," in *2009 Virginia Tech Symp. on Wireless Personal Commun.*, 2009.

[22] P. Hillyard, "Data Set For Through-wall Localization Using an E-shaped Patch Antenna," 2017. [Online]. Available: http://bit.ly/2mzj4Ib

CHAPTER 7

NEVER USE LABELS: SIGNAL STRENGTH-BASED BAYESIAN LOCALIZATION IN CHANGING ENVIRONMENTS

P. Hillyard, and N. Patwari, "Never use labels: Signal strength-based bayesian localization in changing environments," IEEE Trans. on Mobile Computing, (to be submitted).

7.1 Abstract

Wireless sensor networks have opened up many opportunities for detecting breaches in physical property, for making home automation more versatile, and for remotely monitoring the health and activity of home-bound aging patients. In these applications, device-free localization (DFL) methods use measured changes in the received signal strength (RSS) between many pairs of statically deployed RF nodes to provide location estimates of a person inside the wireless network. Many significant challenges face DFL methods. First, without fingerprint training, it is difficult to model RSS measurements as a function of a person's location caused by multipath fading. Second, DFL methods have relied on empty room calibration or fingerprint training to reliably localize a person. However, these methods need to be frequently recalibrated or retrained to stay current with changing environments. Online methods attempt to solve this problem, but are unable to localize stationary people. In this paper, we address these challenges by first, creating a mixture model of observing measured RSS as a function of a person's location. We develop two new Bayesian localization methods which are based on our mixture model. We experimentally validate our new system at three different test sites with over seven days worth of measurements. From these experiments, we demonstrate that, when compared to other DFL methods, MLL and HMML reduce localization error by $11-44\%$, localizes a stationary person, and achieves localization performance that does not degrade in changing environments.

7.2 Introduction

Wireless sensor networks have opened up many opportunities for detecting breaches in physical property, for making home automation a reality, and for remotely monitoring the health and activity of home-bound aging patients. These systems depend on knowing the location of people in an area of interest. Previous research has shown how a person, without an RF tag, can be localized through-walls by processing received signal strength (RSS) measurements between many pairs of statically deployed RF nodes. This tag-less based localization technology is also called sensorless sensing [29], passive localization [25], and device-free localization (DFL) [31].

DFL in indoor environments presents many significant challenges. One challenge is that, because of multipath fading, it is difficult to model the effect a person's location will have on the measured RSS of a link. With a fine resolution of fingerprint locations, fingerprint training can start to capture the unpredictable relationship between RSS measurements and a person's location by measuring the relative frequency of RSS measurements at each location [24]. While fingerprinting can be very accurate in localizing people, the fingerprints must be laboriously retrained to stay current in changing environments [16]. Alternative DFL methods like radio tomographic imaging (RTI) [26], Bayesian methods [13], and particle filters [8], [28], [33] provide more flexibility for DFL because the relationship between measured RSS and a person's location is modeled *a priori*.

A fundamental element of model-based DFL is based on the idea that a link is *affected*, i.e., has significant measured changes in RSS, when a person is on the link line. The link line is the imaginary line segment connecting the link's nodes. In contrast, when the link is *unaffected*, i.e., has very little measured change in RSS, the person tends to be is off of the link line. Model-based DFL methods have been built around the idea that the link is affected only when a person is inside an ellipse whose foci are the nodes of the link [14], [26]. In reality though, the link can be affected even when a person is far from the link line, or unaffected when a person is on the link line.

In this paper, we develop a new mixture model where a link can be both affected and unaffected but weighted based on the location of the person. In our mixture model, we learn RSS distribution parameters for both the affected and unaffected state of each link and we do so without labelled measurements. The weights in our mixture model are

derived from a spatial model such that the affected RSS distribution is weighted more when a person is on the link line and weighted less the further the person is from the link line. We incorporate our new mixture model in two new Bayesian localization methods we develop which we call maximum likelihood localization (MLL) and hidden Markov model localization (HMML). MLL and HMML both compute the probability of observing the measured RSS given a person's location. Adding a temporal property to localization, HMML extends MLL by estimating the current location based on the previous location. In that both MLL and HMML operate on the same mixture and spatial models, and only differ in their temporal properties, we refer to them generally as model-based probabilistic localization (MPL). However, we differentiate between the localization method used in MPL as either MLL or HMML.

A second significant challenge with DFL in general, and our model specifically, is that the affected and unaffected RSS distributions are nonstationary in changing environments. Consequently, DFL methods that require an empty room calibration or fingerprint training will need frequent recalibration or retraining to adjust to a changing environment [14], [26]. In contrast, online calibration methods quickly adjust to a changing environments but can only locate motion [27], [32].

An additional contribution of this paper is that we develop a localization system that addresses the drawbacks of traditional empty room and online calibration methods and fingerprint training. Our system localizes a stationary person, adapts to changes in RSS due to a changing environment, does not require a vacant area for calibration, and does not require fingerprint training. We call this calibration method *continuous recalibration*. Continuous recalibration is accomplished by using a current location estimate to update the distribution parameters of links that are unaffected by the person's presence.

We experimentally validate HMML and MLL at three separate sites and with over 7 days of measured RSS data. We demonstrate that MPL does not need an empty room calibration or fingerprint training period, that it adapts to changes in RSS due to a changing background, and that it is capable of localizing a stationary person. We compare HMML and MLL to an RTI method which uses empty room calibration [26], to an RTI method that uses online calibration [32], and to a Bayesian linear discriminant analysis method [30] which localizes with a trained fingerprint measurements database. We show that HMML

and MLL can match or decrease the localization error by $11-44\%$ compared to these other DFL methods.

7.3 Related Works

The ability to locate a person indoors using sensors has changed the way we think about security, home automation and smart homes, and aging in place. Some of these sensing systems include: cameras that detect changes in pixel values caused by a person's presence [4]; pyroelectric sensors that detect and locate changes in thermal radiation due to a person's presence [11]; and vibration sensors to localize vibrations from a person walking [18]. These sensing systems are not a optimal sensing modality in applications for security or first response where the sensors must be deployed on the outside of a home or building. Cameras and infrared sensors cannot sense through material opaque to visible light, and vibration sensors must be sensitive enough to detect vibrations on the inside of the home while ignore ambient vibrations. Our MPL solution, like other RF solutions, is a more appropriate choice for through-wall sensing since RF can sense through walls, smoke, and in any lighting condition.

RF sensing systems perform localization in a variety of ways. Ultra-wideband radios can be used in multistatic radar to measure the time-of-flight between pulse transmissions and received reflections caused by moving people [17]. The time-of-flight is proportional to the distance between the reflector and the transmitter and receiver which is used to localize a person. Ultra-wideband radios have also been used measure changes in the line-of-sight power and then perform tomography with those measurements [6]. A person's presence has also been shown to create significant changes in the amplitude of subcarriers in PHY layer measurements of commodity WiFi cards. These changes have been used in a fingerprint classification method to localize a person [1]. However, with more communication devices downloading content and evermore RF devices being used for sensing applications like gesture recognition [20], breathing rate estimation [19], heart rate estimation [2], and keystroke detection [3], there is even a greater need to be handwidth-friendly in an already crowded ISM band. Multi-static radar and sensing with WiFi cards occupy a very large bandwidth just for sensing. Our MPL solution uses measured RSS on narrowband transceivers which occupy only a small portion of the ISM band in order to

perform DFL.

Our MPL method is complementary to methods that process RSS to perform DFL including particle filters [8], [28], fingerprint classification [16], [30], and RTI [14], [26]. These methods, however, either need a person to stand at several locations, to have the area completely vacant for a short period [7], [14], [23], [26], or to have the person continuously moving in order to perform localization [9], [32]. What sets our work apart is that MPL can perform DFL without fingerprinting, without a vacant area, and can localize stationary people.

DFL methods vary in how RSS measurements are used to estimate location. In fingerprint-based localization, a person stands at many locations in the area of interest while the RSS distribution or statistics of the RSS distributions are recorded [16], [30]. During testing, the likelihoods or Bayesian probability of measuring the observed RSS is computed for each fingerprint from which the estimated location is derived. With enough fingerprint locations, fingerprint-based localization captures the hard to predict RSS distribution of a link as a function of a person's location. However, this comes at an unsustainable cost of frequently retraining fingerprints to stay current with changing environments. MPL seeks to provide a highly accurate localization system, like that of fingerprinting, but by doing so with a model that provides more flexibility in changing environments.

In RTI methods, a spatial model is first constructed to indicate which locations in the area of interest will cause a change in RSS if a person occupies that location [14], [26]. A least-squares solution then estimates an image of the most likely locations a person was based on the change in RSS observed on the links in the network. MPL provides an alternative approach to localization by computing the probability of observing RSS measurements based on a person's location. Our work compares the localization accuracy of these two methods of localization.

Another variation of DFL is particle filtering. As in MPL, particle filters develop RSS distributions for when a person is on a link line and when they are off of the link line [8], [28], [33]. Particles are then drawn from a Gaussian distributions and are said to be drawn from the affected RSS distribution when their excess path length to a link are less than some threshold. Otherwise they are drawn from the unaffected RSS distribution [28]. MPL differs from this approach in that we do not place 0 or 1 weights to the affected and

unaffected RSS distribution, but soft weights that are a function of the person's excess path length to a link. This approach inserts some uncertainty in the model to account for the reality that a link may not be affected even when a person is standing on the link line or that a link is affected when the person is far from the link line. MPL also differs from particle filters because it uses fixed locations inside the area of interest instead of particles. When the possible locations are fixed, we are able to store the weights in memory instead of having to compute them every time particles are re-sampled.

7.4 Methods

In this section, we describe the fundamental components of MPL generally and of MLL and HMML specifically. These components of MPL are shown in the block diagram in Figure 7.1 and include: a one-time parameter estimation of our mixture model that relates RSS to a occupied location; a lightweight, online RTI method that runs in tandem with either MLL or HMML to provide a location of a moving person; a continuous recalibration block that continuously reestimates the parameters of the links' affected and unaffected distributions; and a block where MLL or HMML is executed. MLL computes the maximum likelihood of the state given the RSS measurements and HMML computes Bayesian probabilities of a person's location for a current RSS measurement given the previous state. We describe each of these components in more detail in the following sections.

7.4.1 Equipment and Measurements

An important place to start is to first describe our equipment and the wireless channel measurements we make. In this paper, our nodes are Texas Instruments CC2531 dongles that communicate according to the ZigBee IEEE 802.15.4-based specification in the 2.4 GHz ISM band. We deploy N nodes around the area of interest. The nodes are programmed to take turns transmitting a packet on a 802.15.4 channel during dedicated time slots using TDMA and a token-ring passing protocol. This protocol is repeated on a predefined set of 802.15.4 channels.

After each node has taken a turn transmitting on each channel, a separate node logs the RSS, also called the received power in decibel units, between each pairwise node on a computer. We denote the RSS measured on link $l = (i, j, c)$ formed by transmitting

node i and receiving node j on channel c as r_l. The RSS is typically a discrete-valued measurement, and we denote its possible values as $\mathcal{S}_r$. We note that $\mathcal{S}_r$ also includes $\oslash$, the event that there was a missed packet and as such RSS was not measured. We observe a vector $\mathbf{r} = [r_1, r_2, \ldots, r_L]$ on L links.

7.4.2 RSS Distribution Models

As in many model-based DFL methods, MPL adopts the idea that a link is either in an *affected* or an *unaffected* state [13], [28]. When the link is unaffected, the person is said to be off of the link line and the RSS follows one distribution. When the link is affected, the person is said to be on the link line and the RSS follows a second distribution. This claim is supported by measurements we collect in an experiment. In this experiment, a person walks around a room at known times and at known coordinates while we record RSS measurements. We show in Figure 7.2 a link's distribution of RSS when a person is far from the link line and when the person is on or near the link line. The affected and unaffected RSS distributions can be modeled as skew-Laplace [28], or Ricean [10], but we sacrifice model accuracy for a Gaussian model where we need to only estimate two model parameters per link state. A normal distribution has also been adopted in [30], [33]. The mean and variance of the unaffected distribution we denote as $\hat{\mu}_{l,u}$ and $\hat{\sigma}^2_{l,u}$ where the subscript u specifies unaffected. The mean and variance of the affected distribution we denote as $\hat{\mu}_{l,a}$ and $\hat{\sigma}^2_{l,a}$ where the subscript a specifies affected.

For link l, we estimate the mean and variance of both distributions using RSS measurements when there is evidence that the link is unaffected. We describe in Section 7.4.6 how we decide when RSS is measured when the link is unaffected, but for now, we create a buffer of length B for link l. When a link is unaffected, we add r_l to the buffer. When a measurement is added to the buffer, we compute both the sample mean and the sample variance of the buffer which we save as $\tilde{\mu}_{l,u}$ and $\tilde{\sigma}^2_{l,u}$, respectively. When there are no changes to objects in the background environment, we anticipate $\tilde{\mu}_{l,u}$ to be about the same as $\hat{\mu}_{l,u}$. So, we only perform the update $\hat{\mu}_{l,u} \leftarrow \tilde{\mu}_{l,u}$ and $\hat{\sigma}^2_{l,u} \leftarrow \tilde{\sigma}^2_{l,u}$ when $|\hat{\mu}_{l,u} - \tilde{\mu}_{l,u}| > 1$.

From Figure 7.2, we also observe that the mean of the unaffected histograms is a few dB greater than the affected histogram's mean. Also, the variance of the affected histogram is larger than the unaffected variance. In our model, we use these observations to also

estimate the mean and variance of the affected distribution by $\hat{\mu}_{l,a} \leftarrow \hat{\mu}_{l,u} - \Delta$ and $\hat{\sigma}^2_{l,a} \leftarrow \eta\hat{\sigma}^2_{l,u}$. We have found that $\Delta = 3$ dB and $\eta = 2.5$ are appropriate parameters to use for indoor settings. We also note that to estimate $\tilde{\sigma}^2_{l,u}$, we use the maximum of the sample variance of the buffer and a minimum constant $\omega^2 > 0$. Due to quantization of RSS, the sample variance may be zero even though the true real-valued received power would have had a positive variance. We impose a minimum variance of $\omega^2 > 0$ to avoid numerical instability. We have found that $\omega = 0.75$ is an appropriate value for this application.

When the mean and variance of a link's unaffected and affected distributions have been re-estimated, we recompute their RSS mass functions as

$$f(r_l \mid u) = \begin{cases} \epsilon, & r_l = \oslash \\ \max\left\{\epsilon, \frac{1}{\gamma}\mathcal{N}(r_l; \hat{\mu}_{l,u}, \hat{\sigma}^2_{l,u})\right\}, & r_l \neq \oslash \end{cases} \tag{7.1}$$

and

$$f(r_l \mid a) = \begin{cases} \epsilon, & r_l = \oslash \\ \max\left\{\epsilon, \frac{1}{\gamma}\mathcal{N}(r_l; \hat{\mu}_{l,a}, \hat{\sigma}^2_{l,a})\right\}, & r_l \neq \oslash \end{cases} \tag{7.2}$$

where γ is constant such that the pmf sums to one, and $\epsilon > 0$ is a small-valued lower bound on the probability value away from zero. The use of the minimum probability ϵ is due to the fact that in practice, we may observe values far from the mean more often than described by equations (7.1) and (7.2) because temporal fading does not always fit the log-normal distribution [12]. Using a small value ϵ conveys the model uncertainty and avoids numerical issues with very low probabilities in likelihood computations we describe in Section 7.4.5.

7.4.3 RSS-Location Mixture Model

So far, we have only said that a link is affected when a person is on or near the link line and unaffected when a person is far from the link line. In this section, we develop a mixture model that defines the relationship between the link's affected or unaffected state and the location of a person in the network.

The approach with many DFL methods is to say a link is affected when a person is standing inside an ellipse whose foci are the coordinates of the link's nodes [26]. Instead of setting a strict elliptical boundary on when the link is affected and unaffected, other models have used a decaying elliptical model where changes in RSS on a link are weighted according to the person's excess path length to the link [15].

In MPL, we adopt a similar decaying elliptical model that we base off of an experiment that we perform. In this experiment, a person moves inside many 1.22 m^2 areas for 30 s each, during which time RSS for many links are measured and recorded. An additional 30 s of RSS is recorded when the person is not in the area of interest. In postprocessing, we find the mean RSS for each link and for each location the person occupied, including when the person stood outside the area of interest. In Figure 7.3, we show the absolute difference in mean RSS when a person occupies each 1.22 m^2 area and the mean RSS when the area of interest in vacant for link l. We threshold the image so that the absolute differences that are greater than 2 dB are shown in blue, and smaller differences are shown in red. What Figure 7.3 shows is which areas experience a decrease in mean RSS when a person occupies the area. In Figure 7.3, we observe that, in general, areas near the link line tend to result in a decrease in RSS. Areas that are further away tend to experience small differences in RSS. However, we also observe that some locations show no measured change in RSS even when the person is on the link line. Additionally, when a person is very far from the link line, the link's RSS can significantly change in mean. A simple elliptical model does not capture the uncertainties due to multipath fading.

Using the results of this experiment, we create our spatial model. First, we create a grid of $P+1$ evenly distributed coordinates situated inside the area of interest and one coordinate representing the out-of-the-area coordinate. The kth coordinate we denote $\mathbf{x}_k^{grid}$ where $k \in \{0, \ldots, P\}$. These coordinates represent the finite set of possible locations a person could stand while inside or outside the area of interest. The coordinate designated for when a person is outside of the area of interest is $\mathbf{x}_P^{grid} = [\infty, \infty]$. In our model, the probability that link l is affected when a person stands at grid coordinate $\mathbf{x}_k^{grid}$ is

$$p_l(a \mid \mathbf{x}_k^{grid}) = \beta_l \cdot e^{-\delta_{l,k}/\lambda_l} \tag{7.3}$$

where the excess path length of $\mathbf{x}_k^{grid}$ with respect to link l is $\delta_{l,k} = d(\mathbf{x}_k^{grid}, \mathbf{x}_l^{tx}) + d(\mathbf{x}_k^{grid}, \mathbf{x}_l^{rx}) - d(\mathbf{x}_l^{tx}, \mathbf{x}_l^{rx})$, $d(\mathbf{x}, \mathbf{y})$ is the Euclidean norm between $\mathbf{x}$ and $\mathbf{y}$, $\mathbf{x}_l^{tx}$ is the coordinate of link l's transmitter, $\mathbf{x}_l^{rx}$ is the coordinate of link l's receiver, and β_l and λ_l are parameters we will estimate. Since our model says that the link is either affected or unaffected, the probability that link l is unaffected when a person stands at grid coordinate $\mathbf{x}_k^{grid}$ is $p_l(u \mid \mathbf{x}_k^{grid}) = 1 - p_l(a \mid \mathbf{x}_k^{grid})$. For the out-of-the-area coordinate $\mathbf{x}_P^{grid}$, we manually set

$p_l(a \mid \mathbf{x}_P^{grid}) = 1\text{e}{-3}$.

The conditional probabilities from our spatial model are then used to model the relationship between RSS measured on link l and the location of a person in our mixture model

$$f(r_l \mid \mathbf{x}_k^{grid}) = p_l(a \mid \mathbf{x}_k^{grid}) \cdot f(r_l \mid a) + p_l(u \mid \mathbf{x}_k^{grid}) \cdot f(r_l \mid u). \tag{7.4}$$

In our model, there is some probability of the link being affected and unaffected, but the state of the link is weighted according to the excess path length of the person relative to the link. When the person is near the link line, the affected distribution is weighted more heavily than the unaffected distribution. The choice of β_l and λ_l gives us some control over how the weights in the model are selected so that we can adjust to the different fading characteristics of each link.

7.4.4 Estimating Spatial Model Parameters

In this section we describe how we estimate the mixture model parameters β_l and λ_l for each link l. To accomplish this, our goal is to estimate β_l and λ_l such that our mixture model closely matches the distribution of RSS measurements as a function of the excess path length of the person's location and link l. This estimation process refers to the KRTI and parameter estimation block seen in Figure 7.1. KRTI is an online DFL method that does not require an empty room calibration period [32]. We choose KRTI because of its relatively low computational complexity and its highly accurate localization capability. KRTI updates a long and short term RSS histogram with every new RSS measurement. The difference between these two histograms is computed using the kernel distance. The differences from all of the links are then used to form an image and estimate the location of a person. During a training period a person walks inside the area of interest. During this time, KRTI provides an estimated location, $\hat{\mathbf{x}}^{krti}$, for each r_l. We store all $< r_l, \delta_l^{krti} >$ tuples where δ_l^{krti} is the excess path length between $\hat{\mathbf{x}}^{krti}$ and link l.

After the training period is complete, we first estimate the mean and variance of the unaffected distribution with, respectively, the median and median absolute deviation (MAD) of the RSS during the training period. We use these statistics to estimate the mean and variance of the unaffected RSS distribution. The median and MAD ignore RSS measurements that fall far from the true unaffected mean and robustly estimate the mean and variance.

Additionally, we multiply the MAD by 1.48 and square the value so that it is a unbiased estimate of the variance for Gaussian data [22]. Once the unaffected mean and variance have been estimated, we apply the same shift to the mean and scale to the variance to get the affected mean and variance as described in Section 7.4.2.

After the training period is complete and the affected and unaffected RSS distribution parameters are estimated, we turn to the RSS, excess path length tuples previously mentioned. An example of the tuples for one of the links is shown in Figure 7.4. We next divide r_l into bins according to excess path length δ_l^{krti}. We choose to bin all tuples $< r_l, \delta_l^{krti} >$ into groups such that their excess path lengths are equal. The possible ordered bin values are in the set $\{\delta_l^{krti}(0), \ldots, \delta_l^{krti}(M-1)\}$ where M is the total number of bins. The RSS measurements for one group of these tuples are seen in the grey box in Figure 7.4 and the histogram of these RSS measurements is shown in Figure 7.5. We denote the histogram of the RSS measurements whose excess path length is $\delta_l^{krti}(m)$ as $\mathbf{h}_{l,m}$ where index m indexes in the set of all excess path lengths. We wish to find an optimal $b_{l,m}$ such that the mixture model $f(r_l \mid b_{l,m}) = b_{l,m} \cdot f(r_l \mid a) + (1 - b_{l,m}) \cdot f(r_l \mid u)$ most closely matches $\mathbf{h}_m$. To do this, we perform

$$b_{l,m}^* = \underset{b_{l,m} \in \mathcal{S}_b}{\arg\min}\, d(f(r_l \mid b_{l,m}), \mathbf{h}_{l,m}) \tag{7.5}$$

where $\mathcal{S}_b$ is a set of equally-spaced real valued numbers between 1e$-$5 and 1. An example optimal mixture model is shown in in Figure 7.5.

We get the tuples $< \delta_l^{krti}(m), b_{l,m}^* >$ by performing this process for all excess path length bins. We plot these tuples for a link in Figure 7.6. The relationship between $b_{l,m}^*$ and $\delta_l^{krti}(m)$ follows our spatial exponential decay function (7.3). We estimate β_l and λ_l from a nonlinear least squares solution. The estimation includes constraining $0 < \beta_l < 1$ to keep the conditional probabilities between 0 and 1 and $\lambda_l > 0$ so that a link is always more likely to be affected by a person on or near the link line over a person far from the link line. When the training period is over and β_l and λ_l are estimated, we never re-estimate β_l and λ_l and consequently no longer need to run KRTI.

7.4.5 Localizing with MLL and HMML

In this section, we frame the problem of DFL in terms of possible states a person could occupy. We describe how MLL and HMML use the mixture model from Section 7.4.3 to

compute the likelihood and joint probabilities of a person being in these states. In the following subsections, we describe the HMML method and in the process, describe the MLL method.

7.4.5.1 States and Emission Probabilities

A Markov chain models a system of P discrete states where the chain is said to be in only one state at each time step. At each time step, the chain can remain in the same state or transition into another with some probability. When applied to DFL, the states of our Markov chain are the discrete locations a person could be standing. We have previously defined these locations as the grid coordinates $\mathbf{x}_k^{grid}$ for $k = \{0, \ldots, P\}$. We first map each grid coordinate $\mathbf{x}_k^{grid}$ to a state q_k in the Markov chain. However, the state of our Markov chain is not observable since we do not know where the person is standing. However, we are able to measure a random variable that is a output of the Markov chain's current state. This random variable is the RSS vector $\mathbf{r}$ from the links in our wireless network. By using a hidden Markov model [21], we can use $\mathbf{r}$ to estimate the state of the Markov chain.

In Section 7.4.3, we developed a mixture model (7.4) to come up with a probability of measuring an RSS for link l given that a person is standing at $\mathbf{x}_k^{grid}$. We change the notation in (7.4) to $f(r_l \mid q_k) = p_l(a \mid q_k) \cdot f(r_l \mid a) + p_l(u \mid q_k) \cdot f(r_l \mid u)$ so that we now refer to the states of the Markov chain using the one-to-one mapping with the grid coordinates. Assuming that the RSS measurements on all links are independent, we compute the probability of measuring $\mathbf{r}$ given the current state by

$$p_k(\mathbf{r}) = \prod_{l=1}^{L} f(r_l \mid q_k). \tag{7.6}$$

However, the product of L probabilities can result in numerical issues when L is large. So when L is large, we use $p_k(\mathbf{r}) = e^{\sum_{l=1}^{L} \log f(r_l|q_k) - \psi}$ where $\psi = \max \sum_{l=1}^{L} \log f(r_l \mid q_k)$ for $k \in \{0, \ldots, P\}$.

If we just consider the states of the Markov chain, we define how MLL performs localization. The probabilities $p_k(\mathbf{r})$ for $k = \{0, \ldots, P\}$ are the likelihood probabilities of measuring $\mathbf{r}$ when a person is in state q_k. The MLL location estimate, $\hat{\mathbf{x}}^{mll}$, is then the mapping between the grid cooridnates and the state which maximizes these probabilities, $\hat{\mathbf{x}}^{mll} = \arg\max_{0 \le k \le P} p_k(\mathbf{r})$. HMML extends MLL's localization algorithm by considering the transitions between steps at each time step which we discuss next.

7.4.5.2 Initial and Transition Probabilities

A hidden Markov model includes a transition matrix which defines the probabilities of transitioning from one state to another in one time step. In our model, we incorporate the physical constraints of walking inside a typical home, like walking speed and fixed barriers, into our transition probabilities. To do this, we first label each state as either an entrance-exit or as a nonentrance-exit state. Entrance-exits are locations in the area of interest where a person can enter or exit the area of interest. Second, for each state, the states that are 0.75 m away are labelled as neighbors. For entrance-exit states, we include the state q_P, or the out-of-area state, as a neighbor since the only way to leave the area of interest is via an entrance-ext. For the out-of-area state, we label the entrance-exit states as neighbors. However, a state cannot be a neighbor if a person must travel through a wall to get to that state. Third, we assume that a person is more likely to stay in the current state than to transition to another.

In terms of transition probabilities, we assign the probability of remaining in the same state after one time step to be 0.9 for all states. Then for all non-neighbor states, we assign a probability $1e{-}200$. For all neighbor states, we assign a equal probability so that the sum of probabilities of transitioning from the current state to any other state equals 1. We note that wall and entrance-exit information is extra information required to create these transition probabilities. Consequently, we will show in Section 7.6.4 how the localization performance of HMML is affected if we ignore wall and entrance-exit information.

A hidden Markov model also includes the probability π_k that the Markov chain starts in state q_k. We assume that when the system turns on, the person is located out of the area of interest with probability 0.95. All other initial state probabilities are assigned $0.05/P$.

7.4.5.3 Forward Algorithm

The final element of the hidden Markov model is to estimate the current state of the Markov chain with computational efficiency, which the forward solution accomplishes [5]. It solves for the most likely current state of the Markov chain given a history of $\mathbf{r}$ observations by inductively computing a vector $\alpha_k[t]$ at each time t for each state $k = \{0, \ldots, P\}$, and then estimating the current location of the person as $\hat{\mathbf{x}}^{hmml} = \arg\max_{0 \leq k \leq P} \alpha_k[t+1]$. The forward algorithm initializes $\alpha_k[1] = \pi_k p_k(\mathbf{r}[1])$ where $\mathbf{r}[1]$ is the first measured RSS

vector, and then computes $\alpha_k[t+1] = \left[\sum_{w=0}^{P} \alpha_w[t] P_{wk}\right] p_k(\mathbf{r}[t+1])$ for each $t > 0$ and for $0 \leq k \leq P$.

7.4.6 Continuous Recalibration

An important element of MPL is that it does not use an empty room calibration period, nor a fingerprint training period, to estimate the mean and variance of the affected and unaffected RSS distributions. Furthermore, MPL is capable of adapting to the nonstationary RSS distributions. We enable these features of MPL by running a light weight companion localization method called VRTI [27]. Using online calibration, VRTI localizes motion by computing the sample variance of a buffer of RSS for each link. The sample variance for each link is used to form an image of the motion, from which we estimate a person's location. We denote the location estimate from VRTI as $\hat{\mathbf{x}}^{vrti}$.

The purpose of running VRTI in tandem with MPL is that VRTI is able to quickly adapt to changes in the background and still localize the person. With VRTI's location estimate, we not only know where the moving person is located but also where they are not located. If a person is not near a link, we can safely update that link's RSS unaffected distribution parameters. We say that $\hat{\mathbf{x}}^{vrti}$ is far from a link if the excess path length of $\hat{\mathbf{x}}^{vrti}$ with respect to link l, which we denote $\delta_l^{vrti} = d(\mathbf{x}^{vrti}, \mathbf{x}_l^{tx}) + d(\mathbf{x}^{vrti}, \mathbf{x}_l^{rx}) - d(\mathbf{x}_l^{tx}, \mathbf{x}_l^{rx})$, is greater than $\delta_l^{max}/2$ where δ_l^{max} is the maximum excess path length of any coordinate in x_k^{grid} for $k \in \{0, \ldots, P-1\}$ with respect to link l. When $\delta_l^{vrti} > \delta_l^{max}/2$, we add r_l to the B-length buffer referred to in Section 7.4.2.

In as much as VRTI is unable to distinguish between a stationary person and when the area of interest is vacant, the RSS distribution parameters won't be re-estimated when the person is stationary or when a person is outside of the area of interest. However, it is important to update the RSS distributions when the area of interest is vacant. To re-estimate the RSS distribution parameters when the area of interest is vacant, we add r_l to the B-length buffer, if it has not been added already, when HMML or MLL says the area of interest is empty, i.e. when $k = P$ is the solution to $\arg\max_{0 \leq k \leq P} \alpha_k$ or $\arg\max_{0 \leq k \leq P} p_k(\mathbf{r})$. The mean and variance of the buffer is then used to periodically re-estimate the distribution parameters for both a link's unaffected and affected state as described in Section 7.4.2. With both the location estimate of VRTI and HMML or MLL, we are able to perform

continuous recalibration without an empty room calibration period. We found that $B = 15$ was an appropriate buffer length for our application.

As an example of how we perform continuous recalibration, we show in Figure 7.7 the measured RSS on a link during a time when the unaffected RSS increases by 6 dB when the background environment changes at 2550 s. We also show $\hat{\mu}_u$ for the link during this time period as it is re-estimated. After a few minutes, our unaffected mean RSS estimate adjusts to the increase in RSS due to the changing environment.

7.4.7 Baseline DFL Methods

Many DFL methods exist that perform an empty room calibration period or run an online calibration. Empty room calibration is inconvenient for those people who must wait outside of the area of interest. Additionally, DFL methods that implement empty room calibration quickly become unreliable estimation methods they are frequently recalibrated. DFL methods with online calibration lose track of stationary people. Other DFL methods require fingerprint training where a person stands at many locations in the area of interest while RSS measurements are stored in a database. Like DFL methods with empty room calibration, fingerprint DFL becomes unreliable as the real fingerprints diverge from those in the database. In this paper, we compare HMML and MLL, both of which address all of these drawbacks, against well-known DFL methods.

One of these methods is attenuation-based RTI which we refer to as RTI [26]. RTI requires an empty room calibration where the mean RSS for each link is computed and stored. The absolute difference between $\mathbf{r}$ and the mean RSS is computed and stored as $\mathbf{y}^{rti}$, which is, in turn, used to compute an image and estimate the person's location. The second method is kernel-based RTI which we refer to as KRTI [32]. KRTI continuously updates a long and short-term RSS histogram. The kernel distance between these histograms are then computed and stored as $\mathbf{y}^{krti}$, from which the image and the person's location is estimated. For both RTI and KRTI, we use an elliptical model for the weight matrix $\mathbf{W}$ [26]. A regularized-least squares solution is then used to estimate the image $\mathbf{z}$ using the linear relationship $\mathbf{y} = \mathbf{W}\mathbf{z} + \tilde{\mathbf{n}}$ where $\tilde{\mathbf{n}}$ is the noise. The pixels in the image, $\mathbf{z}$, for both RTI and KRTI map to the same grid coordinates $\mathbf{x}_k^{grid}$ for $k = \{0, \ldots, P-1\}$ mentioned in Section 7.4.3. We use the pixel with the greatest value as the location estimate, which we denote

$\hat{\mathbf{x}}^{rti}$ for RTI and $\hat{\mathbf{x}}^{krti}$ for KRTI. However, when the image maximum falls below a threshold, we set the location estimate as the out-of-the-area pixel $\mathbf{x}_P^{grid}$. We note that MPL also uses KRTI to estimate spatial parameters, but the baseline KRTI mentioned in this section is separate from KRTI used in MPL. After this point, we distinguish between the two when needed.

The last method is a linear discriminant analysis classifier, which we refer to as LDA, that requires RSS fingerprints at many locations [30]. During fingerprinting, a person moves inside of a small area around a known location. The mean RSS of all L links is recorded for fingerprint location index k' and stored as $\boldsymbol{\mu}_{k'}^{lda}$ where $k' = \{0, \ldots, K'\}$, $K'+1$ is the total number of fingerprints, and $\mathbf{x}_{k'}^{fp}$ are the coordinates of the fingerprint. We denote the out of the area fingerprint as $\mathbf{x}_{K'}^{fp}$. The covariance of the RSS over all fingerprint locations, $\hat{\boldsymbol{\Sigma}}$, is then estimated using Ledoit-Wolf shrinkage as $\hat{\boldsymbol{\Sigma}} = (1-\nu)\boldsymbol{\Sigma}' + \nu\rho I$ where $\boldsymbol{\Sigma}' = \sum_{k'=1}^{K'} \sum_{t \in class k'}^{K'} (\mathbf{r}[t] - \boldsymbol{\mu}_{k'}^{lda})(\mathbf{r}[t] - \boldsymbol{\mu}_{k'}^{lda})^T / (T - K')$ and T is the number of RSS measurement vectors measured during fingerprinting. Ledoit-Wolf shrinkage is a traditional way to estimate a covariance matrix when the number of samples used for estimation is small but the number of variables to estimate is high. We find ourselves in this situation since the number of measurements we record at each fingerprint tends to be small. Finally, we find the k' that maximizes $\mathbf{r}^T \hat{\boldsymbol{\Sigma}}^{-1} \boldsymbol{\mu}_{k'}^{lda} - 0.5 \boldsymbol{\mu}_{k'}^{lda\,T} \hat{\boldsymbol{\Sigma}}^{-1} \boldsymbol{\mu}_{k'}^{lda}$ which gives us our location estimate $\hat{\mathbf{x}}^{lda}$.

7.5 Experimentation

In this section, we describe the three test sites we used to evaluate the localization performance. We also describe the localization metric used for the evaluation.

7.5.1 Test Sites

In our evaluation, we perform experiments at three different test sites. At each site, we first collect a training data set which we use to perform supervised fingerprint training for LDA and to perform unsupervised estimation of β_l and λ_l for each link in MPL. Additional testing data sets are then performed. Both training and testing data sets include the known location of the person moving through the area. Experimentation at each test site was performed differently, so we describe each test site individually. For each site, the grid

coordinates $\mathbf{x}_k^{grid}$ used for KRTI, RTI, and MPL are generated automatically such that the grid points are evenly distributed around the area of interest. Fingerprint locations for LDA are created only for locations in the area of interest where a person walks during testing.

7.5.1.1 Class Room

Our first test site, which we refer to as site CR, is an empty classroom. We deploy twenty nodes, which measure on four channels, on the inside perimeter of the classroom such that a majority of the links are line of sight. The floor plan of site CR is shown in Figure 7.8.

A total of 30 s of RSS are collected for fingerprints at 100 locations spaced 0.61 m apart. At each fingerprint location, the person moved inside a 0.61 m^2 before moving to the next fingerprint location. The total duration of the training experiment was 55 min.

During the testing experiments, the room was vacant for the first minute. A person then entered the room and continuously moved to each fingerprint location at least once. A total of twelve test experiments were performed varying between three and twelve min in length. No objects inside the room were intentionally moved at any time during the training and testing data sets.

7.5.1.2 First Floor

Our second test site, which we refer to as site 3F, is the furnished first floor of a home. We deploy thirty nodes, which measure on eight channels, on the inside perimeter of the house. A pair of nodes are attached to a tall stand such that the nodes are 0.3 and 1.3 m above the floor. With the many walls and obstructions in the house, very few of the links are line of sight. The floor plan of site 3F is shown in Figure 7.8.

RSS Fingerprints are collected at 32 locations in the house. The total duration of the training experiment was 33 min. During the testing experiments, the house was vacant for the first 50 s. A person then entered the house and moved to the first fingerprint location, standing there for 50 s. After the 50 s elapsed, the person moved to the next fingerprint location where the process continued. The same procedure was followed for the test experiments except that the person stands at each location for 20 s. The duration

of each of the 15 test experiments was 10 min.

After the training experiment and each testing experiment, an intentional change to the house was made. For example, a couch was moved, a washer lid was shut, or a sink was filled with water. These intentional changes were performed to simulate the passage of time in a typical house where objects are moved, added, or removed from the area of interest. We note that this training and testing data set was originally created and used in [16].

7.5.1.3 Basement Living

Our last test site, which we refer to as site BL, is a furnished living room, bedroom, and hall in a basement. We deploy fifteen nodes, which measure on four channels, on the inside perimeter of the area of interest where very few of the links are line of sight. The floor plan of site CR is shown in Figure 7.8.

During the training experiment, a person continuously moved around the basement at known locations at known times. For fingerprinting, we create several reference locations that serve as the fingerprint location since the person was moving for the duration of the training period. The duration of the training experiment was 15 min.

During the testing experiments, the basement was vacant for the first minute. A person then entered and continuously walked around the basement. However, the person also reclined on a bed, and sat in an armchair, on a couch, and in a chair for 2 min each at different points during the experiment. This was done to show how DFL methods with online calibration lose track of a stationary person. The duration of each testing experiment is fourteen min; however, we continue to record RSS measurements for 24 h. We wanted to capture the changes in the environment that happen as a result of day-to-day living. This way, changes in the environment are also recorded in the RSS. A total of seven 24-h test experiments are performed.

7.5.2 Localization Accuracy

The DFL methods we evaluate produce a location estimate for each time t. These methods can also indicate that the area of interest is vacant. When a person is in the area of interest and the DFL method detects the person is in the network, we call this a true presence detection (TPD). When no person is present in the area of interest but we

detect presence, we call this a false alarm (FA). And when a person is present in the area of interest but we fail to detect presence, we call this a missed detection (MD). With these definitions, we compute the localization error at time t as

$$e[t] = \begin{cases} e_p, & \text{FA or MD} \\ d(\hat{\mathbf{x}}[t], \mathbf{x}^{true}[t]), & \text{TPD} \end{cases} \tag{7.7}$$

where e_p is a fixed error of 1.22 m to penalize missed detections and false alarms, $\mathbf{x}^{true}$ is the true location coordinate, and $\hat{\mathbf{x}}[t]$ is the estimated location coordinate from one of the localization methods. We then compute the median of $e[t]$ for all t and call it the median penalized Euclidean error e^{med}.

7.6 Results

In this section, we discuss the localization performance of MLL and HMML and our baseline DFL methods, RTI, KRTI, and LDA. We show how MLL and HMML outperform all of the baseline methods at three different sites, how MLL and HMML robustly localize moving and stationary people, and how MLL and HMML adapt to changing environments. We then make intentional modifications to MLL and HMML and show how their localization performance is affected.

7.6.1 DFL Method Comparison

In this paper, we perform many experiments at three different sites to show how MLL and HMML can accurately localize people in many settings. We show the penalized median error, e^{med}, for MLL, HMML, and the baseline DFL methods at the three sites in Figure 7.9. We quickly observe that for all sites, MLL and HMML outperform or match the baseline methods in localization accuracy. At sites 3F and BL, where there were considerable changes to the environment, we see that MLL and HMML reduce e^{med} by 44% or greater when compared to RTI and LDA. Since the environment changes often at site 3F, RTI and LDA's empty room and fingerprint calibration methods become outdated, resulting in poor performance over time. When the environment does not change, like in the CR experiments, RTI and LDA's localization performance closely matches MLL, HMML and KRTI. However, an unchanging environment, like at site CR, is not likely to exist in most applications.

In contrast, we observe that MLL reduces the penalized median error by up to 11% and HMML by up to 9% compared to KRTI at the three sites. While this reduction in error seems small, it is important to recognize that it becomes more challenging to make significant reductions in error when the errors are already considerably low given the size of the site areas, the number of nodes deployed, and the spatial diversity of the nodes. Additionally, MLL and HMML have the advantage of localizing stationary people, a feature that is missing in KRTI and other online DFL methods.

7.6.2 Tracking Stationary People Evaluation

One of the important features of both MLL and HMML is that they keep track of a stationary person. On the other hand, DFL methods that use online calibration only image motion, and so when a person is stationary, these DFL methods eventually lose track of the person. An example of the difference between HMML and KRTI, which performs online calibration, is shown in Figure 7.10. We note that MLL is not shown because its performance is about the same as HMML and we therefore did not want to clutter the figure by including MLL's results. We show a window of time during the BL experiments where a person sat still for 2 min at two locations. From the figure we observe that HMML yields a lower localization error during the two 2-min intervals than KRTI; and we also observe that, while HMML keeps track of the stationary person, KRTI eventually loses track of the person while they are stationary. For KRTI, losing track of the person results in missed detections. A missed detection for applications like monitoring the activity of aging patients can be potentially life threatening. For example, if a person fell to the floor and could not move, we need a system to tell us that the person is still in that location and not out of the house so that we can take necessary responsive action.

7.6.3 Continuous Recalibration Evaluation

Another important feature of MLL and HMML is that it can robustly localize a person even in changing environments. DFL methods that perform an empty room or fingerprint training before the system will gradually suffer in localization performance. As the environment changes, the empty room calibration measurements gradually diverge from those measurements recorded during training. We show an example of localization performance in changing environments in Figure 7.11. The penalized median error is shown for RTI

and HMML for each of the 15 test experiments at site 3F. Again, MLL's performance is similar to HMML, and we therefore did not want to clutter the figure by including MLL's results. HMML and RTI perform equally as well for the first experiment since RTI's empty room calibration measurements are current. With each successive experiment, intentional changes are made to the environment. As a result, RTI's localization error increases, even doubling by experiment five. Without frequent empty room calibration, RTI is unable to provide a reliable location estimate. On the other hand, HMML robustly localizes the person in spite of a changing environment. With the addition of LDA, these same observations can be seen in Figure 7.12 which shows the median penalized error for each of the seven test experiments at site BL.

7.6.4 MPL Feature Evaluation

In this section, we intentionally modify parts of MLL and HMML to see how localization is affected. We make the following four modifications to HMML and MLL.

- First, we use fixed values for λ and β for all links in lieu of estimating them in the spatial model parameter estimation block in Figure 7.1. We call this modification FIXED. We perform this modification for both HMML and MLL.

- Second, we use the true location $\mathbf{x}^{true}$ instead of $\mathbf{x}^{krti}$ to estimate λ and β in the spatial model parameter estimation block in Figure 7.1. We call this modification TRUE and make the modification for both MLL and HMML.

- Third, we ignore wall and entrance-exit information when creating the transition probabilities. We call this modification NO WALL but only apply this to HMML since MLL does not use transition probabilities.

The unmodified MLL and HMML we call BASELINE. Only one modification is made to MLL and HMML at a time. With the modification, we perform localization using the data sets from our three sites and show the results for MLL in Figure 7.13 and for HMML in Figure 7.14.

With the FIXED modification, we entirely eliminate the KRTI and parameter estimation blocks, as seen in Figure 7.1, from MPL. In their place, λ and β are tuned by the user and, consequently, MLL and HMML is ready to run when the system starts. There is no need

for any calibration. From Figure 7.14, we observe that setting all spatial parameters to be the same value for all links increases the penalized median error for HMML by 7 cm at site 3F, reduces the error by 2 cm at site CR, and makes no significant change at site BL when compared to BASELINE. From Figure 7.13, we observe that setting all spatial parameters to be the same value for all links increases the penalized median error for MLE by 4 cm at site 3F, 2 cm at site BL, and 27 cm at site CR when compared to BASELINE.

For a majority of the sites, both MLL and HMML show little loss in localization performance with FIXED when compared to BASELINE. This result demonstrates that, without significant performance loss, MPL does not necessarily need a calibration period where a person walks inside the area of interest. The user could alternatively tune λ and β and the system would be ready to perform localization. The CR site does show that MLL might be more sensitive to this tuning, but overall, MPL becomes a much more attractive DFL method with the FIXED modification.

With the TRUE modification, we require the user to provide labelled RSS data with their true location during the training phase. We wish to see if having labelled training data would improve the estimation of the spatial parameters, and, in turn, improve localization. These true locations replace the estimated locations from KRTI. From Figure 7.14 and Figure 7.13, we observe that at all three sites, supplying labelled RSS data matches or decreases localization error for MLL and HMML when compared to BASELINE. The improvement to localization performance can be as great as 6 cm. The user may decide that the performance gains are too small to warrant having to provide labelled RSS data. However, the trade-off is the additional computational overhead needed to run KRTI for the location estimates.

Finally, with the NO WALL modification, we eliminate the need for extra wall information to be entered into HMML prior to operation. From Figure 7.14, we observe that at all three sites, ignoring wall and entrance-exit information never results in improved localization performance when compared to BASELINE. The greatest increase in error was 3 cm at the BL site. These results suggest that excluding wall and entrance-exit information from informing the creation of transition probabilities does increase the localization error. However, the user may opt to forego entering in the information into HMML and incur only a small localization performance loss.

7.6.5 Complexity and Feature Trade-Offs

We have shown how MML and HMML achieve a lower localization error than other DFL methods and can do so in a changing environment and without an empty room or fingerprint calibration period. Other DFL methods do not share all of these same properties. The trade-off, however, for using MLL and HMML over other DFL methods is the greater memory and computational complexity required to run them. In Table 7.1 and Table 7.2, we compare the features offered by MLL, HMML and other DFL methods, their calibration requirements, and their memory and computational complexity.

The table shows how each of the DFL methods we compare in this paper use different initial calibration methods. RTI requires a period of time when the area of interest is vacant while LDA requires fingerprint training. Empty room calibration and fingerprint training may be feasible, but for aging in place applications, these calibration methods would cause too much inconvenience by having to frequently recalibrate or retrain them. MPL, on the other hand, is calibrated by a person moving around the area of interest, which is likely something that the person would be doing anyway during the course of a day. The big difference between MPL and RTI and LDA is that MPL is able to achieve constant localization performance in changing environments whereas RTI and LDA cannot do so unless empty room calibration or labelled fingerprint training measurements are frequently performed.

In contrast, KRTI does not require any calibration and achieves constant performance in changing environments. The trade-off is that KRTI and other online calibration DFL methods are unable to localize stationary people. Applications like home automation and assisted living are dependent on knowing where a person is, even when they are stationary. MPL is able to localize stationary people, but the trade-off is that MPL must be calibrated by having a person walk around in the area of interest. However, we showed that by modifying MPL to use tuned values for λ and β instead of estimating them, we would also classify MPL as requiring no calibration like KRTI.

A significant trade-off to consider when using MLL or HMML are their relatively higher memory and computational complexity compared to other DFL methods. We observe that, compared to other DFL methods, HMML has an extra P^2 memory factor which is used to store the transition probabilities and an extra P^2 term in computational complexity which

is needed to compute the forward algorithm. The greater memory and computational cost of HMML were used to add a temporal component to localization. We set out to see if the temporal properties of HMML would provide greater localization accuracy than its MLL little brother, but we did not observe those gains. HMML is therefore at a disadvantage when P is increased when compared to any of the DFL methods we compared.

The alternative to HMML is MLL, which we see does not include the extra P^2 memory and P^2 computation like for HMML. We also saw in the previous sections that MLL often performed localization just as well as HMML. Since MLL ignores the temporal component that HMML embraces, it reduces the computational and memory cost by a nontrivial amount. One question to be asked though is, why doesn't HMML benefit from the addition of transition probabilities? We note that both MLL and HMML use the likelihood probabilities in (7.6) which turn out to be values either very near 0 or very near 1 since L is large for all of our experiments. Therefore, the transition probabilities play an insignificant role when inductively computing the joint probabilities α_k. The localization results of MLL and HMML demonstrate that, in this application, there is no clear advantage for including temporal properties into the localization problem by using HMML.

If we were to consider using another DFL method other than MLL, KRTI would be a smart choice. KRTI has no need of calibration and it is highly accurate. However, MLL, which only adds another LP of memory and LP of computation by comparison, buys the advantage to track stationary people while achieving similar localization performance. This advantage is an important feature to have when monitoring an aging, home-bound family member or patient and for enabling smart home features that depend on sensing presence.

7.7 Conclusion

In this paper, we have presented a new signal strength-based Bayesian device-free localization system called model-based localization (MPL) that can localize stationary people, does not require an empty room calibration period, and achieves constant localization performance in changing environments. In MPL, we develop a new mixture model where the probability of a person occupying a location is a function of signal strength measurements from a wireless sensor network. A fundamental piece of our model is that a wireless

link is either affected or unaffected by the presence of a person. Links are typically affected when a person stands on or near the link line, and are unaffected when a person stands far form the link line. Our mixture model allows for uncertainty in the state of the link as a function of the person's location. We develop two realizations of MPL including MLL and HMML which compute the probabilities of a person's location based on the RSS measurements observed. MLL computes the likelihoods of observing RSS measurements given a person's location while HMML computes the joint probabilities of observing RSS measurements given a person's location using the forward algorithm of a hidden Markov model. In addition, we develop a new method to perform continuous recalibration so that our model can adjust to a changing environment.

To validate the performance of MLL and HMML, we perform a series of experiments at three different sites and compute the localization error of MLL, HMML and three other DFL methods. We demonstrate that MLL and HMML outperform the baseline methods in terms of localization accuracy, that MLL and HMML are capable of localizing a stationary person when other baseline methods cannot, and that MLL and HMML achieves constant localization performance even when the environment changes. In addition, we demonstrated that the MLL can perform localization as well HMML but with a fraction of the memory and computational cost. For assisted living and home automation applications, MPL offers an important advantage of constant localization performance and tracking stationary people without significant costs in computational complexity, memory usage, or convenience.

7.8 Acknowledgment

This material is based upon work supported by the National Science Foundation under Grant Nos. #1407949 and #1035565.

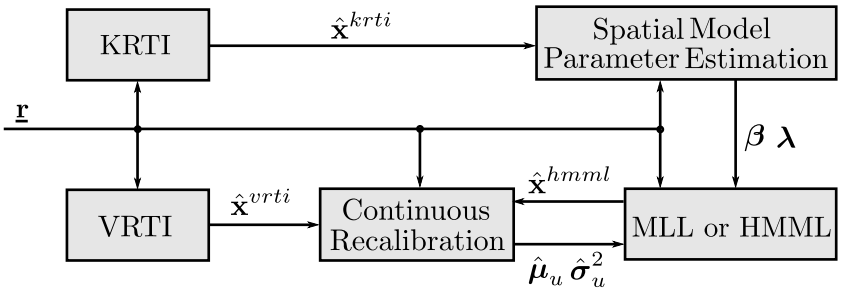

Figure 7.1. Block diagram of model-based probabilistic localization (MPL).

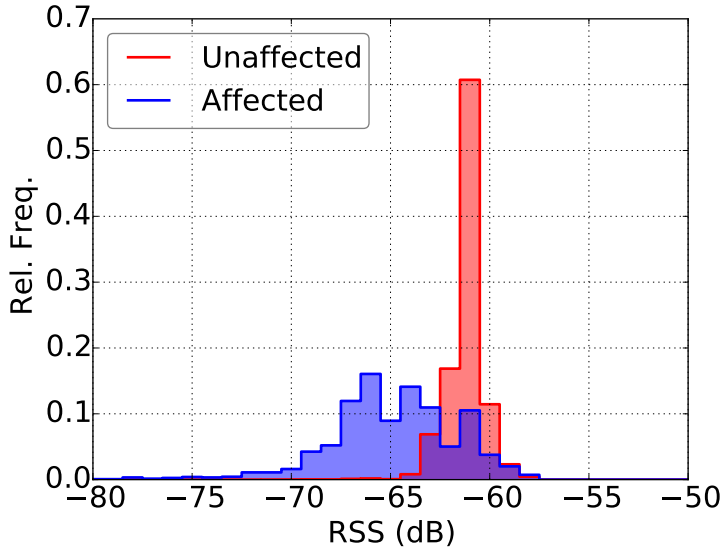

Figure 7.2. Distribution of RSS when a person is on or near the link line and the link is affected, and when a person is far from the link line and the link is unaffected.

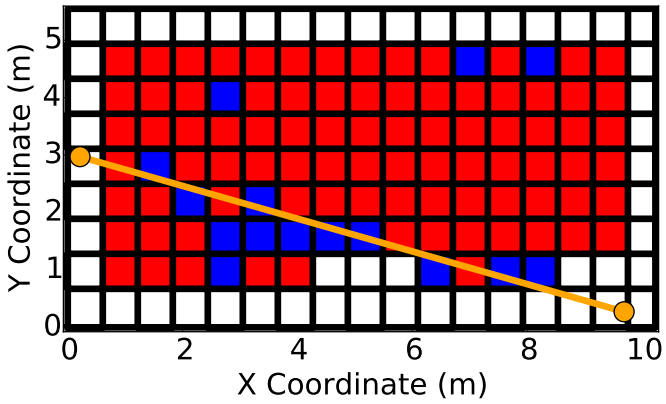

Figure 7.3. The absolute difference between the mean RSS during empty room and the mean RSS when a person occupied each square. Red squares represent an absolute difference of 2 dB or less. Blue squares represent an absolute difference greater than 2 dB. The white squares were never occupied. The nodes and link line are shown in orange.

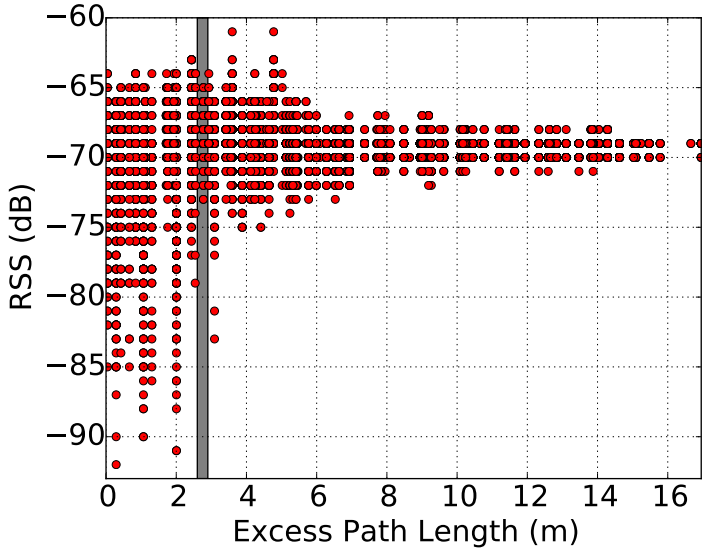

Figure 7.4. Measured RSS as a function of excess path length for a link. Excess path length is computed using the estimated location from the KRTI block seen in Figure 7.1. One group of RSS measurements with the same excess path length is shown in the gray box.

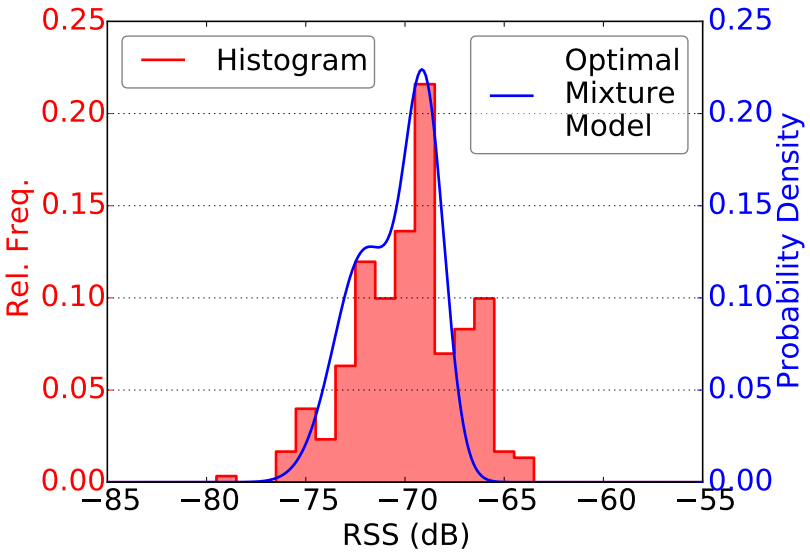

Figure 7.5. Histogram of RSS within the gray box of Figure 7.4. The optimal mixture model for this histogram is overlaid.

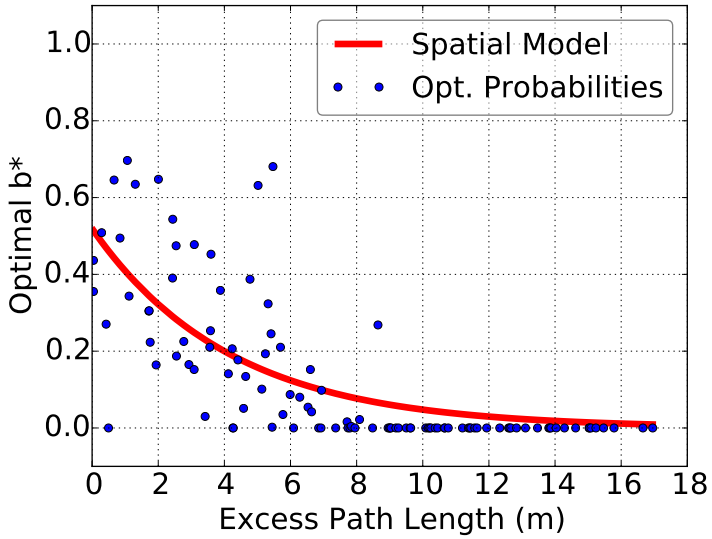

Figure 7.6. Optimal probabilities b^* as a function of excess path length. The estimated spatial model is overlaid.

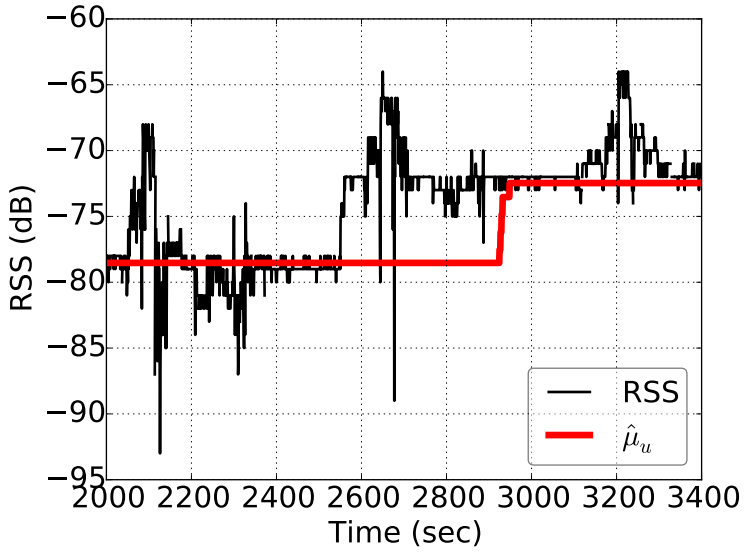

Figure 7.7. Measured RSS during an experiment where changes in the environment cause the unaffected RSS mean to change by 6 dB. The red line shows how our continuous recalibration eventually adjusts the estimate of the unaffected mean after environment changes.

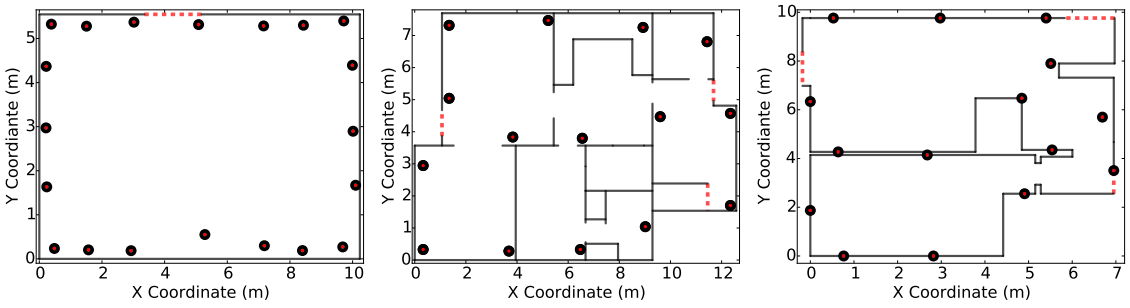

Figure 7.8. Experiment locations where the walls or barriers are shown in black and the nodes are shown as red circles. The red dashed lines indicate where entrance-exits are located for (left) class room, CR (middle) first floor, 3F (right) basement BL.

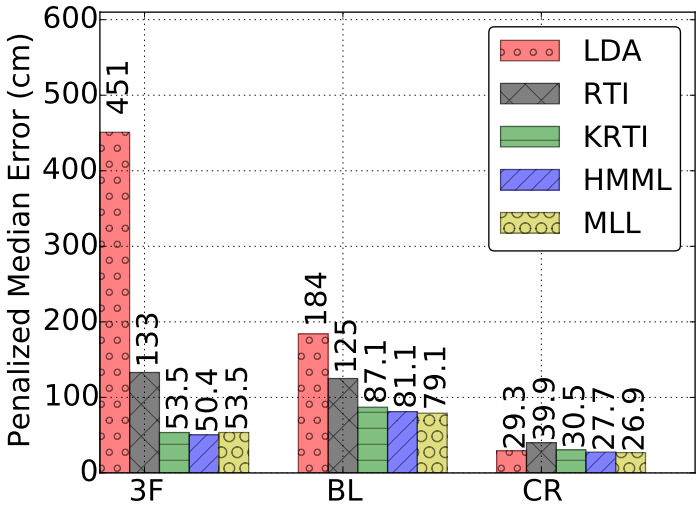

Figure 7.9. Penalized median Euclidean error, e^{med}, for LDA, RTI, KRTI, MLL and HMML at three different experiment sites. Only site CR maintained a relatively unchanged environment during the course of the training and testing experiments and was the only site that were most links were line of sight.

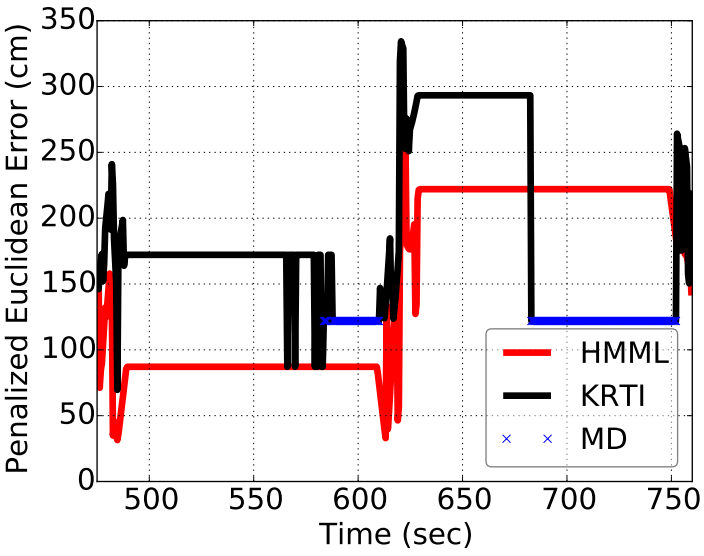

Figure 7.10. The penalized Euclidean error is shown over time for HMML and KRTI during part of the BL experiments. In this window of time, a person sat still twice for 2 min each. HMML keeps track of the stationary person whereas KRTI eventaully loses track of the person. Periods of missed detections (MD), where KRTI loses track of the person, are shown in blue.

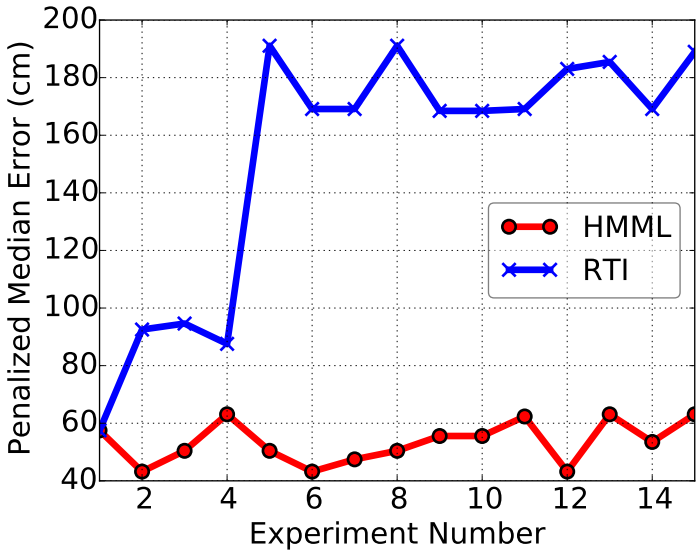

Figure 7.11. Penalized median error for each of the sixteen test experiments performed at 3F for RTI and HMML. Intentional changes to the environment were made after each experiment. HMML adjusts to these changes with continuous recalibration. RTI, which performs offline calibration, gradually suffers in localization performance as the empty room calibration measurements diverge from measurements made when the system turned on.

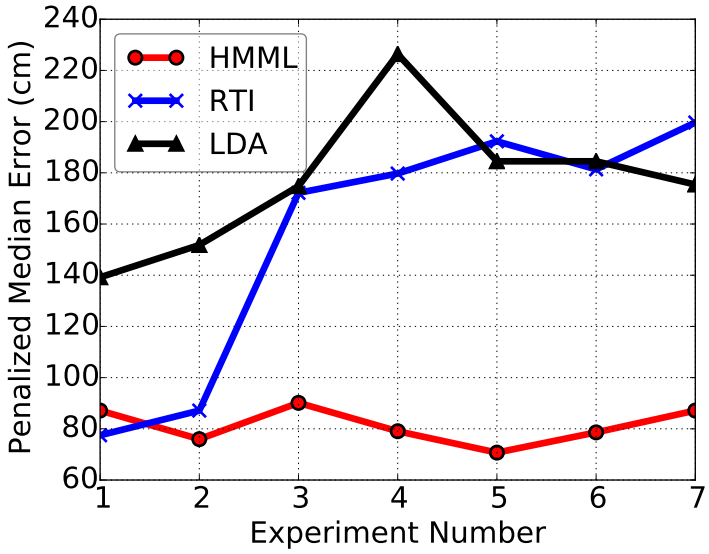

Figure 7.12. Penalized median error for each of the seven test experiments performed at BL for LDA, RTI, and HMML. Changes to the environment after each test were the result of day-to-day living. HMML adjusts to these changes with continuous recalibration. RTI, which performs empty room calibration, and LDA, which performs a fingerprint calibration, gradually suffers in localization performance as the empty room and fingerprint calibration measurements become out dated.

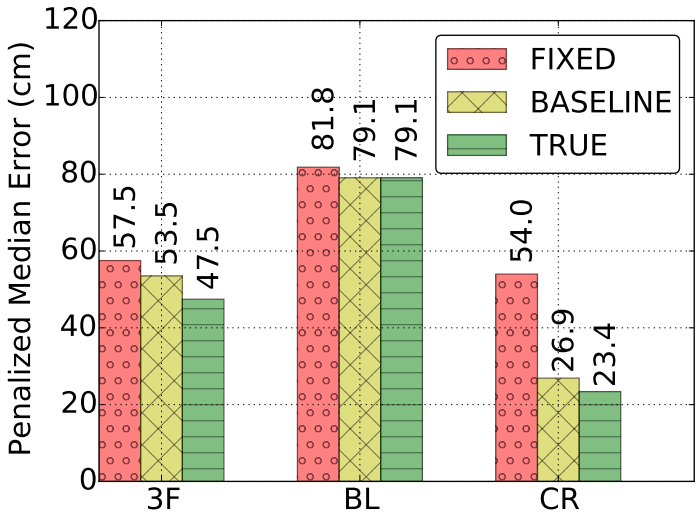

Figure 7.13. Penalized median error for a modified MLL at three different experiment sites. In FIXED, we use the same λ and β parameters for all links. In TRUE, the true location $\mathbf{x}^{true}$ is used instead of $\mathbf{x}^{krti}$ to estimate λ and β. BASELINE indicidates no modification.

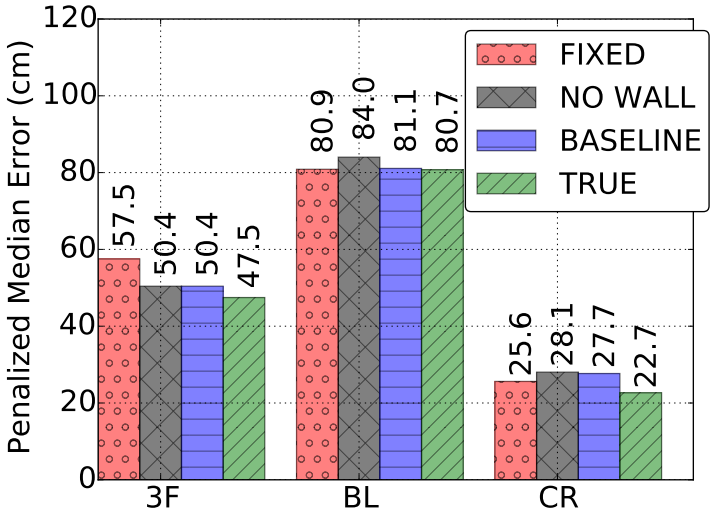

Figure 7.14. Penalized median error for a modified HMML at three different experiment sites. In FIXED, we use the same λ and β parameters for all links. In NO WALL, we ignore wall and entrance-exit information when creating the transition probabilities. BASELINE is HMML without modifications. In TRUE, the true location $\mathbf{x}^{true}$ is used instead of $\mathbf{x}^{krti}$ to estimate λ and β.

Table 7.1. Localization Features Offered by DFL Methods Along With Their Calibration Requirements.

	Initial Calibration				Localize	
DFL Method	Labelled Empty	Labelled Fingerprint	Unlabelled Occupied	None	Motion	Stationary Person
LDA		X			X	X
KRTI				X	X	
RTI	X				X	X
HMML			X		X	X
MLL			X		X	X

Table 7.2. Features Offered by DFL Methods Along With Their Memory and Computational Complexity. For Reference, L is the Number of RSS Measurements, P is the Number of Grid Coordinates, and R is the Number of Bins Used for Histograms. The Costs for Continuously Running VRTI for HMML and MLL are Included in Their Complexity.

		Complexity	
DFL Method	Constant perf. in changing env.'s	Memory	Computation
LDA		$LP + P$	$LP + P$
KRTI	X	$LP + 2LR$	$LR + LP$
RTI		LP	$L + LP$
HMML	X	$2LP + 2LR + P + P^2$	$L + 2LP + P^2$
MLL	X	$2LP + 2LR$	$L + 2LP$

7.9 References

[1] H. Abdel-Nasser, R. Samir, I. Sabek, and M. Youssef, "Monophy: Mono-stream-based device-free WLAN localization via physical layer information," in *2013 IEEE Wireless Commun. and Networking Conf. (WCNC)*, April 2013, pp. 4546–4551.

[2] F. Adib, H. Mao, Z. Kabelac, D. Katabi, and R. C. Miller, "Smart homes that monitor breathing and heart rate," in *Proc. of the 33rd Annu. ACM Conf. on Human Factors in Computing Sys.*, ser. CHI '15, 2015, pp. 837–846.

[3] K. Ali, A. X. Liu, W. Wang, and M. Shahzad, "Keystroke recognition using wifi signals," in *Proc. of the 21st Annu Int. Conf. on Mobile Computing and Networking*, ser. MobiCom '15, 2015, pp. 90–102.

[4] D. Anderson, J. M. Keller, M. Skubic, X. Chen, and Z. He, "Recognizing falls from silhouettes," in *2006 Int. Conf. of the IEEE Eng. in Medicine and Biology Soc.*, Aug 2006, pp. 6388–6391.

[5] L. E. Baum, J. A. Eagon *et al.*, "An inequality with applications to statistical estimation for probabilistic functions of Markov processes and to a model for ecology," *Bull. Amer. Math. Soc*, vol. 73, no. 3, pp. 360–363, 1967.

[6] B. Beck, X. Ma, and R. Baxley, "Ultrawideband tomographic imaging in uncalibrated networks," *IEEE Trans. on Wireless Commun.*, vol. 15, no. 9, pp. 6474–6486, Sept 2016.

[7] M. Bocca, O. Kaltiokallio, and N. Patwari, *Radio Tomographic Imaging for Ambient Assisted Living*. Berlin, Heidelberg: Springer Berlin Heidelberg, 2013, pp. 108–130.

[8] X. Chen, A. Edelstein, Y. Li, M. Coates, M. Rabbat, and A. Men, "Sequential Monte Carlo for simultaneous passive device-free tracking and sensor localization using received signal strength measurements," in *Proc. of the 10th ACM/IEEE Int. Conf. on Inform. Process. in Sensor Networks*, April 2011, pp. 342–353.

[9] A. Edelstein and M. Rabbat, "Background subtraction for online calibration of baseline RSS in RF sensing networks," *IEEE Trans. on Mobile Computing*, vol. 12, no. 12, pp. 2386–2398, Dec 2013.

[10] M. Ghaddar, L. Talbi, T. A. Denidni, and A. Sebak, "A conducting cylinder for modeling human body presence in indoor propagation channel," *IEEE Trans. on Antennas and Propagation*, vol. 55, no. 11, pp. 3099–3103, Nov 2007.

[11] Q. Hao, D. J. Brady, B. D. Guenther, J. B. Burchett, M. Shankar, and S. Feller, "Human tracking with wireless distributed pyroelectric sensors," *IEEE Sensors J.*, vol. 6, no. 6, pp. 1683–1696, Dec 2006.

[12] H. Hashemi, "A study of temporal and spatial variations of the indoor radio propagation channel," in *PIMRC-94*, vol. 1, Sep 1994, pp. 127–134.

[13] P. Hillyard, A. Luong, and N. Patwari, "Highly reliable signal strength-based boundary crossing localization in outdoor time-varying environments," in *2016 15th ACM/IEEE Int. Conf. on Inform. Process. in Sensor Networks (IPSN)*, April 2016, pp. 1–12.

[14] O. Kaltiokallio, M. Bocca, and N. Patwari, "Enhancing the accuracy of radio tomographic imaging using channel diversity," in *2012 IEEE 9th Int. Conf. on Mobile Ad-Hoc and Sensor Sys. (MASS 2012)*, Oct 2012, pp. 254–262.

[15] O. Kaltiokallio, R. Jantti, and N. Patwari, "An adaptive radio tomographic imaging system," *IEEE Trans. on Vehicular Technology*, vol. PP, no. 99, pp. 1–1, 2017.

[16] B. Mager, P. Lundrigan, and N. Patwari, "Fingerprint-based device-free localization performance in changing environments," *IEEE J. on Selected Areas in Commun.*, vol. 33, no. 11, pp. 2429–2438, Nov 2015.

[17] M. McCracken and N. Patwari, "Hidden Markov estimation of bistatic range from cluttered ultra-wideband impulse responses," *IEEE Trans. on Mobile Computing*, vol. 13, no. 7, pp. 1509–1521, July 2014.

[18] M. Mirshekari, S. Pan, P. Zhang, and H. Y. Noh, "Characterizing wave propagation to improve indoor step-level person localization using floor vibration," in *SPIE Smart Structures and Materials+ Nondestructive Evaluation and Health Monitoring*. Int. Soc. for Optics and Photonics, 2016, pp. 980 305–980 305.

[19] N. Patwari, L. Brewer, Q. Tate, O. Kaltiokallio, and M. Bocca, "Breathfinding: A wireless network that monitors and locates breathing in a home," *IEEE J. of Selected Topics in Signal Process.*, vol. 8, no. 1, pp. 30–42, Feb 2014.

[20] Q. Pu, S. Gupta, S. Gollakota, and S. Patel, "Whole-home gesture recognition using wireless signals," in *Proc. of the 19th Annu. Int. Conf. on Mobile Computing & Networking*, ser. MobiCom '13, 2013, pp. 27–38.

[21] L. Rabiner, "A tutorial on hidden Markov models and selected applications in speech recognition," *Proc. IEEE*, vol. 77, no. 2, pp. 257–286, 1989.

[22] P. J. Rousseeuw and C. Croux, "Alternatives to the median absolute deviation," *J. of the Amer. Statistical Assoc.*, vol. 88, no. 424, pp. 1273–1283, 1993.

[23] A. Saeed, A. E. Kosba, and M. Youssef, "Ichnaea: A low-overhead robust WLAN device-free passive localization system," *IEEE J. of Selected Topics in Signal Process.*, vol. 8, no. 1, pp. 5–15, Feb 2014.

[24] M. Seifeldin, A. Saeed, A. E. Kosba, A. El-Keyi, and M. Youssef, "Nuzzer: A large-scale device-free passive localization system for wireless environments," *IEEE Trans. on Mobile Computing*, vol. 12, no. 7, pp. 1321–1334, July 2013.

[25] F. Viani, P. Rocca, M. Benedetti, G. Oliveri, and A. Massa, "Electromagnetic passive localization and tracking of moving targets in a WSN-infrastructured environment," *Inverse Problems*, vol. 26, no. 7, p. 074003, 2010.

[26] J. Wilson and N. Patwari, "Radio tomographic imaging with wireless networks," *IEEE Trans. on Mobile Computing*, vol. 9, no. 5, pp. 621–632, May 2010.

[27] ——, "See-through walls: Motion tracking using variance-based radio tomography networks," *IEEE Trans. on Mobile Computing*, vol. 10, no. 5, pp. 612–621, May 2011.

[28] ——, "A fade-level skew-Laplace signal strength model for device-free localization with wireless networks," *IEEE Trans. on Mobile Computing*, vol. 11, no. 6, pp. 947–958, June 2012.

[29] K. Woyach, D. Puccinelli, and M. Haenggi, "Sensorless sensing in wireless networks: Implementation and measurements," in *2006 4th Int. Symp. on Modeling and Optimization in Mobile, Ad Hoc and Wireless Networks*, April 2006, pp. 1–8.

[30] C. Xu, B. Firner, Y. Zhang, R. Howard, J. Li, and X. Lin, "Improving rf-based device-free passive localization in cluttered indoor environments through probabilistic classification methods," in *2012 ACM/IEEE 11th Int. Conf. on Inform. Process. in Sensor Networks (IPSN)*, April 2012, pp. 209–220.

[31] M. Youssef, M. Mah, and A. Agrawala, "Challenges: Device-free passive localization for wireless environments," in *Proc. of the 13th Annu. ACM Int. Conf. on Mobile Computing and Networking*, ser. MobiCom '07, 2007, pp. 222–229.

[32] Y. Zhao, N. Patwari, J. M. Phillips, and S. Venkatasubramanian, "Radio tomographic imaging and tracking of stationary and moving people via kernel distance," in *2013 ACM/IEEE Int. Conf. on Inform. Process. in Sensor Networks (IPSN)*, April 2013, pp. 229–240.

[33] Y. Zheng and A. Men, "Through-wall tracking with radio tomography networks using foreground detection," in *2012 IEEE Wireless Commun. and Networking Conf. (WCNC)*, April 2012, pp. 3278–3283.

CHAPTER 8

CONCLUSION

We conclude this dissertation with a research summary of the body of research presented in this dissertation. We end by offering research that has yet to be explored or improved for RF sensing in general and for the research presented in this dissertation.

8.1 Research Summary

The presence and movement of a person in a wireless RF sensor network have an impact on the channel measurements made on the links of the network. Consequently, the channel measurements of the links, like CIR and RSS, can be processed to localize a person and perform environmental sensing. In this dissertation, we have focused on developing new measurement models and methods to improve and enable device-free localization.

8.1.1 Line Crossing Methods

A considerable part of this dissertation has focused on performing localization with link line crossing measurements. Link line crossings were detected from changes in RSS measurements as well as with changes in the energy contained within the first few nanoseconds of a CIR measurement. In one application, we considered wireless networks where a person may only cross a link line occasionally. Traditional DFL methods are not well-suited for these conditions since their models rely on a person crossing multiple link lines simultaneously. We developed a linear regression and line stabbing method that uses a history of link line crossing measurements to estimate the person's track.

In a second application, we considered a network of transceivers in motion to perform through-wall localization. In traditional DFL where nodes are statically deployed, changes in channel measurements are the result of the presence or movement of a person. When the nodes are in motion, changes in channel measurements are the result of both a person and/or small scale fading. We demonstrated that the changes in the energy contained in

the first few nanoseconds of a CIR measurement could be used to discriminate between small scale fading and the presence of a person on the link line. We further demonstrated that a person could be localized through walls using the channel measurements of transceivers in motion.

In a third application, we considered the problem of localizing boundary crossings. Even with the best of line crossing algorithms and in the best of fading characteristics, false and missed link line crossings measurements occur. However, when nodes are linearly deployed, link lines naturally overlap, and so a crossing error on one link could potentially be corrected by the correct measurements of other overlapping links. Two new boundary crossing algorithms are developed to exploit this deployment geometry to robustly localize boundary crossings.

8.1.2 More Realistic Spatial Models

Another contribution of this dissertation was to develop more realistic spatial models to relate channel measurement changes to a person's location. When a wireless device transmits a signal, the resulting electromagnetic wave propagates in many directions. The models of many DFL methods make the assumption that most of the power in the wave is concentrated along the link line, and so when a person crosses the link line, the channel measurements will be noticeably impacted. In multipath environments, this model does not always match reality. In one application, we develop new antennas that are designed stay tuned when placed a dielectric material and to send most of its power along the link line while attenuating multipath that propagate across wider angles. With experimental data, we demonstrated that the new antenna tracked a person with less error with RTI than antennas traditionally used in DFL.

In a second application, we take a more realistic approach to traditional spatial models used in DFL. Traditional spatial models form an ellipse with a link's nodes as foci and say that changes in channel measurements will only contribute to localization when a person is inside the ellipse. But in fact, a person can be inside the ellipse and have no impact on channel measurements. Contrastingly, a person can be outside the ellipse and have a significant impact on the channel measurements. As a solution, we develop a mixture model where RSS measurements come from a distribution when the link is affected or

unaffected. We weight the probability of measuring RSS from these distributions based on the excess path length of the person's location to the link. When the person is on or near the link line, we weight the affected RSS probability higher than the unaffected probability. We develop methods that compute the likelihood and joint probabilities of a person's location for the observed RSS measurements on many links and show that they can outperform other DFL methods.

8.2 Future Work

In this section, we divide future areas of research into extensions to the research presented in this dissertation and then work that can be investigated for RF sensing generally.

8.2.1 Extensions to Presented Research

In this dissertation, we presented many new methods and models to enable and improve DFL. In this section, we provide ways to extend this work for added improvements.

In Chapter 2, we presented both a line stabbing and linear regression method to estimate the track of a person passing through a network. The linear regression model incorporates the time at which a link is crossed into the estimation. The line stabbing method, however, can correct for link line crossing measurement errors. A more robust method could be achieved by first performing line stabbing to obtained a corrected history of link line crossings. The filtered history could then be passed to the linear regression method to incorporate timing into track estimation. Alternatively, a third dimension could be added to the line stabbing method to incorporate time and link line crossing measurements. These methods were tested in simulation but could benefit from a comparison to other DFL methods like RTI and fingerprinting with experimental data. This experimental data could be obtained through a network of fully connected nodes or from star networks like those typically formed in WiFi networks.

In Chapter 3, UWB radios were used to measure the CIR while the radio devices were in motion. In our experiments, we manually defined the location of the UWB radios for each CIR measurement. However, in a more realistic system, the UWB radios need to self-localize. Using the CIR measurements, the UWB radios could both self-localize and detect link line crossings. The UWB radios could then be attached to autonomous ground

or aerial robots to rapidly make measurements of the wireless channels and perform localization. The localization performance could be analyzed as a function of the robots paths and the number of UWB radio devices deployed.

In Chapters 4 and 5, we presented a boundary crossing localization system using RSS measurements. Some boundaries can extend for much longer than was tested in our work and are important to monitor. Future research could explore the number of nodes needed as a function of boundary length. But to collect measurements on long boundaries, it will be important to develop communication protocols to pass RSS measurements from all links to a central node for processing. Furthermore, new localization algorithms may need to be developed to account for the loss of connectivity between nodes that are too far away from each other. New methods could also be developed to ignore the negative effects of wind. This includes small scale fading that can occur if the structure to which a node is attached moves because of wind. An accelerometer on the node could detect these movements. In terms of power, changes in communication protocols or to sensing methods could be created to reduce the amount of power required for each node. Replacing batteries and unconstrained energy use from renewable sources could reduce the practicality of the system. The assumption that the on and off link line distributions are Gaussian could be changed to assume other distributions like skew-Laplace, Ricean, or Rayleigh to more closely match the measured distributions. And a mixture model could be explored to place some uncertainty in the RSS measurement coming from either the on or off link line distribution.

In Chapter 7, we present a new spatial-based mixture model where we define RSS measurements as a function of a person's location. To obtain the model, we assume that the affected RSS distribution is also shifted down in mean and scaled up in variance compared to the unaffected distribution. Alternative methods could estimate the unaffected and affected distribution parameters independently. Additionally, model correctness was compromised for model complexity by assuming a normal distribution. A skew-Laplace or Ricean distribution could be used instead to achieve better model accuracy. One significant downside to the methods presented in Chapter 7 is the use of VRTI to perform continuous recalibration so that we could track both moving and stationary people. Future work could explore methods that turn off VRTI after a time period and only rely on location estimates

from MLL or HMML to perform recalibration.

8.2.2 Future Work in RF Sensing

The usefulness of RF sensing continues to grow. New applications are being discovered while existing systems are being improved.

When choosing how to perform DFL or other RF sensing, one idea to consider is whether to use measurements from an existing wireless network or to design a network specifically for an application. WiFi networks exist in many public buildings and consequently, many devices are connected to the network. These devices can join or leave the network at random times, but while they are on the network, they provide a sensing link. With WiFi networks, the wireless cards provide channel state information on multiple subcarriers which can be a rich source of sensing information. Other networks could be exploited as newer infrastructure is added to cities. Street lights, transportation stops, and transmission lines could have wireless devices installed to relay status data to a remote processing center. The measurements on the wireless devices could be exploited to monitor foot or vehicle traffic, detect person or animal presence, monitor the weather, or provide alerts of potential copper thieves.

For emergency responders and tactical personnel, knowing not just the location of a person hidden behind the walls of a building, but the location of walls and other obstacles can help form strategies for entering and securing the inside premises. DFL can localize a person with centimeter accuracy. As a person moves inside the building, their estimated location informs you which possible transitions from one area to the next. When the transition from one area to other happens rarely or never, it can indicate the location of a wall or other obstacle. Future work could include mapping out walls and barriers based on the location estimates from DFL.

Fingerprint-based DFL has been used to very accurately localize and track a person. Fingerprint training, however, is a laborious process and must be done frequently to stay current with changing environments. However, it may be possible to predict how the fingerprint will change as the environment changes. The changes in the fingerprints may follow a predictable pattern such that new methods and models could be created to re-train the fingerprints in an unsupervised way. To make fingerprint training less laborious,

fingerprints could be trained by the output of a DFL method and inertial sensor measurements from a tag worn by the person. The inertial measurements could be used in a filter to smooth location estimates from the DFL method to provide highly accurate filtered location estimates. The filtered location estimates could then be used as the label for RSS measurements for fingerprint training.

DFL methods could also supplement tag-based localization methods. The tag could either be localized with angle of arrival, time of arrival, or RSS measurements from a separate sensor network or the tag could be a part of the same network and use the same measurements for localization. The problem could also be seen as tag-based localization supplementing DFL methods. A tag identifies a person whereas, in device-free applications, we can only locate an unidentified person. Security and emergency response applications could benefit from knowing not only where people are, but which person is being localized.

DFL systems that are deployed in power-lacking environments need to be designed to conserve power while providing sufficient localization accuracy. The number of nodes in the network, the communication protocol, and the number of channels measured can have a significant influence on the amount of power used for sensing. When power is not a constraint, DFL can benefit from having the nodes perform some of the computation before the node sends its data. Another avenue of research could explore intelligent ways of sending channel measurements (processed or raw) to a central node for processing. In networks where nodes are far apart, there can be significant latency passing data from a node to a central processing location. To have nodes do all or a significant portion of their own processing could help in sending only important information from a node to the base station.